Christian Grodon

# Phase Behavior and Effective Interactions in Colloidal Suspensions

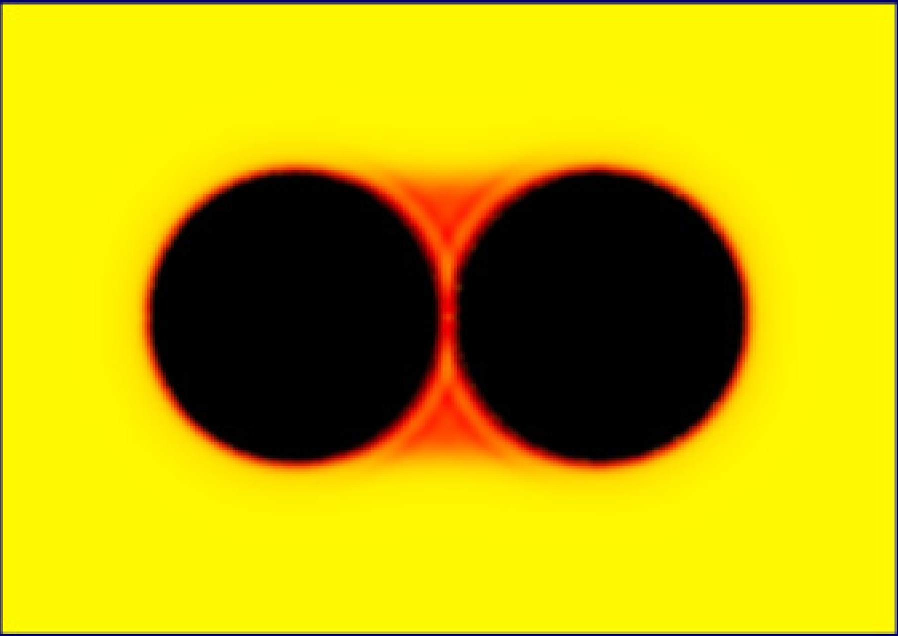

Cuvillier Verlag Göttingen

# Phase Behavior and Effective Interactions in Colloidal Suspensions

Von der Fakultät für Mathematik und Physik der Universität
Stuttgart zur Erlangung der Würde eines Doktors der
Naturwissenschaften (Dr. rer. nat.) genehmigte Abhandlung

Vorgelegt von

Christian Grodon

aus Laurahütte

Hauptberichter: Prof. Dr. S. Dietrich
Mitberichter: Prof. Dr. U. Seifert

Tag der Einreichung: 11. Januar 2007
Tag der mündlichen Prüfung: 12. März 2007

Institut für Theoretische und Angewandte Physik
Universität Stuttgart

Max-Planck-Institut für Metallforschung
Stuttgart

2007

**Bibliografische Information Der Deutschen Bibliothek**
Die Deutsche Bibliothek verzeichnet diese Publikation in der Deutschen Nationalbibliografie; detaillierte bibliografische Daten sind im Internet über http://dnb.ddb.de abrufbar.
1. Aufl. - Göttingen : Cuvillier, 2007
Zugl.: Stuttgart, Univ., Diss., 2007

978-3-86727-223-0

Nonnenstieg 8, 37075 Göttingen
Telefon: 0551-54724-0
Telefax: 0551-54724-21
www.cuvillier.de

1. Auflage, 2007
Gedruckt auf säurefreiem Papier

978-3-86727-223-0

# Contents

# Chapter 1

# Introduction

What are colloids? The word origin *kolla* (glue) and *eidos* (form, shape) suggests to some extent the connection to the field of soft matter within statistical physics, but it does not capture the rich variety of phenomena and properties. The term *colloidal*, in general, describes a class of particles with size from a few nanometers to typically a few microns that are dispersed in a medium. More than one hundred years ago colloids played an important role in the development of the idea of the discontinuous structure of matter, or, that is to say to the existence of atoms. In 1905 A. Einstein predicted that small particles visible by a microscope due to thermal molecular motions are subject to Brownian motion [1]. A few years later J. Perrin experimentally confirmed the kinetic theory and thereby showed the existence of atoms [2]. From sedimentation experiments he could determine Avogadro's number $N_A$, or equivalently, the Boltzmann constant $k_B$. In 1926 J. Perrin and in 1925 R.A. Zsigmondy received the Nobel Prize for their work on the discontinuous structure of matter and the heterogenous nature of colloid solutions, respectively. In the following period, atoms, the quantum character of matter, and the nucleus became of increasing interest. It took several decades until the study of colloidal systems underwent a recent renaissance based on the development of experimental techniques, the availability of extensive computer simulations, and well-developed theoretical approaches. The latest developments allow one to consider colloids as model atoms [3,4] because they provide tunable interparticle interactions and the underlying length and time scales allow one to directly study aspects of atomic systems. Moreover, from a technological point of view, the relevance of micro- and nanostructured materials and the presence of colloids in nature and everyday life motivates study of this rich field. Colloids can be found, for instance, in paint, in blood, and in many industrial processes.

The solvent in which the colloidal particles are immersed can itself consist of a variety of particles such as atoms, ions, macromolecules, polymers, and other species of colloids. The interaction between the colloidal particles is affected by the properties of the solvent and can be described by an effective interaction that originates from integrating out the degrees of freedom of the solvent. This requires a good understanding of the solvent behavior to consider its contribution to the effective interaction. In order to achieve this, we study the behavior of mixtures of colloids such as spherical particles, polymer coils, needles and platelets in various situations: in the bulk we benefit from the model character of colloids and achieve a means to handle the tunable nature of their mutual interactions; at planar walls additional surface contributions give rise to further effects; in confinement the phase behavior of the fluid will affect the force on the confining walls; analogously, the solvent properties might strongly influence the interaction between two fixed big colloids at close distance.

From an experimental point of view, colloidal mixtures are of appealing size and well-developed experimental techniques allow one to synthesize and study particles of different size and shape. It is possible to choose particles that are matched in density and refractive index and to study systems with vanishing dispersion forces. Electrostatic or steric stabilization yields particles with a strong short-ranged repulsion and a weak long-ranged interaction. From a theoretical point of view, such colloids [5,6] are successfully described by the hard-core model. Hard-sphere fluids are widely studied and theory provides very accurate results when compared with computer simulations. One example is the equation of state for the one-component hard-sphere fluid [7,8]. The construction of a theory for mixtures is more demanding, particularly for mixtures of particles of different species. For mixtures of hard spheres and ideal polymer Asakura and Oosawa [9,10] and independently Vrij [11] introduced a successful model that serves as a starting-point for various approaches. Several different routes have been developed to describe the structure and thermodynamics of such mixtures. Density functional theory (DFT), integral equation theory and perturbation theory allow us to select an approach most suitable for a given physical situation. In DFT [12] the framework of fundamental measure theory (FMT) provides a successful reference model to treat particles with interactions that are dominated by strong repulsion [13]. Within FMT it is possible to add to the hard-sphere fluid additional species that together act as a depletion agent [14]. Upon integrating out the degrees of freedom of the depletion agent, the solvent effects can be mapped onto the effective interaction between the remaining particles. For hard-sphere solvents [15–18] and different kinds of soft particles [19–22] this method has been applied successfully. The effective one-component treatment in some cases is simpler to treat as compared to the full mixture and one may employ different routes which often involve a perturbation theory.

If the solvent is composed of a mixture of small colloids $c$, modeled as hard spheres, and ideal polymer $p$ the solvent exhibits phase separation between a colloid-rich and a colloid-poor phase. In such systems fluid–fluid demixing can be experimentally observed by confocal microscopy [23], and the rich phase behavior of mixtures of colloids and depletion agent has been observed by other experimental techniques [23–31]. When two big colloids of type $b$ are immersed into a colloid-polymer ($cp$) mixture then the mapping of the solvent onto an effective one-component system of particles of the species $b$ has to deal with a rich phenomenology. Computer simulations provide insight into the properties of colloidal mixtures, but if the particle sizes are highly asymmetric the different length and time scales of the problem lead to slow convergence and simulations have to be performed with care [32–34]. In contrast, density functional theory for such mixtures is well developed and various inhomogeneous situations, such as fluids near planar walls [22], confined in narrow slits [35] or in porous media [36] have been studied.

The phase behavior of the colloid-polymer ($cp$) mixture with monodisperse components is widely studied for various types of depletion agents [23,24,26–29,31,37–39] including spherical polymers, needles, and platelets. A pure hard-sphere fluid exhibits a fluid–solid phase separation at sufficiently high packing fractions [40]. Adding a depletion agent $d$ favors the phase separation and widens the region in the phase diagram with metastable and unstable states while the regions with the stable fluid and the stable solid phase shrink. Moreover, for mixtures of colloids (diameter $\sigma_c$) and a spherical depletion agent (diameter $\sigma_d$) with a symmetric size ratio $q = \sigma_d/\sigma_c \simeq 1$ a fluid–fluid phase separation is stable with respect to crystallization. By introducing polydispersity, i.e., species with a continuously varying size or shape distribution, the mixture shows even richer phase behavior that has been demonstrated in experiment [30, 41] and theory [42–50]. For the $cp$ mixture with monodisperse particles, a recent approach based on FMT [51] provides a good starting-point to introduce polydispersity because multi-component mixtures with different size or geometry can be considered from the outset. It is not known a priori how polydispersity, for example introduced by varying size or shape of the depletion agent particles, affects the phase behavior. By introducing different length scales the phase diagrams can possess two fluid–fluid critical points [52–55]. The distinct length scales are typically introduced directly via the interparticle interaction potential. Here, we address the question whether similar effects can be seen, if the length scales are introduced in terms of a bimodal size distribution of the depletion agent.

In contact with walls a colloid-polymer mixture exhibits a complex surface phase behavior. Within the Asakura-Oosawa-Vrij (AOV) model for the mixture for weak size asymmetry, a series of layering transitions and a wetting transition have been found [22]. When confined in narrow slit-like pores, depending on the interaction of the confining planar walls, a fluid can undergo capillary condensation [56–58] or evaporation [59, 60]. In experiments, narrow pores can be studied using the surface force apparatus [61,62] or two mica plates [63–65]. In theoretical calculations for the AOV model both capillary condensation and evaporation have been observed [35,66]. Combining the results for the AOV mixture at a single wall and in a narrow pore, we address the question in which range of the slit-width of the pore the various effects compete. One can expect a competition between the gas phase, the layering phase and the liquid phase. Since the confined fluid exerts an excess pressure on the confining walls, we study how the layering transitions and capillary condensation affect forces between the walls of a slit-like pore.

In order to study mixtures of different species one can in some cases consider the full mixture, i.e., each species explicitly. In many cases this approach is complicated and demanding. If one is mainly interested in the behavior of one component of the mixture then it is convenient to integrate out the degrees of freedom of the remaining species. Although this procedure is restricted to particular situations, e.g., asymmetric size ratios for hard-sphere mixtures, one ends up with a problem that is simpler to treat. The resulting effective interaction potentials between the remaining particles capture the influence of the solvent in addition to the direct interaction. Effective interactions between two particles or between a particle and a wall are widely studied for simple solvents. In the case of a hard-sphere solvent one obtains a depletion potential with oscillatory decay [18, 67]. In the case of an ideal polymer solvent, the interaction potential is of finite range and known even exactly [9,10]. The effective interaction potentials have been studied in other systems, e.g., for charged particles [68], for long-ranged and for soft interactions [19,69]. Once the effective interaction is known, integral equation techniques or perturbation theory can be employed to study the structure and the phase behavior of the effective one-component fluid.

For solvents with rich phase behavior the mapping onto an effective interaction potential is more complicated. The structure, the thermodynamic properties, and the phase behavior of the colloid-polymer mixture described by the AOV model of one colloid and one polymer component are widely studied. For that reason, the colloid-polymer mixture provides an appropriate model to introduce a complex solvent in a colloidal suspension of big particles. When a big colloid is brought close to a wall or a second big particle then the solvent-mediated interaction must reflect the rich behavior of the solvent and it is evident that integrating out the degrees of freedom of the solvent particles becomes a challenging task. In particular, near the phase coexistence of the solvent one will face rich phenomenology.

This thesis is structured as follows. In Chapter 2 we present a brief introduction into the basic principles used throughout the thesis, including some thermodynamic foundations, density functional theory with focus on fundamental measure theory, and free-volume theory. In Chapter 3 we present results for the bulk phase behavior of a mixture of colloids and a depletion agent. We also introduce a general approach in which the depletion agent can be polydisperse. In the case of bimodal distributions we find a novel phase and complex phase diagrams with two stable critical points. The phase behavior of a monodisperse colloid-polymer mixture in confined geometry is treated in Chapter 4. There we describe the competition between layering transitions found at a single hard wall and capillary condensation, which can be found in narrow slits. The influence of the solvent phase behavior on the interaction between the walls is also studied. The interaction between a big colloid and a planar hard wall in a solvent of an AOV mixture is presented in Chapter 5. We study the behavior of a colloid-polymer mixture close to phase coexistence near two big colloids and near one ellipsoidal particle in Chapter 6. We conclude in Chapter 7.

# Chapter 2

# Statistical Mechanics of Colloidal Mixtures

In this chapter we give an introduction to the framework and basic principles that we use for treating colloidal mixtures. Starting from the elementary grounds of equilibrium thermodynamics we describe their basic quantities and concepts. We briefly review density functional theory (DFT), which allows us to treat inhomogeneous classical fluid mixtures. Originally, DFT has been developed by Hohenberg and Kohn [70] to study electronic systems at temperature $T = 0$ and was generalized by Mermin [71] to non-zero, positive temperature, $T > 0$. Several approaches to describe non-uniform classical fluids, such as integral equation techniques, variational principles, diagram representations of the grand partition function expansions and cluster theory, have been developed at the same time [72–75] but it took more than ten years until the density functional formalism was introduced to describe inhomogeneous classical fluids [76, 77]. Refs. [12] and [78] give an excellent review to foundations of this topic and Ref. [79] provides a recent overview to a wide range of applications of density functional theory. One of the main issues within DFT is to find reliable approximations for the free energy that take into account the interparticle interactions. For a particular kind of colloids, which exhibit strong short-ranged repulsion and weak long-ranged interactions, the core contribution in the interparticle interaction potential can be modeled by a hard-core reference system and the potential tail can be treated in a perturbative manner [80]. For colloids with very weak or vanishing long-ranged interactions the pure hard-core model provides a suitable approximation. Within that model the temperature scales out, as $\beta V(r)$ only takes the values 0 or $\infty$, and the behavior of the system is driven by entropy. Mixtures of particles with hard-core potentials can be described within fundamental measure theory (FMT) going back to the work of Rosenfeld [13]. It is possible to base the FMT on different equations of state [67, 81–83]. We present an outline of the main ideas for that approach. Within the same framework we can add to the hard-sphere colloids another species, say a polymer substance or colloidal rods, which acts as a depletion agent [14, 84]. A recent approach [51] which combines FMT and the free-volume theory (FVT) allows us to treat bulk phase behavior of colloids in a sea of arbitrarily shaped depletion agent [37] and is presented at the end of this chapter.

## 2.1 Thermodynamics and phase transitions

From a phenomenological point of view classical statistical systems in equilibrium are described by a small number of variables. In the case of bulk, or equivalently homogeneous, systems such as colloidal mixtures of $\nu$ components $i$ connected to a heat bath and particle reservoirs the temperature $T$, the volume $V$ and the chemical potentials $\mu_i$ are sufficient. In the grand canonical ensemble the thermodynamic potential is given by

$$\Omega(T, V, \{\mu_i\}) = -pV, \tag{2.1}$$

where $p$ is the bulk pressure. In the canonical ensemble with fixed particle numbers $N_i$ the corresponding Helmholtz free energy $F(T, V, \{N_i\})$ is related to $\Omega$ by

$$\Omega = F - \sum_i \mu_i N_i. \tag{2.2}$$

In the description of colloids throughout the current work we focus on a model in which temperature scales out due to particle interaction potentials $\beta V_{ij}(r) = \infty$ in the range of $r < \sigma_{ij} = (\sigma_i + \sigma_j)/2$, where $\sigma_i$ is the diameter of component $i$, and 0 otherwise. The thermodynamic properties based on such type of interactions are determined by entropy alone. Hence we omit relations based on a variation of $T$. Both the grand potential $\Omega$ and the Helmholtz free energy $F$ play a central role in the description of the phase behavior of colloidal mixtures. In the homogeneous case the pressure $p$ and the chemical potentials $\mu_i$ are given by

$$p = -\frac{\partial F}{\partial V}\bigg|_{T,\{N_i\}} \tag{2.3}$$

and

$$\mu_i = \frac{\partial F}{\partial N_i}\bigg|_{T,V}. \tag{2.4}$$

Two different bulk phases $\alpha$ and $\beta$, which for example differ from each other by their densities $\rho_i = N_i/V$, $i = \alpha, \beta$, can coexist if their pressures and chemical potentials are equal: $p^\alpha = p^\beta$ and $\mu_i^\alpha = \mu_i^\beta$. The equation of state describes the relation between the pressure and the density. For a one-component hard-sphere system the following equations of state proved to be successful. The one-component Percus-Yevick (PY) compressibility equation of state [7] in terms of the packing fraction $\eta = (\pi/6)\sigma^3\rho$ of the colloids is given by

$$\beta\, p_{PY} = \rho\, \frac{1+\eta+\eta^2}{(1-\eta)^3}, \tag{2.5}$$

and the more accurate Carnahan-Starling (CS) equation of state reads [85]

$$\beta\, p_{CS} = \rho\, \frac{1+\eta+\eta^2-\eta^3}{(1-\eta)^3}. \tag{2.6}$$

The CS equation of state and its generalization to mixtures yields better agreement with simulations than the PY equation of state, especially at sufficiently high values of $\eta$ and for multi-component mixtures. The corresponding chemical potentials can be obtained via the Maxwell relation, $(\partial\mu_i/\partial V)_T = -(\partial p/\partial N_i)_T$. In the following we consider a single-component colloidal system in a sea of depletion agents. Those are particles that mimic polymer coils or colloids of different shape such as needles or platelets. After integrating out their degrees of freedom the colloids interact via an effective interaction, the so-called depletion potential. The depletion agent is connected to a reservoir and its density in the reservoir plays the role of the inverse temperature.

In Fig. 2.1 a sketch of the phase diagram of a colloid-polymer mixture is shown in the $(\eta_c,\eta_d^r)$-representation where $\eta_c = (\pi/6)\sigma_c^3\rho_c$ is the packing fraction of the colloids and $\eta_d^r = (\pi/6)\sigma_d^3\rho_d^r$ is the reservoir packing fraction of the depletion agent modeling the polymer. At low values of $\eta_d^r$ we find a stable fluid and a stable solid. The fluid–solid coexistence is indicated by the full lines in the region of large values of $\eta_c$. For values above the critical point (full circle) the fluid can phase-separate into a gas (G) and a liquid (L) phase. The full line near the critical point shows the fluid–fluid coexistence line. In the representation chosen in Fig. 2.1, state-points at that line which are connected by horizontal tie lines coexist. The thermodynamic stability of the system can be expressed in terms of an inequality [37]

$$\frac{\partial^2 F}{\partial N^2}\bigg|_{T,V} = \frac{\partial \mu}{\partial N}\bigg|_{T,V} = \frac{V}{N^2}\frac{1}{\kappa_T} \geq 0, \tag{2.7}$$

with the isothermal compressibility $\kappa_T$. The region with non-stable states w.r.t. fluid–fluid phase separation, i.e., $\kappa_T < 0$, is bound by the spinodal line (dashed line). At sufficiently high values of $\eta_d^r$ one finds three coexisting states. At the triple point (indicated by the dotted line) we find the gas (poor in colloid, but rich in polymer), the liquid (rich in colloid, but poor in polymer) and the solid (S) phase.

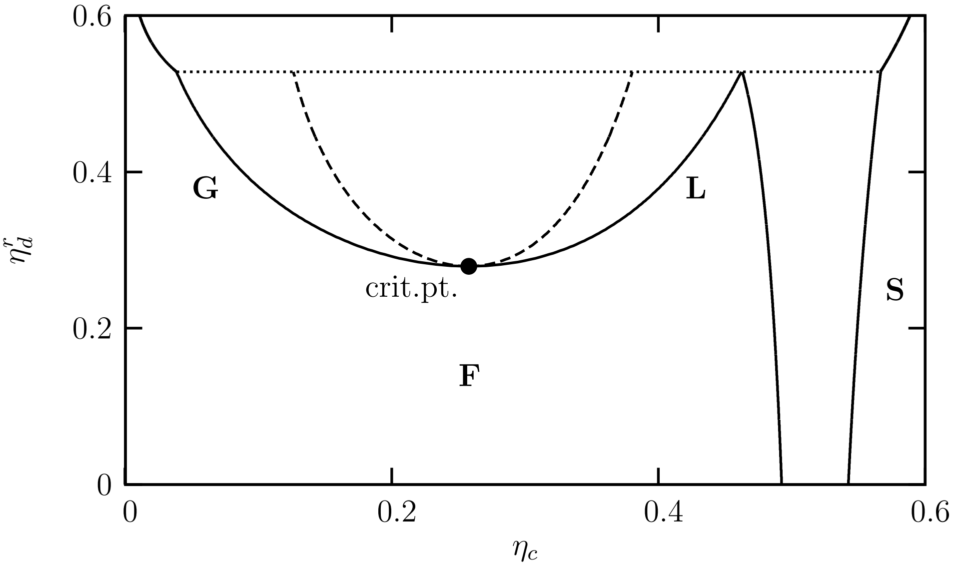

Figure 2.1: Sketch of a phase diagram of a colloidal $c$ suspension in a sea of depletion agent $d$ which one can for example obtain within the framework of free-volume theory. The packing fractions $\eta_d^r$ of the depletion agent in the reservoir plays the role of the inverse temperature. For low values of $\eta_d^r$ a fluid (F) and a solid (S) phase are stable. At intermediate values of $\eta_d^r$ a colloid rich phase (liquid, L), a colloid poor phase (gas, G) and the colloidal solid phase are stable. The dotted tie line connects the three coexisting state points at the triple point, the full circle shows the position of the critical point. The full lines denote coexistence lines while the dotted line (spinodal) encloses the region with non-stable state-points, the spinodal region.

If the system is subjected to an external potential, which can model a fixed particle or a confining geometry, the density distribution $\rho_i(\mathbf{r})$ is no longer constant. Due to the confinement the centers of the fluid particles can take the values of a set of points which we refer to as the system $S$ [86]. The grand potential $\Omega$ in the fluid phase away from the critical point and away from wetting or drying transitions are, for short-ranged external potentials, well approximated by the form [86]

$$\Omega[S] = -pV[S] + \sigma A[S] + \kappa C[S] + \bar{\kappa} X[S], \tag{2.8}$$

with $\sigma$ the surface tension at the planar wall and the bending rigidities $\kappa$ and $\bar{\kappa}$. The corresponding geometrical measures are the volume $V[S]$ of the system and the surface area $A[S]$, the integrated mean curvature $C[S]$ and the Euler characteristic $X[S]$ of the system walls. It is important to note that this description holds when the system is sufficiently big as compared to the length scales of the fluid particles, correlations or interactions.

An excess quantity that describes the inhomogeneity caused by $S$ is the excess surface grand potential per unit area

$$\gamma = \frac{1}{A}(\Omega_{inh.} - \Omega_b) \tag{2.9}$$

and the excess adsorption

$$\Gamma_i = -\frac{\partial \gamma}{\partial \mu_i}\Big|_{T,V} = \frac{1}{A}\int_V \mathrm{d}\mathbf{r}\,(\rho_i(\mathbf{r}) - \rho_i), \tag{2.10}$$

which in its general form follow directly from Eqs. (2.9) and (2.8). $\Omega_{inh.}$ denotes the grand potential of the inhomogeneous system whereas $\Omega_b = -pV$ describes the bulk fluid.

Phase coexistence between two phases $\alpha$ and $\beta$ of a fluid in confined geometry, e.g., for a fluid in a slit-like pore of two parallel planar plates, occurs if the grand potential and the chemical potentials are equal [58,87], $\Omega^\alpha = \Omega^\beta$ and $\mu_i^\alpha = \mu_i^\beta$. Fluids at surfaces or in confined geometry can exhibit rich and more complex phase behavior as compared to bulk.

## 2.2 Density functional theory

We describe a classical system of $N$ identical particles in an external field by its Hamiltonian $H_N = T_{kin} + U + V_{ext}$, which is composed of the kinetic energy $T_{kin}$, a term describing the interactions $U$ between the particles and one term for the external potential $V_{ext}$. The generalization to mixtures of different particles is straightforward. In this section we focus on the one-component system to highlight the basic principles. Thermodynamic quantities of the system follow from the partition function $\Xi$. In phase space $(q^{3N}, p^{3N})$ with the canonical variables $q_i$ and $p_i$, the equilibrium probability density is given by $f_0 = \frac{1}{\Xi}\exp\left(-\beta(H_N - \mu N)\right)$, where $\Xi = \mathrm{Tr}_{cl}\exp\left(-\beta(H_N - \mu N)\right)$ and the classical trace $\mathrm{Tr}_{cl}$ can be written as

$$\mathrm{Tr}_{cl} \equiv \sum_{N=0}^{\infty} \frac{1}{N!h^{3N}} \int \mathrm{d}q_1 \ldots \mathrm{d}q_{3N}\, \mathrm{d}p_1 \ldots \mathrm{d}p_{3N}, \tag{2.11}$$

where $h^3$ is a unit of phase volume in the phase space. We consider the following functional of the probability density $\bar{\Omega}[f]$ and find [12]

$$\bar{\Omega}[f] = \mathrm{Tr}_{cl} f\left(H_N - \mu N + \beta^{-1}\ln f\right), \tag{2.12}$$

which, for the equilibrium distribution $f_0$, equals the grand potential of the system $\Omega = \bar{\Omega}[f_0] = -\beta^{-1}\log\Xi$. For any other distribution $f \neq f_0$ one finds $\Omega[f] \geq \Omega[f_0]$. Given a Hamiltonian of the form introduced above one can show that the equilibrium probability density $f_0$ is a unique functional of the equilibrium one-particle density $\rho_0(\mathbf{r})$. Accordingly, the system is completely described by the functional $\Omega[\rho]$ which depends on the density distribution $\rho(\mathbf{r})$,

$$\Omega[\rho(\mathbf{r})] = \mathcal{F}[\rho(\mathbf{r})] + \int \mathrm{d}\mathbf{r}\, \rho(\mathbf{r})(V_{ext}(\mathbf{r}) - \mu). \tag{2.13}$$

$\mathcal{F}[\rho(\mathbf{r})]$ denotes the intrinsic Helmholtz free energy. In equilibrium, the minimum property for $\Omega[\rho]$ gives rise to the variational principle

$$\frac{\delta\Omega[\rho(\mathbf{r})]}{\delta\rho(\mathbf{r})}\Big|_{\rho_0(\mathbf{r})} = 0 \tag{2.14}$$

and, accordingly,

$$\frac{\delta\mathcal{F}[\rho(\mathbf{r})]}{\delta\rho(\mathbf{r})}\Big|_{\rho_0(\mathbf{r})} = \mu - V_{ext}(\mathbf{r}). \tag{2.15}$$

We divide the Helmholtz free energy into two terms

$$\mathcal{F}[\rho(\mathbf{r})] = \mathcal{F}_{id}[\rho(\mathbf{r})] + \mathcal{F}_{ex}[\rho(\mathbf{r})]. \tag{2.16}$$

The ideal gas contribution $\mathcal{F}_{id}$ is known exactly,

$$\beta\mathcal{F}_{id}[\rho(\mathbf{r})] = \int \mathrm{d}\mathbf{r}\, \rho(\mathbf{r}) \left(\ln(\lambda^3\rho(\mathbf{r})) - 1\right), \tag{2.17}$$

with the thermal wavelength $\lambda = \sqrt{\beta h^2/2m\pi}$ of a particle of mass $m$. The excess (over ideal gas) contribution $\mathcal{F}_{ex}$ contains the interactions between the particles. We present a general approach to treat mixtures of hard spheres and ideal polymer within DFT in the following section.

## 2.3 Fundamental measure theory

In nature colloidal particles appear in a great variety and their interparticle interactions may be described by different potentials. For spherical colloids which are immersed in a molecular fluid and which feature a strong short-ranged repulsion and a weak long-ranged interaction, the hard-sphere model represents a suitable reference system. The interaction potential between two spheres of species $i$ and $j$ with diameters $\sigma_i$ and $\sigma_j$, respectively, is described by

$$\beta V_{ij}(\mathbf{r}_{ij}) = \begin{cases} \infty, & |\mathbf{r}_{ij}| < (\sigma_i + \sigma_j)/2, \\ 0, & \text{otherwise.} \end{cases} \tag{2.18}$$

The density functional in the low density limit is known exactly,

$$\lim_{\rho_i \to 0} \beta\mathcal{F}_{ex}[\{\rho_i(\mathbf{r})\}] = -\frac{1}{2}\sum_{ij} \int \mathrm{d}\mathbf{r} \int \mathrm{d}\mathbf{r}'\, \rho_i(\mathbf{r})\rho_j(\mathbf{r}') f_{ij}(\mathbf{r} - \mathbf{r}'). \tag{2.19}$$

We use this finding as a starting-point for the construction of the density functional for finite densities, $\rho_i > 0$. The Mayer-f function, $f_{ij}(\mathbf{r}) = \exp(-\beta V_{ij}(\mathbf{r})) - 1$, for hard-sphere mixtures is given by

$$\begin{aligned} f_{ij}(\mathbf{r}) &= \begin{cases} -1, & |\mathbf{r}_{ij}| < (\sigma_i + \sigma_j)/2, \\ 0, & \text{otherwise}, \end{cases} && (2.20) \\ &= -\Theta((\sigma_i + \sigma_j)/2 - |\mathbf{r}_i - \mathbf{r}_j|), && (2.21) \end{aligned}$$

where $\Theta(x)$ denotes the Heaviside function. We take into account the limit of the two-body direct correlation function $c_{ij}^{(2)}(r)$ at low densities and we extrapolate to higher densities using thermodynamic relations into quantities that depend on the geometry of a single species only. This is achieved by [13]

$$\begin{aligned} \Theta((\sigma_i + \sigma_j)/2 - |\mathbf{r}_i - \mathbf{r}_j|) &= w_i^{(3)} \otimes w_j^{(0)} + w_i^{(2)} \otimes w_j^{(1)} + w_i^{(1)} \otimes w_j^{(2)} \\ &+ w_i^{(0)} \otimes w_j^{(3)} - \mathbf{w}_i^{(2)} \otimes \mathbf{w}_j^{(1)} - \mathbf{w}_i^{(1)} \otimes \mathbf{w}_j^{(2)}, \end{aligned} \qquad (2.22)$$

where the four scalar functions $w_i^{(\alpha)}$ and the two vector functions $\mathbf{w}_i^{(\alpha)}$ are given by

$$\begin{aligned} w_i^{(3)}(\mathbf{r}) &= \Theta(\sigma_i/2 - |\mathbf{r}|), \\ w_i^{(2)}(\mathbf{r}) &= \delta(\sigma_i/2 - |\mathbf{r}|), \\ w_i^{(1)}(\mathbf{r}) &= \frac{1}{2\pi\sigma_i} w_i^{(2)}(\mathbf{r}), \\ w_i^{(0)}(\mathbf{r}) &= \frac{1}{\pi\sigma_i^2} w_i^{(2)}(\mathbf{r}), \\ \mathbf{w}_i^{(2)}(\mathbf{r}) &= \frac{\mathbf{r}}{|\mathbf{r}|} \delta(\sigma_i/2 - |\mathbf{r}|), \\ \mathbf{w}_i^{(1)}(\mathbf{r}) &= \frac{1}{2\pi\sigma_i} \mathbf{w}_i^{(2)}(\mathbf{r}). \end{aligned} \qquad (2.23)$$

The convolution of in each case two scalar or two vector functions is defined as follows

$$w_i^{(\alpha)} \otimes w_j^{(\beta)} \equiv \int \mathrm{d}\mathbf{x}\, w_i^{(\alpha)}(\mathbf{r}_i - \mathbf{x}) \cdot w_j^{(\beta)}(\mathbf{r}_j - \mathbf{x}). \qquad (2.24)$$

After inserting the Mayer-f function into the low density expression we extract a composition of terms of the following form

$$n_\alpha(\mathbf{r}) = \sum_{i=1}^{\nu} \int \mathrm{d}\mathbf{r}'\, \rho_i(\mathbf{r}')\, w_i^{(\alpha)}(\mathbf{r} - \mathbf{r}'). \qquad (2.25)$$

Those are called the weighted densities $n_\alpha$. Accordingly to the structure of the weight functions we have four scalar and two vector-valued functions with dimension

$[n_\alpha] = (\text{length})^{\alpha-3}$. Rosenfeld introduced the approximation for the excess free energy based on a function $\Phi$ depending on the set of weighted densities $\{n_\alpha(\mathbf{r})\}$

$$\beta\mathcal{F}_{ex}[\{\rho_i(\mathbf{r})\}] = \int \mathrm{d}\mathbf{r}\, \Phi(\{n_\alpha(\mathbf{r})\}). \tag{2.26}$$

We note that besides the decomposition Eq. (2.22) with the weight functions introduced above in Eq. (2.23), it is also possible to decompose the Heaviside function from Eq. (2.21) with different weight functions that do not contain vector-valued expressions [88, 89], but involve derivatives of the $\delta$-functions instead. Obtaining an explicit expression for $\Phi(\{n_\alpha\})$ requires to commit oneself to further approximations. To obtain the functional for hard spheres we can use the structure of the exact one-dimensional functional of hard-rod mixtures [90, 91]. An approximate expression for the function $\Phi(\{n_\alpha(\mathbf{r})\})$ for spherical particles can be obtained from various approaches. Rosenfeld's original formulation [13] employs the dimensional ansatz $\Phi(\{n_\alpha\}) = f_1 n_0 + f_2 n_1 n_2 + f_3\,(\mathbf{n}_1\cdot\mathbf{n}_2) + f_4 n_2^3 + f_5 n_2\,(\mathbf{n}_2\cdot\mathbf{n}_2)$. The coefficient functions $f_0, f_1, f_2, f_3$ and $f_5$ which depend only on $n_3$ follow by considering the excess chemical potential in the limit $\lim_{R_i\to\infty}\mu_i/V_i$ which, according to the scaled particle theory (SPT), must be equal to the total pressure inside the system. This results in SPT differential equations. The integration constants can be fixed when considering the low density, Eq. (2.19), and the (three-body diagram in the) two-body direct correlation function $c_{ij}^{(2)}(r)$ which must be regular for $r \to 0$. The final result is given by

$$\Phi(\{n_\alpha\}) = -n_0\ln(1-n_3) + \frac{n_1 n_2 - \mathbf{n}_1\mathbf{n}_2}{1-n_3} + \frac{n_2^3 - 3n_2(\mathbf{n}_2\cdot\mathbf{n}_2)}{24\pi(1-n_3)^2}. \tag{2.27}$$

The equation of state that follow from the above expression corresponds to the Percus-Yevick compressibility equation of state. A more accurate approach, which is based on the Mansoori-Carnahan-Starling-Leland (MCSL) equation of state, yields [67]

$$\begin{aligned}\Phi_{WB}(\{n_\alpha\}) &= -n_0\ln(1-n_3) + \frac{n_1 n_2 - \mathbf{n}_1\mathbf{n}_2}{1-n_3}\\ &\quad+\frac{n_2^3 - 3n_2(\mathbf{n}_2\cdot\mathbf{n}_2)}{36\pi n_3^2(1-n_3)^2}\left(n_3 + (1-n_3)^2\ln(1-n_3)\right).\end{aligned} \tag{2.28}$$

From the excess free energy functional we can obtain a whole hierarchy of $n$-body correlation functions

$$c^{(n)}(\mathbf{r}_1,\ldots,\mathbf{r}_n) = \frac{\delta c^{(n-1)}(\mathbf{r}_1,\ldots,\mathbf{r}_{n-1})}{\delta\rho(\mathbf{r}_n)} = -\beta\frac{\delta^n\mathcal{F}_{ex}[\rho(\mathbf{r})]}{\delta\rho(\mathbf{r}_n)\ldots\delta\rho(\mathbf{r}_1)}. \tag{2.29}$$

The one-body correlation function can be regarded as an effective potential.

The density functional Eq. (2.13) within FMT, Eq. (2.26), is given by

$$\Omega[\{\rho_i(\mathbf{r})\}] = \beta^{-1}\int \mathrm{d}\mathbf{r}\,\Phi(\{n_\alpha(\mathbf{r})\}) + \mathcal{F}_{id}[\{\rho_i(\mathbf{r})\}] + \sum_i\int \mathrm{d}\mathbf{r}\,\rho_i(\mathbf{r})(V_{ext}^i(\mathbf{r}) - \mu_i), \tag{2.30}$$

with the ideal gas contribution $\beta\mathcal{F}_{id}[\{\rho_i(\mathbf{r})\}] = \sum_i \int \mathrm{d}\mathbf{r}\, \rho_i(\mathbf{r})\, (\ln(\lambda_i^3 \rho_i(\mathbf{r})) - 1)$ for mixtures. Having an explicit expression for the free energy density $\Phi$, it is now possible to calculate $\rho(\mathbf{r})$ by minimizing the grand potential $\Omega[\rho(\mathbf{r})]$ for arbitrary external potential.

An important finding is that the effective potential between particles of one species $b$ of the mixture, which results from integrating out the degrees of freedom of the remaining components $i \neq b$, can be expressed in an elegant fashion via the insertion method [18]. The depletion potential in terms of the one-body direct correlation functions is given by

$$\beta W(\mathbf{r}) = \left( c_b^{(1)}(\mathbf{r} \to \infty) - c_b^{(1)}(\mathbf{r}) \right)_{\{\mu_{i \neq b}\}, \mu_b \to -\infty}. \tag{2.31}$$

From the definition Eq. (2.29) and the knowledge of the free energy density $\Phi(\{n_\alpha\})$ the direct correlation function yields

$$c_b^{(1)}(\mathbf{r}) = -\sum_\alpha \int \mathrm{d}\mathbf{r}' \, \frac{\beta \partial \Phi(\{n_\alpha\})}{\partial n_\alpha(\mathbf{r}')} w_b^\alpha(\mathbf{r}' - \mathbf{r}). \tag{2.32}$$

It is important to notice that the density profiles at the particle fixed in the origin which enter the weighted densities describe the system before insertion of the particle at position $\mathbf{r}$.

### Hard-Spheres and Depletion Agent

Based on the excess free energy density for hard-sphere mixtures we can also derive an expression for a mixture of hard-sphere colloids ($c$) and an *ideal depletion agent* ($d$). The interaction potentials are given by

$$\beta V_{ij}(\mathbf{r}_{ij}) = \begin{cases} \infty, & |\mathbf{r}_{ij}| < (\sigma_i + \sigma_j)/2 \\ 0, & \text{otherwise,} \end{cases} \tag{2.33}$$

for $ij = cc, cd, dc$, i.e., the colloid-colloid and colloid-depletion agent interaction is described by pure hard-core repulsion (see Fig. 2.2). The interaction between particles of the depletion agent vanishes

$$\beta V_{dd}(\mathbf{r}_{dd}) = 0, \tag{2.34}$$

such that they can overlap freely. The diagrammatic expansion of the two-body direct correlation function $c_{ij}^{(2)}(r)$ up to second order in the density contains the following information: $c_{cc}^{(2)}(r)$ is linear in the density $\rho_d$ of the depletion agent [84]

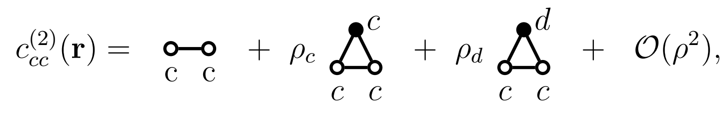

$$c_{cc}^{(2)}(\mathbf{r}) = \quad + \rho_c \quad + \rho_d \quad + \mathcal{O}(\rho^2), \tag{2.35}$$

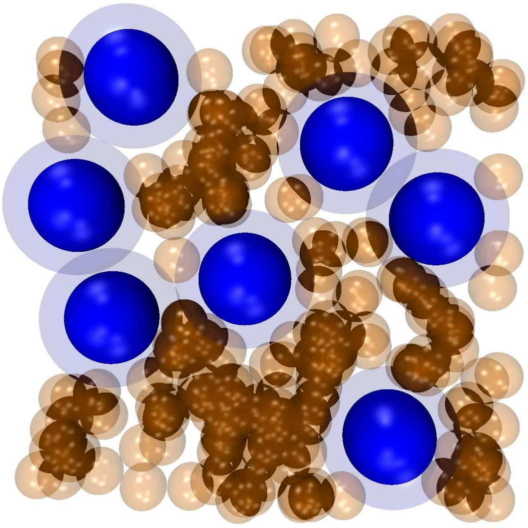

Figure 2.2: Sketch of a model mixture of colloids and depletion agent within the AOV model. The big dark particles (colloids) cannot overlap, while the smaller particles, the depletion agent, may overlap freely among themselves. The light shell around a colloid shows the volume excluded to the depletion agent. In this example the size ratio between the spherical depletion agent and the colloid is $\sigma_d : \sigma_c = 1 : 2$.

$c^{(2)}_{cd}(r)$ and $c^{(2)}_{dc}(r)$ are independent of $\rho_d$

$$c^{(2)}_{cd}(\mathbf{r}) =$$

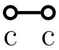

$$+ \; \rho_c$$

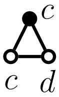

$$+ \; \mathcal{O}(\rho^2), \qquad (2.36)$$

and $c^{(2)}_{dd}(r)$ vanish to first order in $\rho$:

$$c^{(2)}_{dd}(\mathbf{r}) = 0 + \mathcal{O}(\rho^2). \qquad (2.37)$$

The full symbols denote coordinates of integration and all symbols are connected by Mayer-f bonds [92]. The determination of the higher order coefficients in the expansions, Eqs. (2.35)-(2.37), is a difficult task and based on the truncation of the expansion after the second order, or equivalently third virial level, a simple choice for the Helmholtz free energy is apparent. For the mixture of colloids and depletion agent the total weighted densities are defined as $n_\alpha = n^c_\alpha + n^d_\alpha$ with now two different sets of weighted densities $\{n^c_\alpha\}$ and $\{n^d_\alpha\}$. The linearization of the hard-sphere mixture free energy w.r.t. the density of the depletion agent gives the following expression [14, 84]

$$\Phi^{\mathrm{AOV}}(\{n^c_\alpha\},\{n^d_\alpha\}) \;=\; \Phi^{\mathrm{HS}}(\{n^c_\alpha\}) + \sum_{\beta=0,1,2,3,\mathbf{1},\mathbf{2}} \frac{\partial\Phi(\{n^c_\alpha\})}{\partial n^c_\beta} \cdot n^d_\beta, \qquad (2.38)$$

and the resulting Helmholtz free energy is given by

$$\beta\mathcal{F}_{ex}[\{\rho_i^c(\mathbf{r}),\rho_i^d(\mathbf{r})\}] = \int \mathrm{d}\mathbf{r}\,\Phi^{\mathrm{AOV}}(\{n_\alpha^c(\mathbf{r}),n_\alpha^d(\mathbf{r})\}). \tag{2.39}$$

For the Rosenfeld formulation, Eq. (2.27), and within the White Bear version of the free energy, Eq. (2.28), the second derivatives in Eq. (2.29), $c_{ij}^{(2)}(r)$, possess the properties required for the present interaction potential, Eqs. (2.35)-(2.37). For the mixture of different species the variational principle yields two equations

$$\frac{\delta\Omega[\rho_c,\rho_d]}{\delta\rho_c(\mathbf{r})} = 0, \quad \text{and} \quad \frac{\delta\Omega[\rho_c,\rho_d]}{\delta\rho_d(\mathbf{r})} = 0, \tag{2.40}$$

which must be solved simultaneously.

## 2.4 Free-volume theory

To describe the phase behavior of colloidal mixtures we consider a system with a fixed number of big spherical colloidal particles $N_c$ that is coupled to a reservoir of depletion agent at chemical potential $\mu_d$ or fugacity $z_d = e^{\beta\mu_d}$, respectively [37]. In this description the mixture of colloids and depletion agent is treated within the semi-grand canonical ensemble [93]. The density $\rho_d^r$ of the depletion agent in the reservoir is fixed and the corresponding density in the system, $\rho_d$, depends on the free volume available to the depletion agent or equivalently on the occupation by the colloids, $\rho_d = \rho_d(\rho_c)$. The Helmholtz free energy is given by

$$\mathcal{F}_{ex}^{\mathrm{AOV}}[\rho_c,\rho_d] = \mathcal{F}_{ex}^{\mathrm{AOV}}([\rho_c];z_d). \tag{2.41}$$

The latter can be decomposed into two terms,

$$\beta F(N_c,V,z_d) = \beta F(N_c,V,z_d=0) + \int_0^{z_d} \mathrm{d}z_d' \left(\frac{\partial\beta F(N_c,V,z_d')}{\partial z_d'}\right), \tag{2.42}$$

where the first term denotes the contribution of pure colloids. By Taylor expansion of the integrand of the second term in Eq. (2.42) up to first order in $z_d$ we obtain an expression for the volume available to the depletion agent particles in a system of $N_c$ colloids at low concentrations of the depletion agent, the so-called *free volume* denoted by $\alpha V$. In this limit of small fugacity of the depletion agent, we can rewrite Eq. (2.42) as

$$\beta F(N_c,V,z_d) = \beta F_0(N_c,V) - \rho_d^r(z_d)\alpha V, \tag{2.43}$$

where $\rho_d^r$ is the reservoir density of the depletion agent. Within the AOV model the free-volume fraction $\alpha$ depends only on the geometry of the depletion agent, e.g., the size ratio $q = \sigma_d/\sigma_c$ if the depletion agent consists of spherical polymer coils, and on the packing fraction of the colloidal spheres, $\eta_c = \pi\sigma_c^3 N_c/(6V)$.

For the calculation of the phase diagram of the colloidal mixture we need the chemical potential of the colloid component $\mu_c$ and its osmotic pressure $p$. In the bulk two phases $\alpha$ and $\beta$ coexist if they are in chemical and mechanical equilibrium, i.e., if $\mu_c^\alpha = \mu_c^\beta$ and $p^\alpha = p^\beta$. The chemical potential $\mu_c$ and the pressure $p$ follow from the Helmholtz free energy via [37]

$$\mu_c = \left.\frac{\partial F}{\partial N_c}\right|_{V,z_d} = \mu_0(\eta_c) - \rho_d^r(z_d)\left(\frac{\partial\alpha}{\partial\eta_c}\right)\frac{\pi\sigma_c^3}{6} \tag{2.44}$$

and

$$p = -\left.\frac{\partial F}{\partial V}\right|_{N_c,z_d} = p_0(\eta_c) + \rho_d^r(z_d)\left(\alpha - \eta_c\frac{\partial\alpha}{\partial\eta_c}\right). \tag{2.45}$$

The chemical potential and the pressure of the pure reference system, labeled by $\mu_0$ and $p_0$, are described accurately by the Carnahan-Starling expressions in the fluid phase. To assure thermodynamic consistency the free-volume fraction $\alpha$ must also be calculated from the equation of state of the reference system, i.e., the Carnahan-Starling equation of state [51]. Besides coexisting fluid states, i.e., points on the binodal line in phase diagram, we calculate the spinodal line which separates metastable states from thermodynamically unstable ones (see Fig. 2.1). For thermodynamically unstable states the second derivative of the Helmholtz free energy w.r.t. the colloid packing fraction $\eta_c$ is negative and for points on the spinodal line it vanishes,

$$\frac{\partial^2 F}{\partial\eta_c^2} = 0. \tag{2.46}$$

For the fluid–solid coexistence we need the chemical potential and the equation of state of a reference (fcc) hard-sphere crystal, which is described by [94]

$$\beta\mu_0 = 2.1306 + 3\ln\left(\frac{\eta_c\eta_{cp}}{\eta_{cp}-\eta_c}\right) + \frac{3\eta_{cp}}{\eta_{cp}-\eta_c} \tag{2.47}$$

with $\eta_{cp} = \pi\sqrt{2}/6 \approx 0.74$, the packing fraction for close packing, and [95]

$$\beta p_0 v_s = \frac{3\eta_c\eta_{cp}}{\eta_{cp}-\eta_c}. \tag{2.48}$$

### Fundamental Measure Approach within Free Volume Theory

For discrete mixtures of two species the excess Helmholtz free energy density in bulk, $\Phi = \beta F/V$, is constructed from two sets of weighted densities $\{n_i^c\}$ and $\{n_i^d\}$, one for the colloids $c$ and one for the depletion agent $d$. In homogeneous bulk fluids $i$ labels four scalar weighted densities in contrast to inhomogeneous fluids where $\alpha$ denotes additionally two vector-valued weighted densities. The weighted densities for the bulk case can be identified as the scaled-particle theory variables $\zeta_i$ of the $N$-component mixture [13, 96, 97]

$$n_i \equiv \zeta_i = \sum_{\nu=1}^{N} g_\nu^{(i)} \rho_\nu. \tag{2.49}$$

The geometrical measures of component $\nu$ are the volume $g_\nu^{(3)} \equiv v_\nu$, the surface area $g_\nu^{(2)} \equiv a_\nu$, the integrated mean curvature $g_\nu^{(1)} \equiv c_\nu$ and the Euler characteristic $g_\nu^{(0)} \equiv X_\nu$.

The expression for the bulk free energy density of the colloidal mixture in the limit of low density of the depletion agent (AOV) can be obtained by expanding the hard-sphere mixture free energy with weighted densities $n_i = n_i^c + n_i^d$ up to linear order in the density $\rho_d$. We show the result for the bulk mixture explicitly as it will be used in the following chapter,

$$\Phi^{\mathrm{AOV}}(\{n_i^c\}, \{n_i^d\}) \;=\; \Phi^{\mathrm{HS}}(\{n_i^c\}) + \sum_{k=0}^{3} \frac{\partial \Phi(\{n_i^c\})}{\partial n_k^c} n_k^d. \tag{2.50}$$

In order to relate the terms in Eq. (2.50) to the free-volume fraction $\alpha$ we transform the excess Helmholtz free energy density, which is given in Eq. (2.42) in the semi-grand canonical ensemble, into the canonical ensemble and obtain in terms of the colloid packing fraction $\eta_c$ and the density $\rho_d$

$$\Phi(\eta_c, \rho_d; q) = \Phi(\eta_c) - \rho_d \ln\left(\alpha(\eta_c; q)\right). \tag{2.51}$$

By direct comparison of Eq. (2.50) and Eq. (2.51) we obtain a FMT expression for the free-volume fraction [51]

$$\alpha(\eta_c; \{g_\nu^{(i)}\}) = \exp\left( - \sum_{k=0}^{3} \frac{\partial \Phi(\{n_i^c\})}{\partial n_k^c} \, g_d^{(k)} \right). \tag{2.52}$$

The partial derivatives of the free energy w.r.t. the weighted densities are thermodynamic quantities of the (pure) colloids, namely, the pressure $p_0$, the surface tension $\sigma$ at a planar hard wall and the bending rigidities $\kappa$ and $\bar{\kappa}$, which describe the effect on the free energy due to curved interfaces. The depletion agent enters the expression for the free-volume fraction $\alpha$ only through its geometrical measures $g_d^{(k)}$. For the free energy density we employ Rosenfeld's original formulation of FMT [13] and the more accurate White Bear version from Ref. [67, 81]

$$\Phi(\{n_i\}) \;=\; -n_0 \ln(1-n_3) + \frac{n_1 n_2}{1-n_3} + \frac{n_2^3 \left(n_3 + (1-n_3)^2 \ln\left(1-n_3\right)\right)}{36\pi n_3^2 (1-n_3)^2}, \tag{2.53}$$

which is based on the Boublik-Mansoori-Carnahan-Starling-Leland (BMCSL) equation of state [8, 98]

$$\beta p_{BMCSL} = \frac{n_0}{1-n_3} + \frac{n_1 n_2}{(1-n_3)^2} + \frac{n_2^3}{12\pi(1-n_3)^3} - \frac{n_3 n_2}{36\pi(1-n_3)^3}. \tag{2.54}$$

Note that Eq. (2.53) results from Eq. (2.28) in the bulk limit, i.e., for homogeneous densities. In this case the vector-valued weighted densities vanish, $\mathbf{n}_1(\mathbf{r}) = 0$ and $\mathbf{n}_2(\mathbf{r}) = 0$.

# Chapter 3

# Bulk Phase Behavior

Colloidal suspensions modeled as one-component hard-sphere systems crystallize at high densities [40] despite the fact that the interactions between the fluid particles are purely repulsive. Moreover, if depletion agent is added the mixture can phase separate into a (colloidal) gas and a (colloidal) liquid phase — see Fig. 2.1 for a sketch. Figures 3.1 and 3.2 display results for mixtures of colloids and spherical depletion agent. Still in this system all mutual particle interactions are purely repulsive. This simple two-component model already shows quite rich phase behavior. In the present approach we employ the combination of free-volume theory with fundamental measure theory. Constructed for discrete mixtures we generalize this technique to continuous distributions of the depletion agent. For one- and two-dimensional depletion agents we give explicit expressions that play a central role within FVT. For the three-dimensional particles we show numeric results for different ways of introducing polydispersity, i.e., size- and morphology-polydispersity, and discuss the effect of fractionation. We apply the general approach to ternary mixtures of one (monodisperse) colloidal species and two polymer components. The latter are introduced by a bimodal or a bidisperse distribution. By fine tuning the distributions we present phase diagrams that exhibit two stable critical points and richer phase behavior as compared to monodisperse distributions.

## 3.1 Generalization to polydispersity

Fundamental measure theory is by construction a theory to treat mixtures. We introduced its basic principles in Sec. 2.3 and presented the free-volume approach based on its bulk expressions in Sec. 2.4. For mixtures of colloids and ideal depletion agent we now employ multiple parameters $q_i$ to parameterize the geometry of particles of the depletion agent components. Although it is straightforward within FMT to

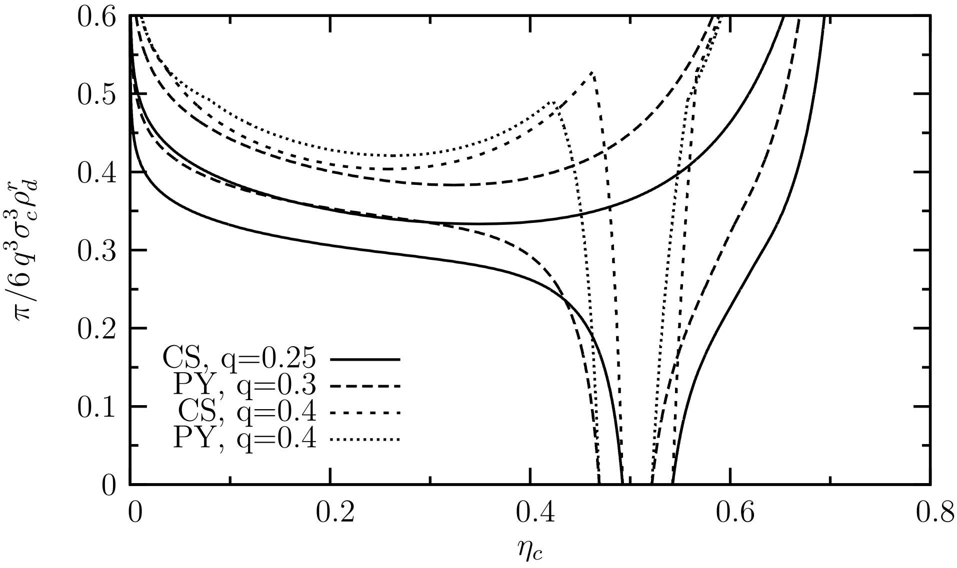

Figure 3.1: Phase diagram of a mixture of colloids and spherical depletion agent with size ratio $q = \sigma_d/\sigma_c$ of the spherical particles in the AOV approach based on the free-volume theory. For both the Percus-Yevick and Carnahan-Starling equation of state the fluid–fluid coexistence is stable for the more symmetric value of $q$. For highly asymmetric values of $q$ only the fluid–solid coexistence is stable. Note that coexisting points are connected by horizontal tie lines. Within the semi-grand canonical treatment $\eta_d^r = (\pi/6)q^3\sigma_c^3\rho_d^r$ denotes the packing fraction of the depletion agent in the reservoir.

treat general mixtures of $\nu_c$ colloid and $\nu_d$ depletion agent components, we are going to restrict our studies to the simpler case of one single colloid species with packing fraction $\eta_c$. For the depletion agent we start by considering a discrete number of $\nu_d$ components. Within the semi-grand canonical ensemble the free-energy density, analogous to Eq. (2.51), is given by

$$\Phi(\eta_c, \{\rho_{d,i}^r\}; \{q_i\}) = \Phi(\eta_c) - \sum_{i=1}^{\nu_d} \rho_{d,i}^r \alpha(\eta_c; \{q_i\}), \tag{3.1}$$

and the set $\{g_\nu^{(i)}\}$ of geometrical measures as introduced in Sec. 2.4 is characterized by the set of parameters $\{q_i\}$. To obtain some insight into the influence of polydispersity in the depletion agent on the phase behavior it might be sufficient to consider a discrete mixture, however we prefer to introduce continuous distributions, which can represent experimental systems more accurately than a discrete distribution. In the following we restrict the set $\{g_\nu^{(i)}\}$ to depend on a single parameter $q$ only. We introduce $d(q)$ as a continuous distribution of the depletion agent in the reservoir, and require that $\int d(q)\mathrm{d}q = 1$. The density distribution of the depletion agent in reservoir follows directly from $\rho_d^r(q)\mathrm{d}q = \rho_d^r\, d(q)\mathrm{d}q$. By specifying the fundamental geometrical

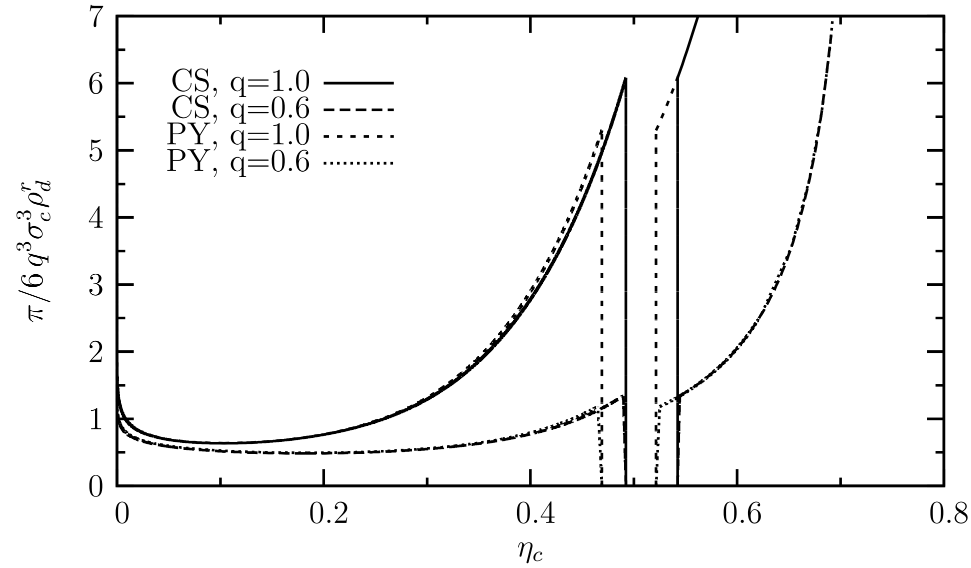

Figure 3.2: Phase diagrams of a mixture of colloids and spherical depletion agent within the AOV model. For symmetric length scales of the colloids and the depletion agent the fluid–fluid coexistence is stable. We find little difference between the approach based on the Rosenfeld and the White Bear version of the functional within FMT, or equivalently between results based on the PY and the CS equation of state except for the fluid–solid coexistence.

measures of the depletion agent as function of $q$ we obtain, similar to Ref. [99],

$$\Phi^{pd}(\eta_c, \rho_d^r; [d]) = \Phi(\eta_c) - \rho_d^r \int \mathrm{d}q\, d(q)\, \alpha(\eta_c, v_d(q), a_d(q), c_d(q), X_d(q)), \qquad (3.2)$$

which is a functional of the distribution $d(q)$. Note that the precise meaning of $q$ is unspecified so far and can refer to a size ratio, in the case of spherical mixtures, or to a parameter that specifies the shape of the depletion agent in a more complicated manner. We return to this point later. Analogous to Eq. (2.43) we call the integral on the r.h.s. of Eq. (3.2) the *effective* free-volume fraction $\alpha_{\text{eff}}$ and we obtain

$$\Phi^{pd}(\eta_c, \rho_d^r; [d]) = \Phi(\eta_c) - \rho_d^r\, \alpha_{\text{eff}}(\eta_c; [d]). \qquad (3.3)$$

## 3.2 Distribution functions

To study the phase behavior of a mixture of spherical colloids and a polydisperse depletion agent we focus on frequently used distributions, namely the Schulz ($S$), the (cut) Gaussian ($G$), the Hat-type ($H$) and the Log-normal ($L$) distribution. These are characterized by two parameters corresponding to their first and second moment.

The average asymmetry ratio is given by $\bar{q} = \tilde{\sigma}_d/\sigma_c$, with the colloid diameter $\sigma_c$ and a length-scale of the depletion agent $\tilde{\sigma}_d$. The parameter $z$ describes the degree of polydispersity: the limiting case, $z \to \infty$, equals the monodisperse fluid and by decreasing the value of $z$ the distribution is broadened. A component is a species of the mixture for which the amount or concentration can be varied independently, e.g., a monodisperse species described by the Dirac-$\delta$ function or a contribution in a bimodal distribution of a polydisperse depletion agent. The distributions under consideration here lead to explicit expressions for the effective free-volume fraction $\alpha_{\text{eff}}(\eta_c; d(q; \bar{q}, z))$, if the geometry of the depletion agent is simple. For more complicated shapes the integration has to be performed numerically. In terms of $\bar{q}$ and $z$, the distributions considered here are given by

$$\begin{aligned}
d_S(q; \bar{q}, z) &= \left(\frac{z}{\bar{q}}\right)^z q^{z-1} \frac{\exp(-zq/\bar{q})}{\Gamma(z)}, \qquad z \geq 1, && (3.4)\\
d_G(q; \bar{q}, z) &= \frac{z}{\sqrt{\pi}} \exp(-(q-\bar{q})^2 z^2)\, 2\,\Theta(q)/[\mathrm{erf}(z\bar{q}) + 1], && (3.5)\\
d_H(q; \bar{q}, z) &= \frac{z}{2} \Theta\left(q - \bar{q} + z^{-1}\right) \Theta\left(-q + \bar{q} + z^{-1}\right), \qquad \bar{q}z > 1, && (3.6)\\
d_L(q; \bar{q}, z) &= \frac{z}{\sqrt{\pi} q} \exp(-(\ln q - \mu(\bar{q}))^2 z^2). && (3.7)
\end{aligned}$$

It is evident that $q > 0$ is required in all distributions and the integration in $\alpha_{\text{eff}}(\eta_c; d(q; \bar{q}, z))$ is performed in the limits from 0 to $\infty$. In the case of a Gaussian distribution one can obtain simpler explicit expressions by imposing the full integration range $q \in (-\infty, \infty)$. The result $d'_G$ is similar to that of the cut Gaussian distribution $d_G$

$$d'_G(q; \bar{q}, z) = \frac{z}{\sqrt{\pi}} \exp(-(q - \bar{q})^2 z^2). \tag{3.8}$$

The Log-normal distribution, for which $\bar{q} = e^{\mu + \sigma^2/2}$ and $\sigma = \bar{q}/\sqrt{z}$, decays slower for large values of $q$ than other distributions considered here.

## 3.3 Effective free-volume fraction

### 3.3.1 Explicit expressions for rod- and disk-like particles

The equations for the chemical potential $\mu_c$ and the osmotic pressure $p$ from Eqs. (2.44) and (2.45) for polydisperse size distributions contain integrals over the distribution. For the calculation of the phase diagram these equations must be solved simultaneously. In general, this must be done numerically. In the case of one- and two-dimensional depletion agents, such as infinitely thin rods or platelets, their geometry is sufficiently simple so that the effective free-volume fraction $\alpha_{\text{eff}}$ can be

| Dim | Depletion agent | Geometry | $v_d$ | $a_d$ | $c_d$ | $X_d$ |
|---|---|---|---|---|---|---|
| 1 | prolate ellipsoid | $c = q\,\sigma_c/2,\ b \to 0, a \to 0$ | 0 | 0 | $\frac{c}{2}$ | 1 |
| 1 | spherocylinder | $L = q\,\sigma_c,\ R \to 0$ | 0 | 0 | $\frac{L}{4}$ | 1 |
| 2 | oblate ellipsoid | $a = b = q\,\sigma_c/2,\ c \to 0$ | 0 | $2\pi a^2$ | $\frac{\pi}{4}a$ | 1 |
| 2 | cylinder, spherodisk, cut sphere | $R = q\,\sigma_c/2,\ L \to 0$ | 0 | $2\pi R^2$ | $\frac{\pi}{4}R$ | 1 |
| 2 | hexagonal platelet | $R = q\,\sigma_c/2,\ L \to 0$ | 0 | $3\sqrt{3}R^2$ | $\frac{3}{4}R$ | 1 |

Table 3.1: Geometrical measures for one- and two-dimensional depletion agents. All lengths are measured in units of the diameter $\sigma_c = 2R_c$ of the spherical colloids. For ellipsoids $a$, $b$ and $c$ denote the half-axes, in the other cases $R$ is the radius, $L$ the thickness or length of the depletion agent, respectively. The asymmetry ratio $q$ plays the role of the size ratio with respect to the colloid size in this limiting case.

calculated explicitly. Infinitely thin needles, which represent one-dimensional depletion agents, can be obtained as limiting case from, e.g., prolate ellipsoids or spherocylinders. Infinitely thin platelets, which represent two-dimensional depletion agents, can be obtained as limiting case from, e.g., oblate ellipsoids, cylinders, spherodisks, cut spheres or hexagonal platelets. The geometric measures for these geometries are given in Tab. 3.1. In the following we show explicit expressions for $\alpha_{\text{eff}}$ for one- and two-dimensional depletion agents based on some of the distributions given above. As aforementioned, we obtain the thermodynamic quantities of the pure hard-sphere fluid that enter the free-volume fraction $\alpha_{\text{eff}}$ from the excess free energy density $\Phi$ of the White Bear version of FMT [67, 81]. These quantities are the pressure $\beta p = \partial\Phi/\partial n_3$, the surface tension $\beta\sigma = \partial\Phi/\partial n_2$ and bending rigidities $\beta\kappa = \partial\Phi/\partial n_1$ and $\beta\bar{\kappa} = \partial\Phi/\partial n_0$.

The explicit expressions for the effective free-volume fraction in the case of infinitely thin needles for the Schulz, the Gaussian, and the Hat-type distribution, Eqs. (3.4)-(3.6), read

$$\alpha_{\text{eff},S}(\eta_c;\bar{q},z) = \frac{2^z z^z}{(\bar{q}\kappa\,\sigma_c/2 + 2\,z)^z\, e^{\bar{\kappa}}}, \tag{3.9}$$

$$\begin{aligned}\alpha_{\text{eff},G}(\eta_c;\bar{q},z) &= \exp\left(-\bar{\kappa} - \bar{q}\kappa\sigma_c/4 + \frac{\kappa^2\sigma_c^2}{64z^2}\right)\\ &\quad\times\frac{1}{\operatorname{erf}(z\bar{q})+1}\left(1 - \operatorname{erf}\left(\frac{-z^2\bar{q} + \kappa\,\sigma_c/8}{z}\right)\right),\end{aligned} \tag{3.10}$$

$$\alpha'_{\text{eff},G}(\eta_c;\bar{q},z) = \exp\left(-\bar{\kappa} - \bar{q}\kappa\sigma_c/4 + \frac{\kappa^2\sigma_c^2}{64z^2}\right), \tag{3.11}$$

$$\alpha_{\text{eff},H}(\eta_c;\bar{q},z) = \frac{4z}{\kappa\sigma_c}\exp\left(-\bar{\kappa} - \bar{q}\kappa\sigma_c/4\right)\sinh\left(\frac{\kappa\,\sigma_c}{4z}\right). \tag{3.12}$$

Since only $\kappa$ and $\bar{\kappa}$ enter these expressions for one-dimensional depletion agents, there is no difference between an approach based on the PY or the BMCSL equation of state. In terms of the colloid packing fraction $\eta_c$, the average asymmetry ratio $\bar{q}$ and the polydispersity parameter $z$ we obtain

$$\alpha_{\text{eff},S}(\eta_c;\bar{q},z) = (2z)^z\,(1-\eta_c)\left(3\,\frac{\bar{q}\eta_c}{1-\eta_c}+2\,z\right)^{-z}, \tag{3.13}$$

$$\begin{aligned}\alpha_{\text{eff},G}(\eta_c;\bar{q},z) &= (1-\eta_c)\exp\left(-\frac{3\bar{q}\eta_c}{2(1-\eta_c)}+\frac{9{\eta_c}^2}{16z^2\,(1-\eta_c)^2}\right)\\ &\quad\times\frac{1}{\operatorname{erf}(z\bar{q})+1}\left(1-\operatorname{erf}\left(-z\bar{q}+\frac{3\eta_c}{4z(1-\eta_c)}\right)\right), \end{aligned}\tag{3.14}$$

$$\alpha'_{\text{eff},G}(\eta_c;\bar{q},z) = (1-\eta_c)\exp\left(-\frac{3\bar{q}\eta_c}{2(1-\eta_c)}+\frac{9{\eta_c}^2}{16z^2\,(1-\eta_c)^2}\right), \tag{3.15}$$

$$\alpha_{\text{eff},H}(\eta_c;\bar{q},z) = \frac{2z(1-\eta_c)^2}{3\eta_c}\exp\left(\frac{-3\bar{q}\eta_c}{2(1-\eta_c)}\right)\sinh\left(\frac{3\eta_c}{2z\,(1-\eta_c)}\right). \tag{3.16}$$

The effective free-volume fraction is unity for vanishing colloid packing fraction, $\eta_c \to 0$. In this case the complete volume $V$ is accessible to the particles of the depletion agent. $\alpha_{\text{eff}}$ decreases upon increasing $\eta_c$ since a part of the system volume is occupied by colloids. An example for $\alpha_{\text{eff}}$ for a one-dimensional depletion agent with $\bar{q} = 1.0$ and three different values of the parameters $z$ of the Schulz distribution is plotted in Fig. 3.3. We show results for $z = 2, 10$ and $\infty$, which corresponds to the monodisperse case. The influence of polydispersity on the effective free-volume fraction is small for low values of $\eta_c$ and is larger for higher values of $\eta_c$ (see Fig. 3.3). However, for the distributions introduced above and for the parameters used here, the differences between the various results remain small. For more asymmetric values of the size ratio $q = \bar{L}/\sigma_c$ or broader size distributions the difference between results increases.

In the present study we restrict the product $\bar{q}z$ to sufficiently large values. For the Hat-type distribution we require $\bar{q}z > 1$ which ensures $\int_0^\infty \mathrm{d}q\, d(q) = 1$. In the case of the Gaussian distribution $d'_G$ we require $\bar{q}z > 1$ since for small values of $\bar{q}z$ the contribution of the distribution from values $q < 0$ increases, e.g., for $\bar{q} = 0.5$ and $z = 3$ we obtain $\int_{-\infty}^0 \mathrm{d}q\, d_G(q) \lesssim 10^{-2}$.

In the case of two-dimensional depletion agents, which we can obtain from the limiting case of vanishing thickness of various objects (see Tab. 3.1), the geometric measures can differ for different geometry of the depletion agent: for circular and hexagonal platelets $a_d$ and $c_d$ differ, while those of cut sphere and cylinder equal. For that reason results for $\alpha_{\text{eff}}$ are shown in a general form. The effective free-volume fractions within the BMCSL approach are given by

$$\alpha_{\text{eff},S}(\eta_c;\bar{q},z) = \left(\frac{z}{\bar{q}}\right)^z(-2\chi_2)^{-z/2}\exp\left(-\frac{\chi_1^2}{8\chi_2}+\chi_0\right)D_{-z}\left(\frac{-\chi_1}{\sqrt{-2\chi_2}}\right), \tag{3.17}$$

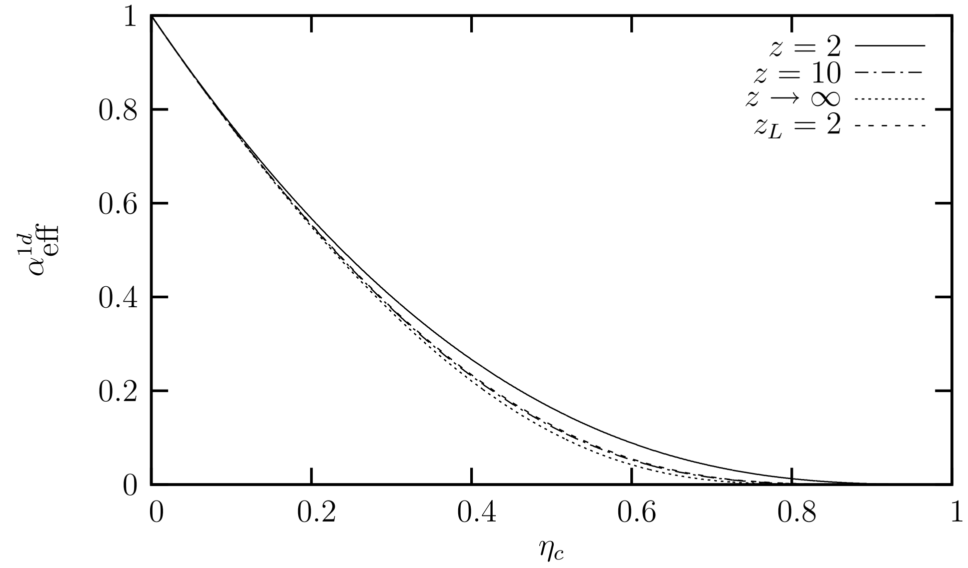

Figure 3.3: The effective free-volume fraction $\alpha_{\text{eff}}(\eta_c; d(q; \bar{q}, z))$ in the case of infinitely thin polydisperse rod-shaped depletion agents for the Schulz and the Log-normal distribution. The average size asymmetry ratio $\bar{q} = \bar{L}/\sigma_c = 1.0$. $z$, the parameter describing the degree of size polydispersity, is 2, 10 and $\infty$, whereby the latter corresponds to the monodisperse limit. Results corresponding to different values of $z$ deviate from each other at intermediate and high values of the colloid packing fraction $\eta_c$. The curves for the Log-normal distribution ($z_L = 2$) and the Schulz distribution with $z = 10$ almost collapse. The Gaussian and Hat-type distributions yield very similar behavior (not shown in this figure). Note that hard spheres in three dimensions reach close-packing at $\eta_c = \eta_{cp} = \pi\sqrt{2}/6 \approx 0.74$. For reasons of simplicity we plot $\alpha_{\text{eff}}(\eta_c)$ in the whole range of $0 \leq \eta_c \leq 1$.

$$\begin{aligned}
\alpha_{\text{eff},G}(\eta_c; \bar{q}, z) &= \exp\left(\frac{z^2\bar{q}^2\chi_2 + \chi_0\, z^2 - \chi_0\, \chi_2 + z^2\bar{q}\chi_1 + {\chi_1}^2/4}{z^2 - \chi_2}\right) \\
&\quad \times \left(\text{erf}\left(\frac{z^2\bar{q} + \chi_1/2}{\sqrt{z^2 - \chi_2}}\right) + 1\right) \frac{z}{2[\text{erf}(z\bar{q}) + 1]\sqrt{z^2 - \chi_2}}, \qquad (3.18) \\
\alpha'_{\text{eff},G}(\eta_c; \bar{q}, z) &= \exp\left(\frac{z^2\bar{q}^2\chi_2 + \chi_0 z^2 - \chi_0\chi_2 + z^2\bar{q}\chi_1 + {\chi_1}^2/4}{z^2 - \chi_2}\right) \frac{z}{\sqrt{z^2 - \chi_2}}, \qquad (3.19) \\
\alpha_{\text{eff},H}(\eta_c; \bar{q}, z) &= \frac{z}{4}\sqrt{\frac{\pi}{-\chi_2}} \exp\left(\chi_0 - \frac{\chi_1^2}{4\chi_2}\right) \\
&\quad \times \sum_{n=1}^{2} (-1)^n \text{erf}\left(\frac{2\chi_2(\bar{q} - (-1)^n) + \chi_1 z}{2z\sqrt{-\chi_2}}\right), \qquad (3.20)
\end{aligned}$$

where $\chi_2 = -\beta\gamma a_d/q^2$, $\chi_1 = -\beta\kappa c_d/q$ and $\chi_0 = -\beta\bar{\kappa}X_d$. The geometrical measures $a_d$, $c_d$ and $X_d$ are given in Tab. 3.1. $D_{-z}(x)$ with $z > 0$ denote the parabolic cylinder functions.

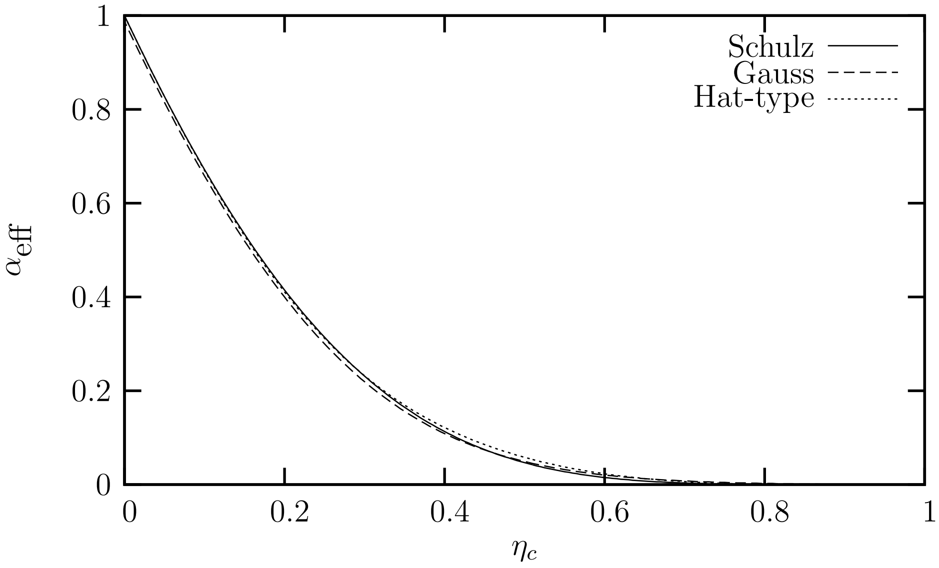

Figure 3.4: The effective free-volume fraction $\alpha_{\text{eff}}$ for polydisperse spherical depletion agent and different underlying distributions. The first and the second moment are equal in all cases. Although we observe slightly different behavior between the various distributions in the intermediate range of the colloid packing fraction $\eta_c$, and in particular for low $\eta_c$ for the Gaussian distribution (see text), the different distributions yield very similar results.

### 3.3.2 Results for spherical depletion agent

In the case of a three-dimensional depletion agent, e.g., spherical particles which model polymer coils, the integration in Eq. (3.2) in the considered cases cannot be performed analytically. For a spherical depletion agent we show results to demonstrate the dependence on the different types of distribution, the influence of the broadness of the distribution and the influence of the size asymmetry between the colloids and the depletion agent. Figure 3.4 shows the effective free-volume fraction $\alpha_{\text{eff}}$ based on the Schulz, the Gaussian and the Hat-type distribution. In all cases $\bar{q} = 0.5$ and we consider equal second moments, i.e., $z_S = 5.000$, $z_G = 3.157$ and $z_H = 2.582$ for the different distributions. For increasing values of $\eta_c$ we find a stronger decrease of $\alpha_{\text{eff}}$ in case of the three-dimensional particles as compared to rod-like (one-dimensional) particles. The spheres can fill the space better. Note that for pure hard spheres the fluid phase is stable up to $\eta_c \approx 0.49$ and for $\eta_c \gtrsim 0.54$ the hard spheres are in the crystalline phase. In the case shown in Fig. 3.4 no cut-off is applied to the Gaussian ($G$) distribution which is the reason for the deviations at low $\eta_c$. We observe an overall similarity for the different distributions.

In the following we focus on the Schulz distribution as this is widely studied in theory and describes real systems better: it avoids unphysical properties that appear

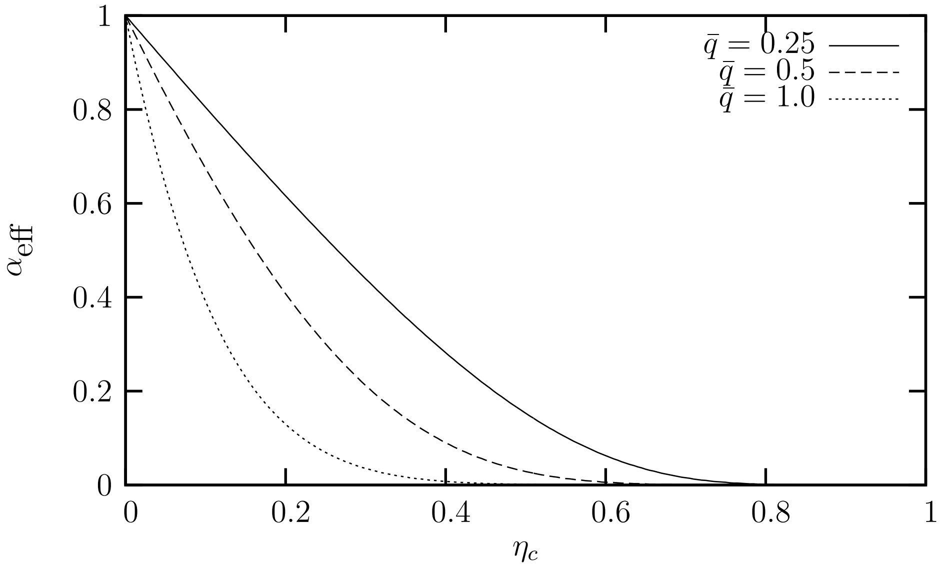

Figure 3.5: For fixed polydispersity, $z = 10$, we compare the effective free-volume fraction $\alpha_{\text{eff}}$ for various values for the degree of asymmetry between the colloid and the depletion agent. In the asymmetric case, $\bar{q} = 0.25$, the curve is nearly linear for low $\eta_c$ and exhibits low slope. For more symmetric cases the accessible volume to the larger depletion agent decreases stronger and we find steeper curves with strong decrease to low values of the free volume.

in the Hat-type distribution or due to the cut-off in the Gaussian distribution. Unless expressed explicitly the parameters $z$ and $\bar{q}$ refer to the Schulz distribution in the following.

For fixed polydispersity, $z = 10$, and three different values of size asymmetry, $\bar{q} = 0.25, 0.5$ and $1.0$, we show the effective free-volume fraction $\alpha_{\text{eff}}$ in Fig. 3.5. In the highly asymmetric case the curve is flatter than in the more symmetric cases, and in a wider range the former exhibits nearly linear decrease. The free volume decreases steeper for more symmetric depletion agent.

When we study systems with fixed average size, $\bar{q} = 0.25$, and varying polydispersity described by the parameter $z$ we observe little difference. However, in the following sections we demonstrate that this difference has a significant influence on the phase diagram. Figure 3.6 displays that for low degree of polydispersity ($z = 50$) in the range of low $\eta_c$ we observe almost linear behavior. Upon increasing polydispersity, i.e., for lower values of $z$, the curve has a more negative slope for small $\eta_c$ but the effective free-volume fraction $\alpha_{\text{eff}}$ exhibits larger values at intermediate colloid packing fractions $\eta_c$. The results refer to the CS equation of state. For $z = 10$ and $\bar{q} = 0.25$ we compare the results based on the CS and the PY equation of state.

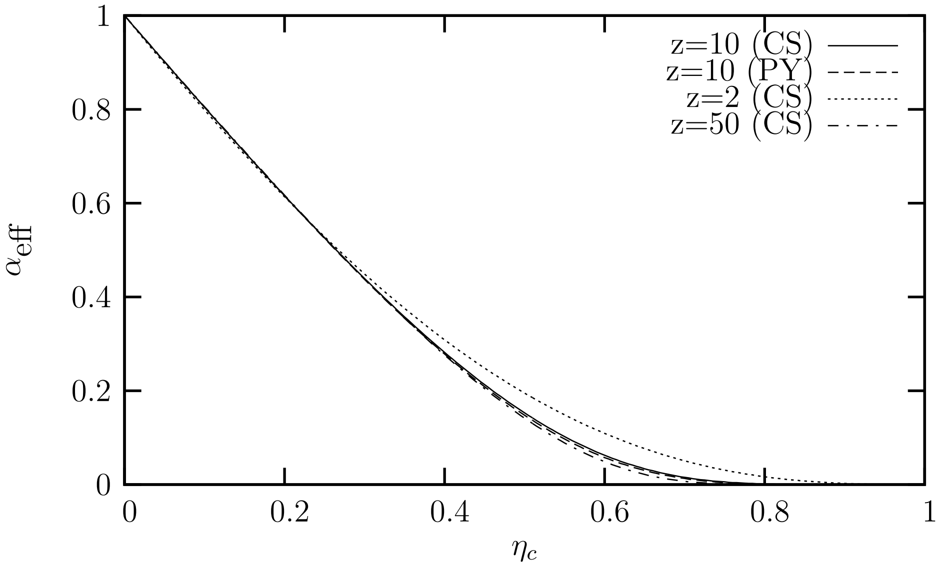

Figure 3.6: For fixed average size of the depletion agent, $\bar{q} = 0.25$, we show the influence of polydispersity on the behavior of the effective free-volume fraction $\alpha_{\text{eff}}$. For low degree of polydispersity ($z = 50$) we observe almost linear behavior at low values of $\eta_c$. Upon increasing polydispersity, i.e., decreasing the value of $z$, for low $\eta_c$ the curve exhibits a more negative slope and a larger deviation from the linear behavior. The values of $\alpha_{\text{eff}}$ are larger at intermediate range of $\eta_c$ as compared to the case of a narrow distribution (dash-dotted line). In one case, $z = 10$, we show the comparison between results based on the PY (dashed line) and the CS (full line) equation of state.

## 3.4 Phase diagrams

### 3.4.1 Influence of size polydispersity

In this section we study the phase diagrams of a mixture of (monodisperse) colloids and polydisperse spherical ideal polymer [9–11] as depletion agent. As we showed in the previous section the effective free-volume fraction $\alpha_{\text{eff}}$ cannot be obtained explicitly in contrast to some cases of one- and two-dimensional depletion agents. Once we have the effective free-volume fraction, we evaluate the phase diagram by solving Eqs. (2.44) and (2.45) simultaneously which, in any case, must be performed numerically. We describe the polymer polydispersity by means of the Schulz distribution, cf. Eq. (3.4). The Schulz distribution is frequently used in theoretical studies of polydispersity. It is described by the mean value $\bar{q}$ and the standard deviation $\sigma = \bar{q}/\sqrt{z}$.

The equations of state of the pure reference system and the free-volume fraction $\alpha$ respectively, and hence the chemical potential $\mu_c$ and the osmotic pressure $p$ of the colloids, are based on the free energy density $\Phi$ of the White Bear version of FMT, cf. Eq. (2.53).

In the case of a spherical ideal polymer as monodisperse depletion agent, the free-volume fraction is given explicitly by [51]

$$\alpha_{CS} = (1-\eta_c)\exp\left(-\frac{\eta_c\,(1+\eta_c+\eta_c^2-\eta_c^3)}{(1-\eta_c)^3}q^3 - \left(3\ln(1-\eta_c) + \frac{6\eta_c-3\eta_c^2}{(1-\eta_c)^2}\right)q^2 - \frac{3\eta_c}{1-\eta_c}q\right). \tag{3.21}$$

In Fig. 3.7(a) we show phase diagrams of polydisperse AOV mixtures obtained within our approach. We vary the polydispersity and keep the size ratio $\bar{q} = \langle\sigma_d\rangle/\sigma_c = 0.25$ fixed, where $\sigma_d$ is the diameter of the spherical depletion agent. For this size ratio, the fluid–fluid phase separation in the monodisperse case is metastable w.r.t. the fluid–solid coexistence [38]. We display phase diagrams for $z = 50, 10$ and 2. The corresponding polymer size distributions in the reservoir are plotted in Fig. 3.7(b). For $z = 50$ the phase diagram is very similar to that of a mixture of colloids with monodisperse polymer and the fluid–fluid coexistence remains metastable (full lines). Upon decreasing $z$, which broadens the size distribution, the fluid–fluid and the fluid–solid coexistence lines approach each other and almost touch each other for $z = 10$ (dashed lines). By further increasing the degree of polydispersity the fluid–fluid coexistence becomes stable, as we display in Fig. 3.7(a) for $z = 2$ (dotted lines). The critical point is shifted to lower colloid packing fractions $\eta_c$ as the value of $z$ decreases. We like to highlight that the small difference in the effective free-volume fractions (see Fig. 3.6) result in a considerable shift of the coexistence lines and the appearance of a stable critical point.

We have compared these results to the treatment of the phase behavior completely based on the PY compressibility equation of state and find qualitatively similar results. In the present approach this is achieved by employing the free energy density $\Phi$ of Rosenfeld's original formulation of FMT to evaluate $\alpha_{\text{eff}}$ and the pressure and chemical potential of a pure reference system. Figure 3.8 shows the corresponding result for $\bar{q} = 0.3$ and three values for the degree of polydispersity, $z = 50, 10$ and 2. For low degree of polydispersity ($z = 50$) the fluid–fluid coexistence is situated in the metastable regime (full lines) as expected from the description of the results based on the CS equation of state. Again, for highly polydisperse depletion agent, $z = 2$, the fluid–fluid coexistence is stabilized (dotted lines). This is already the case for the intermediate value, however, slightly different value of $\bar{q}$ is chosen here which is the reason for the difference to the results above. For $\bar{q} = 0.3$ we find that the fluid–fluid coexistence regime is already stable at $z = 10$.

The polymer distribution in the system differs from that in the reservoir [42], which is a phenomenon known as *fractionation.* For spherical polymer we find results

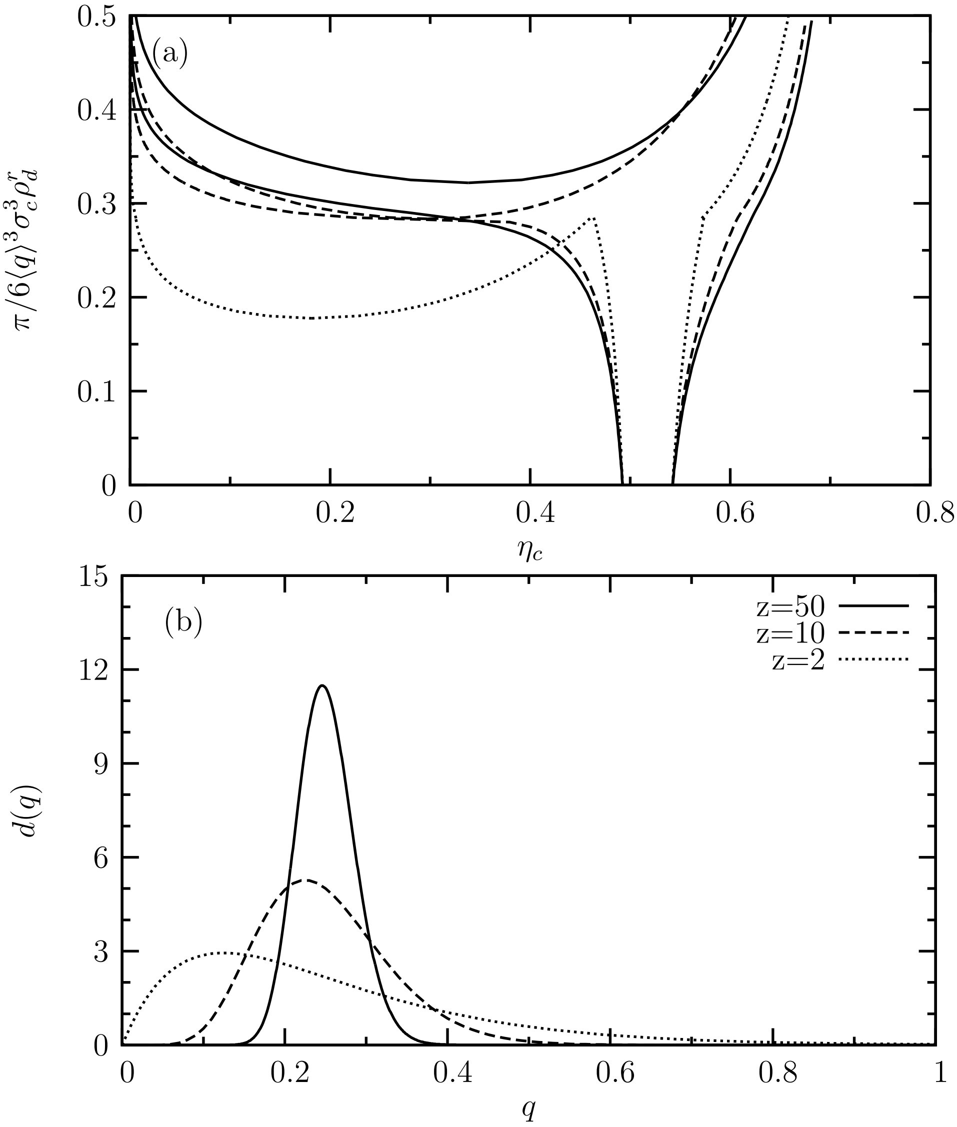

Figure 3.7: (a) Phase diagrams of mixtures of colloids and a polydisperse spherical depletion agent with an average size ratio $\bar{q} = 0.25$ and (b) the corresponding distributions. We employ a free-volume theory based on the BMCSL equation of state. For low degrees of polydispersity, corresponding to $z = 50$ (full lines), the fluid–fluid phase separation is metastable w.r.t. fluid–solid coexistence. Upon increasing the degree of polydispersity, corresponding to $z = 10$ (dashed lines) and $z = 2$ (dotted lines), the fluid–fluid coexistence is stabilized.

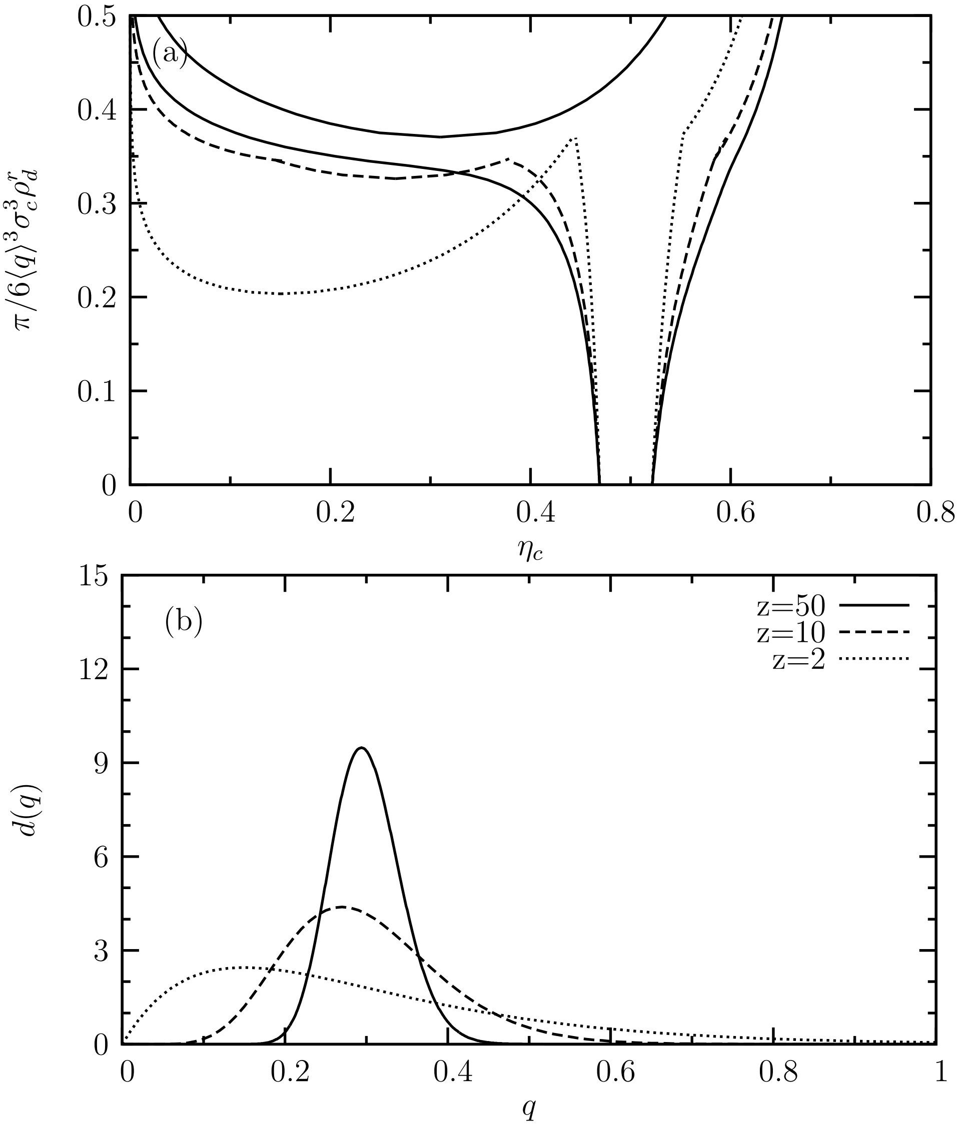

Figure 3.8: (a) Phase diagrams of mixtures of colloids and a polydisperse spherical depletion agent with an average size ratio $\bar{q} = 0.3$ and (b) the corresponding distributions. In this case we employed the mixture PY equation of state. For large values of $z = 50$ (full lines), i.e., for low degree of polydispersity, the fluid–fluid coexistence is metastable. Upon increasing polydispersity to $z = 10$ (dashed lines) and further to $z = 2$ (dotted lines) the fluid–fluid coexistence is stabilized.

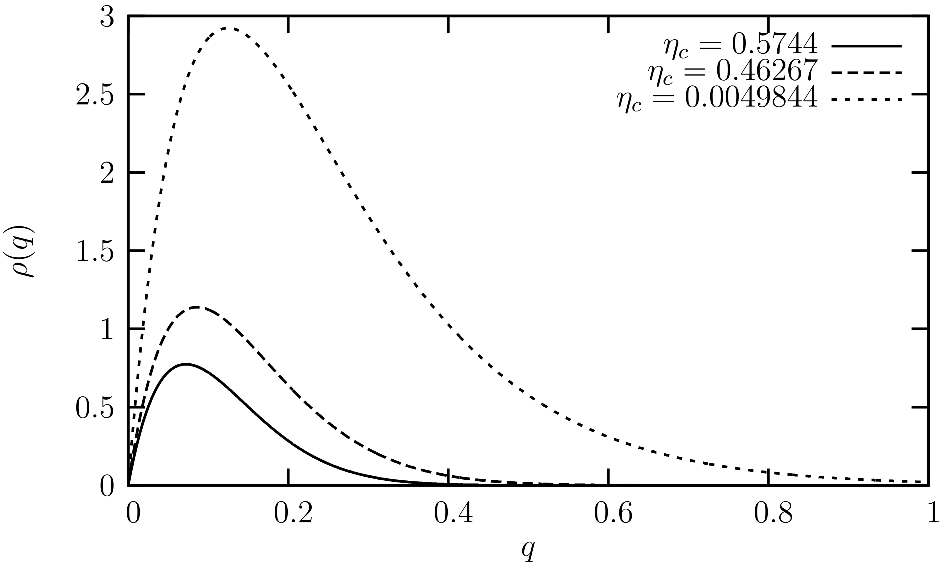

Figure 3.9: Density distributions $\rho(q)$ for spherical depletion agent with $\bar{q} = 0.25$ and a high degree of polydispersity, $z = 2$. The three curves correspond to the three different values of $\eta_c$ at the triple point obtained from the approach based on the BMCSL equation of state. For increasing colloid packing fraction the maximum of the density distributions is shifted to lower values of $q$.

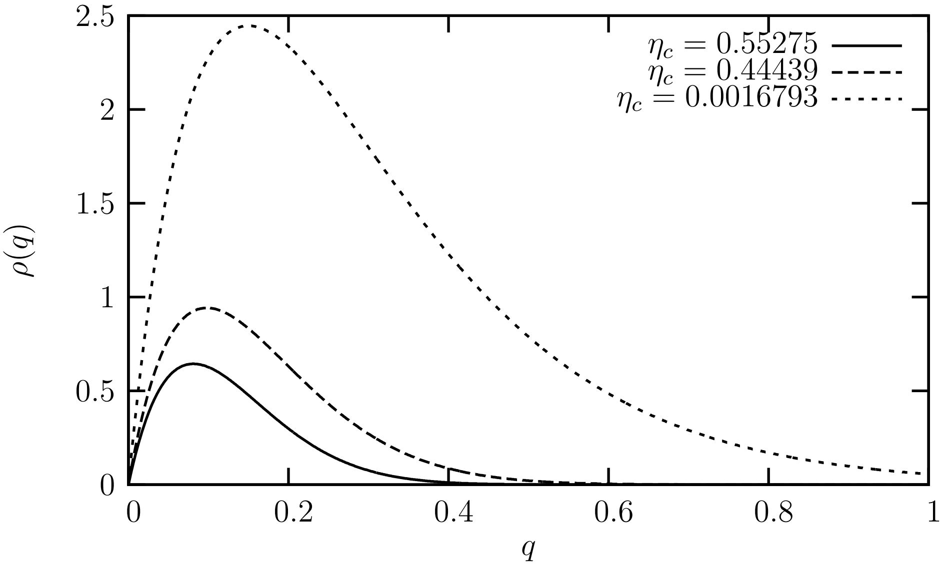

Figure 3.10: Density distributions $\rho(q)$ for spherical depletion agent with $\bar{q} = 0.3$ and a very high degree of polydispersity, $z = 2$. In this case the PY equation of state is employed. The three curves correspond to the three different values of $\eta_c$ at the triple point, and in a similar fashion to the BMCSL results (see Fig. 3.9) for increasing colloid packing fraction the maximum of the density distributions is shifted to lower values of $q$.

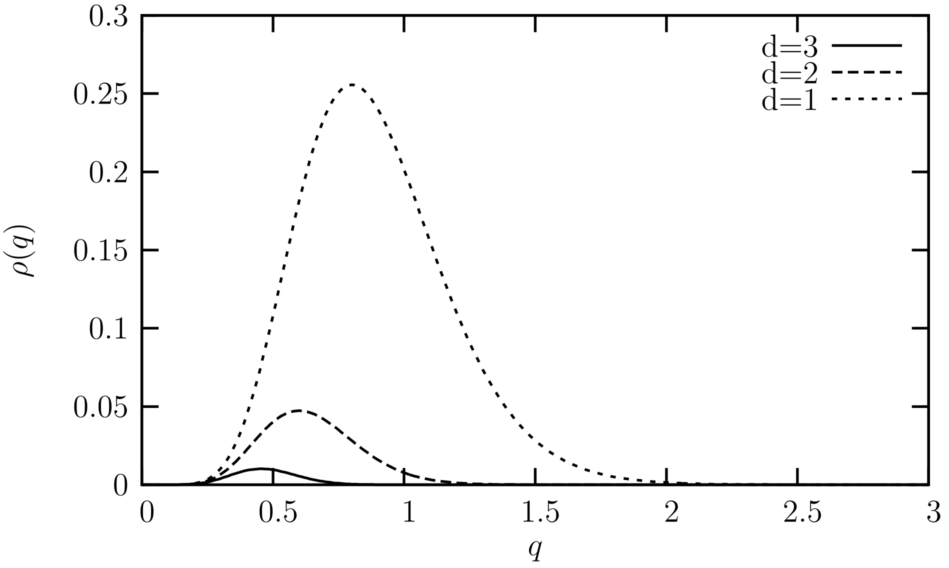

Figure 3.11: Density distributions for different type of the depletion agent. In all cases we employ the Schulz distribution with $z = 10$ and $\bar{q} = 1.0$. The colloid packing fractions $\eta_c$ are approximate values of the triple point. We show curves for the phase with intermediate density, i.e., the liquid phase and $\eta_c^{a.t.p.} = 0.45$. For three-dimensional particles (spheres) we observe the strongest shift of the curve. Two-dimensional particles (platelet-like thin disks) and one-dimensional particles (needle-like thin rods) exhibit smaller shift.

equivalent to those from Ref. [42]. At low packing fractions of the colloids the size distribution of (spherical) polymer follows closely the reservoir distribution. As the colloid packing fraction increases, the maximum height of the polymer size distribution decreases significantly and shifts towards smaller polymer radii. In Figs. 3.9 and 3.10 we show results for the density distribution $\rho(q) = d(q)\,\alpha(q;\eta_c = \eta_c^{t.p.})$ for the examples given above, i.e., $z = 2$ and $\bar{q} = 0.25$ for the CS and $z = 2$ and $\bar{q} = 0.3$ for the PY equation of state. The three different curves correspond to the three different values of the colloid packing fraction $\eta_c^{t.p.}$ at the triple point.

In principle we observe a qualitatively similar but less pronounced behavior also in the case of platelet-like or rod-like depletion agents. The maximum of the size distribution of the depletion agent becomes smaller and moves to smaller sizes as the colloid packing fraction in the system increases. In Fig. 3.11 we present results for the density distribution for one-, two- and three-dimensional depletion agents, i.e., spheres, thin disks and thin rods. The degree of polydispersity is equal, $z = 10$, in all cases and $\bar{q} = 1.0$. The colloid packing fraction is taken at the intermediate of the approximate values for the triple point, $\eta_c^{a.t.p.} = 0.45$. The shift observed in Fig. 3.11 was expected, because one- or two-dimensional depletion agents require less

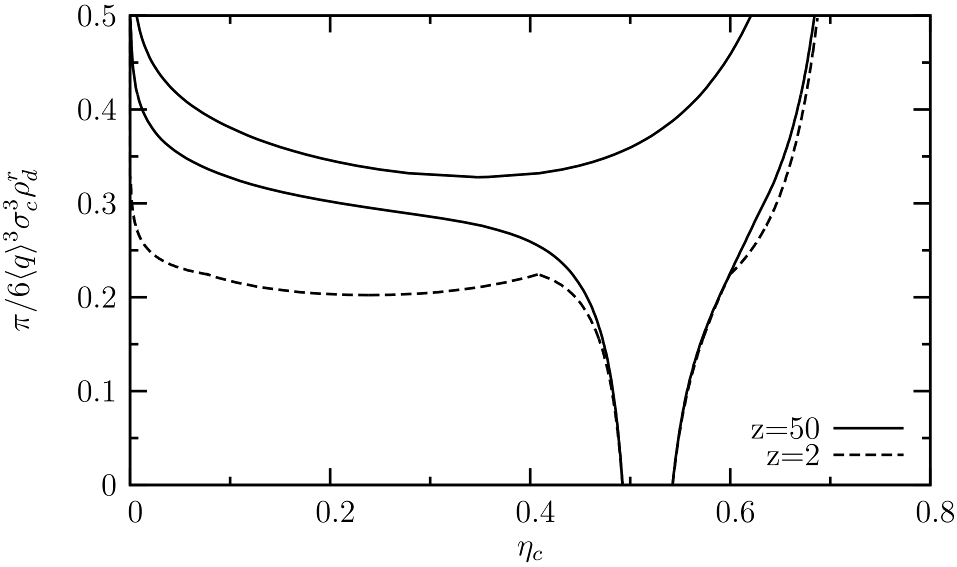

Figure 3.12: Phase diagrams for polydisperse depletion agent with varying morphology. The volume $v_d$ is fixed, while the surface area $a_d$ and the integrated mean curvature $c_d$ depend on the parameter $q$, which is distributed with $d(q)$. For low and high values of $q$ the depletion agent becomes ellipsoidal. The average value $\bar{q} = 1.0$ and $\sigma_d = 0.25\sigma_c$. To compare with the spherical depletion agent the BMCSL equation of state is employed. For low degree of polydispersity ($z = 50$) the fluid–fluid coexistence is situated in the metastable regime and is stabilized upon increasing the degree of polydispersity ($z = 2$).

free volume to fit between colloids than spherical polymer.

### 3.4.2 Influence of morphology polydispersity

In the previous sections we have considered size polydispersity in the distribution of the depletion agent. In this section we focus on the influence of a depletion agent with varying particle shapes or, in other terms, on the influence of morphology polydispersity on the phase behavior. To this end we consider ellipsoids, with half-axes $a = b = \sigma_d/(2\sqrt{q})$ and $c = q\sigma_d/2$, for which the geometrical measures can be obtained explicitly [51]. The length scale $\sigma_d$ is fixed and in the following set to $\sigma_d = 0.25\sigma_c$. In this relatively simple case a single parameter $q$ characterizes the shape. Obviously, more complicated scenarios are possible. Note that for this choice of half-axes the volume $v_d = \pi\sigma_d^3/6$ is kept fixed, while the surface area $a_d = \pi\sigma_d^2(1/q + q^{3/2}(\operatorname{arccosh} 1/q^{3/2})/\sqrt{1/q - q^2})/2$ and integrated mean curvature $c_d = \sigma_d(q + (\arccos q^{3/2})/\sqrt{q - q^4})/4$ depend on $q$. The Euler characteristic $X_d = 1$ is independent of $q$. The parameter $q$ describes the degree of deviation of the shape

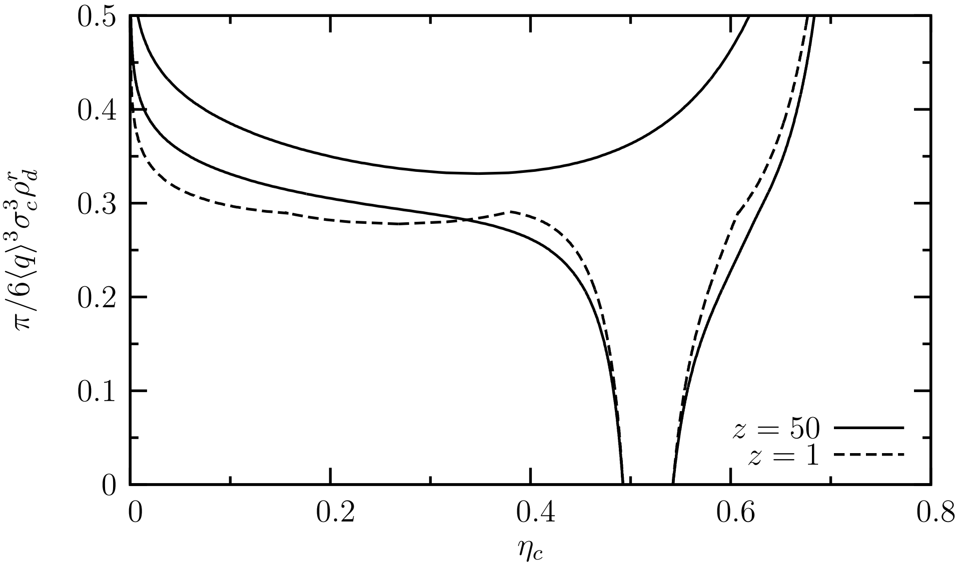

Figure 3.13: Phase diagrams for polydisperse depletion agent with varying morphology. In this case, all fundamental measures (except $X_d$) depend on the parameter $q$. The volume is linear in $q$. The shape of the depletion agent is ellipsoidal and its polydispersity is described by the Schulz distribution with $\bar{q} = 1.0$ while $\sigma_d = 0.25\sigma_c$. The increase of the degree of polydispersity from $z = 50$ to $z = 1$ stabilizes the fluid–fluid coexistence.

from a sphere: for small values of $q$ we obtain lens-shaped depletion agent (oblates), while for large values of $q$ the particles become cigar-shaped (prolates). Similarly to the case of size polydispersity, we observe that an increasing degree of shape polydispersity stabilizes the fluid–fluid phase separation w.r.t. fluid–solid decomposition (see Fig. 3.12). It seems that polydispersity in general favors a stable fluid–fluid phase separation because the polydisperse depletion agent can fill the free volume of the system more effectively than a monodisperse one. Even if the bigger particles of the distribution cannot find free volume in the system, the smaller ones might still do. In terms of the depletion potential this would result in a longer range of the effective attraction between colloids [43], giving rise to a more negative effective second virial coefficient $B_2^{\text{eff}}$ which increases the tendency for fluid–fluid phase separation [100].

This effect seems to be robust against details of introducing polydispersity as we also observe that the fluid–fluid coexistence is stabilized for an ellipsoidal depletion agent with $a = b = \sigma_d/2$ and $c = q\sigma_d/2$, where all geometrical measures, except the Euler characteristics, depend on $q$. In this case $v_d = \pi/6\sigma_c^3 q \propto q$, $a_d = (1 + q^2 \operatorname{arccosh}(1/q)/\sqrt{1-q^2})\,\pi/(2\sigma_c^2)$, $c_d = (q + \arccos(q)/\sqrt{1-q^2})\,\sigma_c/4$ and $X_d = 1$. The phase diagrams are shown in Fig. 3.13.

## 3.5 Ternary mixtures

### 3.5.1 Phase diagrams for bimodal and bidisperse distributions

In experimental systems of colloid and polymer mixtures polydispersity in general can result from imperfection in the synthesis process and practical limitations. If two spherical polymer components with significant different sizes are mixed with colloids one would obtain a ternary mixture. The sizes of the polymer would now be described by a bimodal distribution $d_S(q; x, \bar{q}, \bar{Q}, z_{\bar{q}}, z_{\bar{Q}}) = x\, d_S(q; \bar{q}, z_{\bar{q}}) + (1-x)\, d_S(q; \bar{Q}, z_{\bar{Q}})$ with a mixing parameter $x$ and two averaged size ratios $\bar{q}$ and $\bar{Q}$. For simplicity we assume the width of both parts of the distribution to be equal, $z_{\bar{q}} = z_{\bar{Q}} = 5$. In Figs. 3.14–3.17 we show phase diagrams in the $(\eta_c, \tilde{\eta}_d^r)$–representation for different values of the mixing parameter $x$. We choose $\bar{q} = 0.25$ and $\bar{Q} = 2.0$. The polymer reservoir packing fraction is given by $\tilde{\eta}_d^r = \frac{\pi}{6} \langle q \rangle^3 \sigma_c^3 \rho_d^r$, where $\langle q \rangle = x\, \bar{q} + (1-x)\, \bar{Q}$. For $x = 0.9999$ (see Fig. 3.14) the phase diagram is similar to the polydisperses case studied above [see Fig. 3.7(a) for $z = 2$ and 10]. Upon decreasing $x$, the fraction of the polymer with average size ratio $\bar{Q}$ increases, and the spinodal exhibits two minima, one corresponding to the stable critical point (triangle) and the other corresponding to an additional metastable fluid–fluid phase separation (diamond) — see Fig. 3.15. Further decreasing the value of the mixing parameter to $x = 0.9935$ (Fig. 3.16) leads to a phase diagram with two *stable* critical points and two triple points. At one triple point, a gas, a liquid, and a solid phase coexist, while at the second triple point a gas phase and two liquid phases with different densities coexist. There is a novel low density liquid phase in the region between the two critical points with $\eta_c = 0.0177$ and 0.251. Upon varying the value of $x$ the triple points are shifted. According to Gibbs' phase rule a four-phase coexistence between the gas, the low density liquid, the high density liquid and the solid is also possible. For our system it is expected for $x$ between the values used in Fig. 3.15 and 3.16, i.e., between $x = 0.995$ and 0.9935. In Fig. 3.17 for $x = 0.98$ we also observe two critical points. The critical point with lower colloid packing fraction (diamond) is stable — see Fig. 3.17 for the phase diagram and Fig. 3.18 for the corresponding bimodal distribution $d(q)$. The second critical point at higher colloid packing fraction (triangle) is now situated in the metastable regime and vanishes upon further decreasing the values of $x$. For these systems one liquid phase and one triple point are stable. Further decrease of the values of $x$ approximately below 0.8 lead to a shift of the coexistence region to higher values of $\tilde{\eta}_d^r$. For $x \ll 1$ the fluid–fluid binodal lies in the region of the fluid with monomodal polydisperse depletion agent with $\bar{Q} = 2.0$.

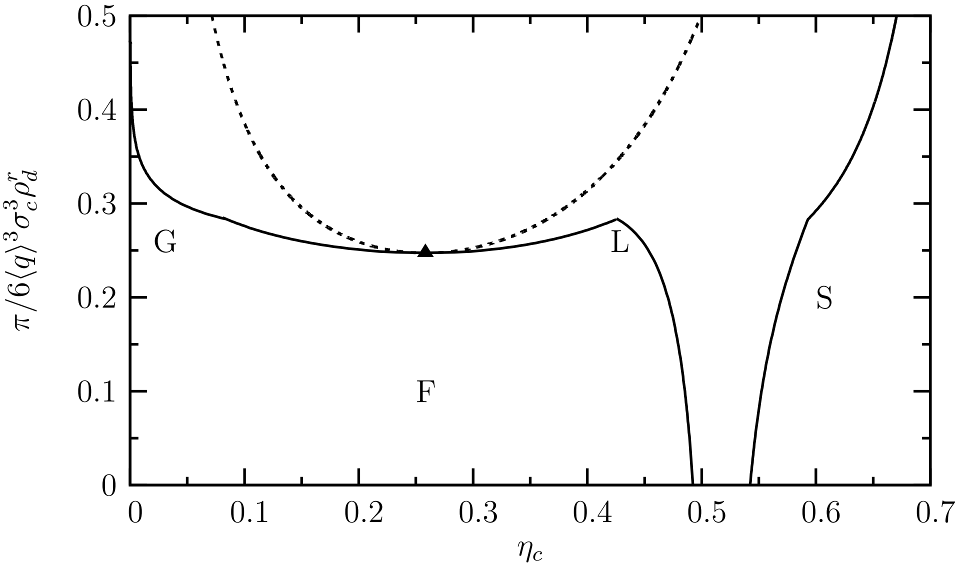

Figure 3.14: Phase diagram for the bimodal distribution of the spherical depletion agent. The degree of polydispersity of both parts in the distribution with $\bar{q} = 0.25$ and $\bar{Q} = 2.0$ is equal, $z = z_{\bar{q}} = z_{\bar{Q}} = 5$. The results are based on the BMCSL equation of state. The mixing parameter is $x = 0.9999$ and the smaller component dominates the mixture. The phase diagram is very close to the one for a monomodal distribution with $\bar{q} = 0.25$.

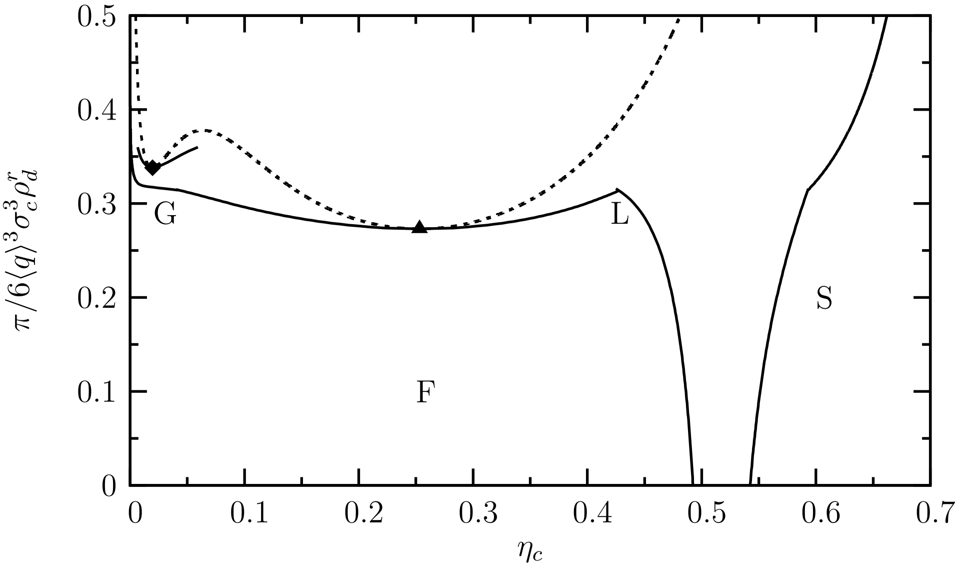

Figure 3.15: Phase diagram for the bimodal distribution of the depletion agent. As it is the case in Fig. 3.14, the distribution is described by $z = 5$, $\bar{q} = 0.25$ and $\bar{Q} = 2.0$. The mixing parameter is $x = 0.995$. We find two minima (filled symbols) of the spinodal line (dashed line). The fluid–fluid coexistence exhibits one stable minimum (triangle).

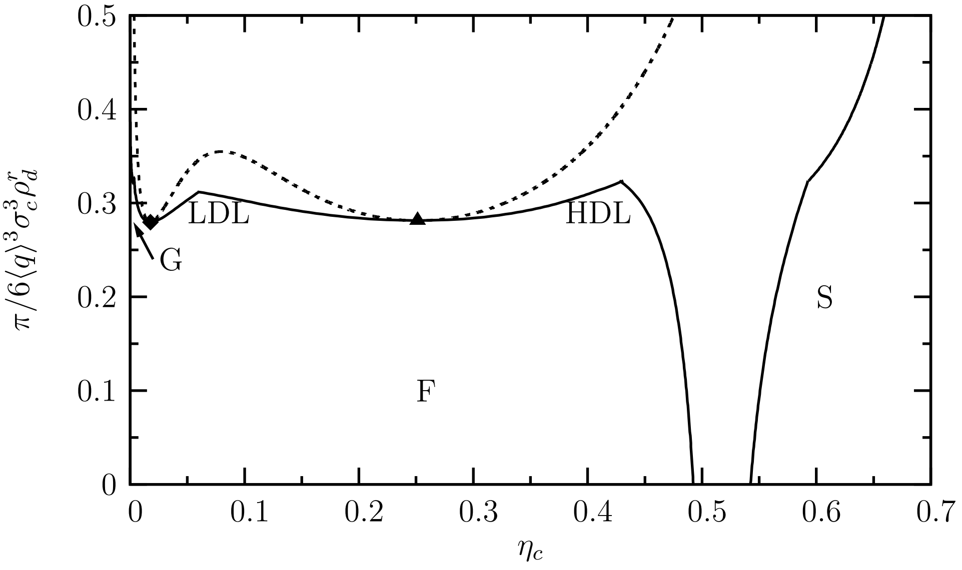

Figure 3.16: For a mixing parameter of $x = 0.9935$ the phase diagram with $z = 5$, $\bar{q} = 0.25$ and $\bar{Q} = 2.0$ exhibits two stable critical points (filled symbols) and three fluid phases: the colloidal gas (G), the low density liquid (LDL) and the high density liquid (HDL).

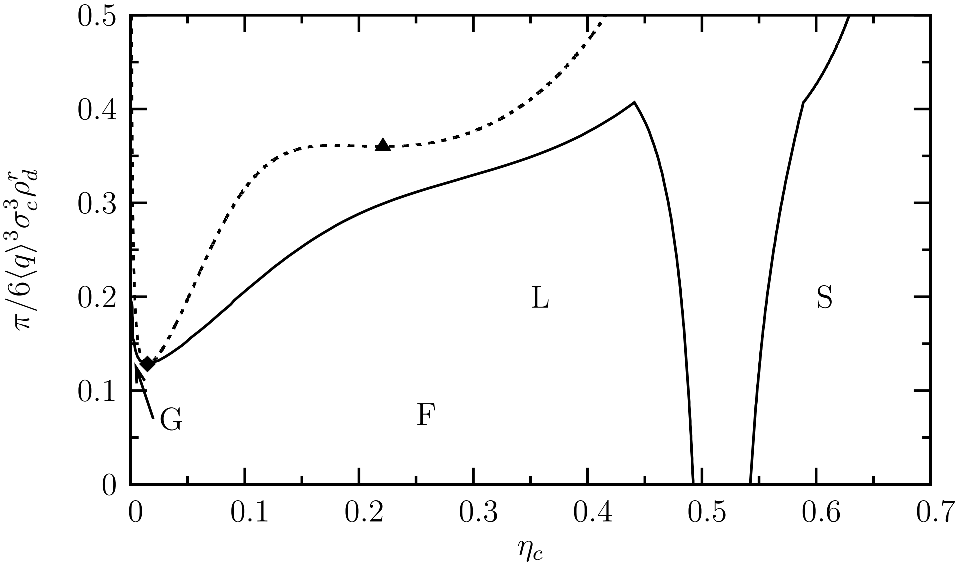

Figure 3.17: Upon increasing the fraction of the depletion agent with larger values of $q$ in the bimodal distribution, $x = 0.98$, we find one critical point at intermediate values of $\eta_c$ shifted to higher values of $\eta_d^r$ and into the metastable regime. The distribution is described by $z = 5$, $\bar{q} = 0.25$ and $\bar{Q} = 2.0$. One liquid phase remains stable as compared to higher values of $x$, where we can find a low and a high density liquid. For further decreasing the value of $x$ the critical point with higher $\eta_c$ (triangle) vanishes.

We observe similar behavior for a mixture of colloids and two monodisperse polymer components, i.e., $z_q$ and $z_Q \to \infty$. For the same size asymmetries as above, $\bar{q} \to q = 0.25$ and $\bar{Q} \to Q = 2.0$, the critical point is metastable when $x = 1$, or equivalently $\langle q \rangle = 0.25$. Upon decreasing the value of $x$ a second critical point occurs at low values of $\eta_c$. For the value $x = 0.995$ — see Fig. 3.19 — we show the phase diagram which exhibits two critical points and observe that one of those is stable (diamond) and one lies in the metastable regime. According to this finding one gas, one liquid and one solid phase are stable. The low density liquid (LDL) and the high density liquid (HDL) phase separation is metastable w.r.t. fluid–solid coexistence.

For the more symmetric case with $q = 0.5$ and $Q = 2.0$ there is a stable critical point for $x = 1$. Similarly to the polydisperse case described above, decreasing $x$ leads to a second *stable* critical point at an intermediate range of $x$ — see Fig. 3.20. In a similar manner as compared to the bimodal polydisperse mixture, besides the gas and the solid phase we observe two stable liquid phases, namely the low density and the high density liquid. To summarize, we find that both by choosing the degree of polydispersity and by accounting for size asymmetry we can study a model fluid which exhibits one or two (stable) critical points and one or two (stable) liquid phases. Furthermore, we have verified that it is possible to generate two critical points and hence *three* fluid phases by using depletion agents of different than spherical geometry.

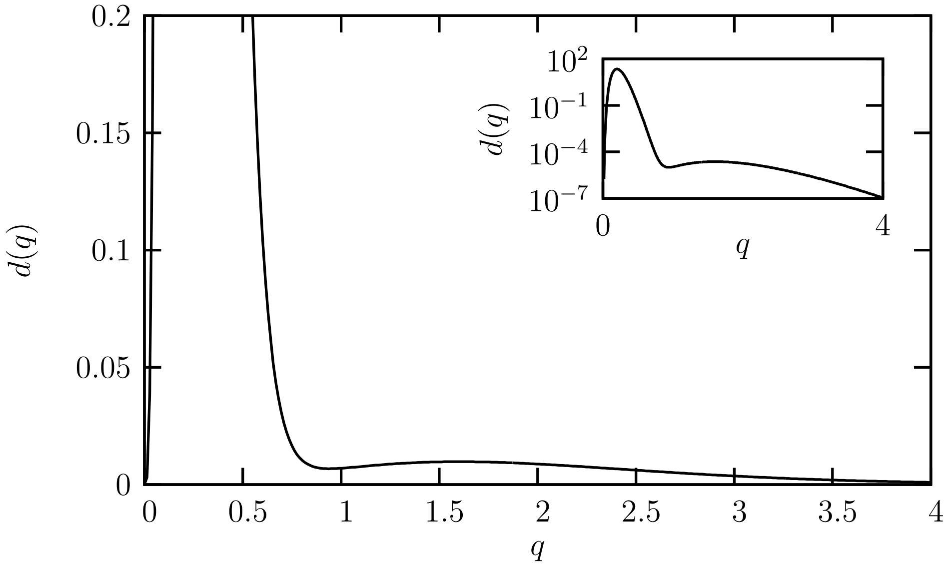

Figure 3.18: The bimodal distribution of the depletion agent with $z = 5$, $\bar{q} = 0.25$ and $\bar{Q} = 2.0$. For the mixing parameter $x = 0.98$ only little contribution comes from high values of $q$. However, this suffices to generate significant effect on the phase diagram.

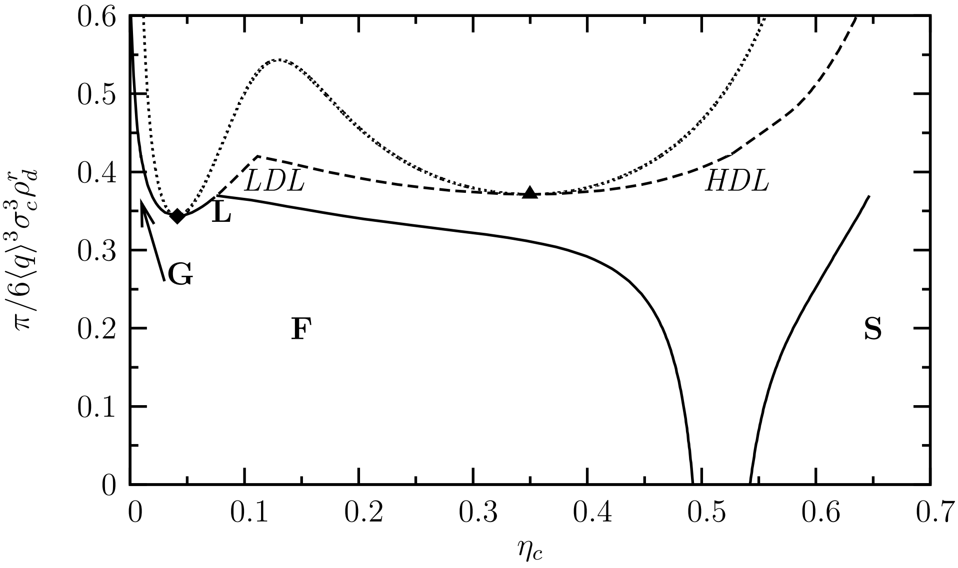

Figure 3.19: Phase diagram of a (discrete) ternary AOV mixture with one colloid species and two (monodisperse) species of the depletion agent with size ratios $q = 0.25$ and $Q = 2.0$. At an intermediate mixing parameter, $x = 0.995$, we observe, similarly to the bimodal distribution of the depletion agent, two critical points. However, only one of those is stable (diamond) while the second lies in the metastable regime (triangle) w.r.t. fluid–solid coexistence. Also, the low and the high density liquid phases are located in the metastable regime (see the dashed lines).

### 3.5.2 Trajectories of critical points

In the previous section we have studied the full phase diagrams of mixtures of colloids and polydisperse depletion agent with a bimodal distribution. For four values of the mixing parameter $x$ we show the phase diagrams of the ternary mixture. In the following we focus on the critical points in the whole range of values of the mixing parameter $x$. We obtain the critical points from evaluating the (local) minimum values in the spinodal line. As we have already done in the example before, we concentrate on the case $z = z_{\bar{q}} = z_{\bar{Q}} = 5$. In Fig. 3.21 we show the trajectory of critical points in a phase diagram for the whole range from $x = 1$ to 0. For $x = 1$ a critical point is found at high values of $\eta_c$. Decreasing $x$, i.e., increasing the contribution of the component corresponding to $\bar{Q} = 2.0$, leads to a shift of the critical point to lower vales of $\eta_c$. At a certain value of $x$ we observe a second critical point indicated by the two filled squares. For further decreasing $x$ both critical points become stable and finally the one with higher values of $\eta_c$ disappears (filled circle). For very low values of $x$ the critical point is shifted to the position from the pure case

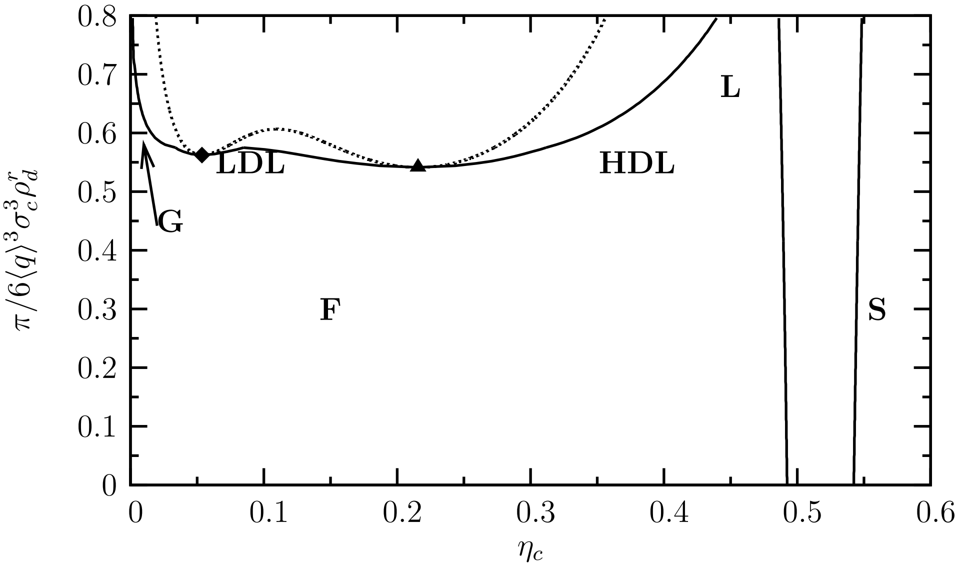

Figure 3.20: Phase diagram of a (discrete) ternary AOV mixture with one colloid species and two (monodisperse) species of the depletion agent with size ratios $q = 0.5$ and $Q = 2.0$. The size ratio between the two species of the depletion agent is less asymmetric as compared to Fig. 3.19. For $x = 1$, where only the component with $q = 0.5$ is present, the fluid–fluid coexistence is stable in contrast to the mixture with $q = 0.25$ (cf. Figs. 3.1 and 3.19). For slightly decreasing the mixing parameter to $x = 0.98$ we find a phase diagram which is qualitatively very similar to that of a bimodal distribution of the depletion agent and $\bar{q} = 0.5$ and $\bar{Q} = 2.0$: We observe two stable critical points (diamond and triangle) and three stable fluid phases, the gas, the low density liquid and the high density liquid.

of a distribution with average value for $\bar{Q} = 2.0$. For decreasing asymmetry between both components, i.e., for lower ratio $\bar{Q}/\bar{q}$, the gap in the trajectory becomes smaller — see the dashed line in Fig. 3.21. The open squares ($x = 0.9668$) and the open circles ($x = 0.97$) for $\bar{q} = 0.5$ have analogous meaning to the case where $\bar{q} = 0.25$ ($x = 0.9786$ and $0.9966$). Upon further decreasing the size asymmetry to $\bar{q} = 0.5$ and $\bar{Q} = 1.5$ the trajectory of the critical points in the phase diagram is continuous in the whole range of the mixing parameter, $x \in [0, 1]$, and we find only one (stable) critical point for all values of $x$. Figure 3.22 displays the colloid packing fractions $\eta_c$ of the trajectories of the critical points for a wide range of the parameter $x$. The symbols have the same meaning as in the phase diagram, cf. Fig. 3.21. In the ($x$,$\eta_c$)-representation we can more clearly see that for the more asymmetric distributions we find a range of $x$ where two critical points appear simultaneously.

In the limiting case of a bidisperse distribution where $z_{\bar{q}} \to \infty$ and $z_{\bar{Q}} \to \infty$, i.e., the discrete ternary mixture, we observe similar behavior of the trajectory of critical

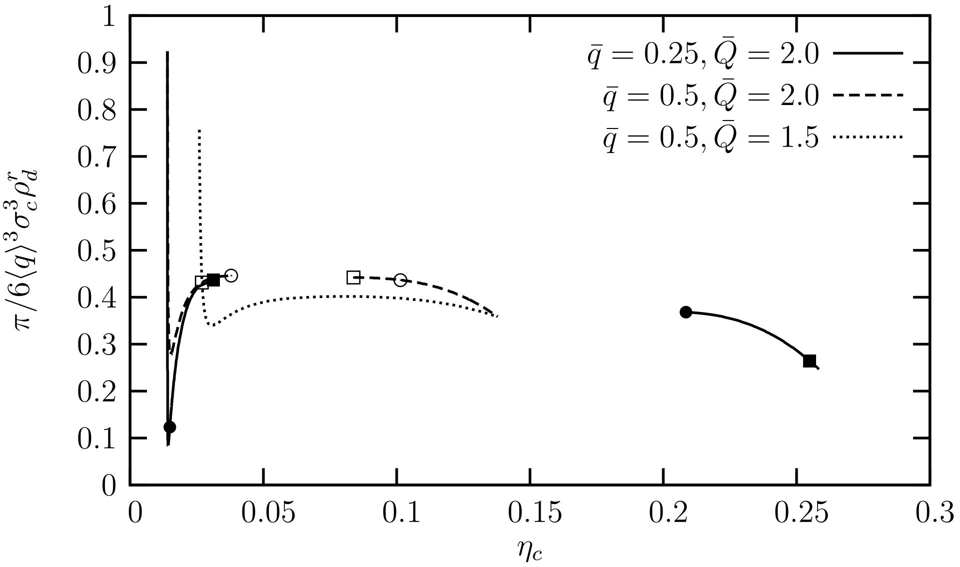

Figure 3.21: Trajectories of critical points in phase diagram for varying mixing parameter $x$ in the bimodal distribution $d_S(q;x)$ with $z = 5$. For $x = 1$ the critical point takes the highest value of $\eta_c$. For decreasing $x$ the critical points move to lower $\eta_c$ and, for the asymmetric cases, we observe two critical points in the range bound by the squares and the circles that occur simultaneously for a certain value of $x$. As we have shown in the phase diagrams (see Fig. 3.16) for $\bar{q} = 0.25$ and $\bar{Q} = 2.0$ we find a range of $x$ where two critical points are stable at the same time. In the symmetric case (dotted line) the trajectory is continuous. Only one critical point can occur for these parameters.

points.

## 3.6 Conclusions

In this chapter we have presented three main results. Firstly, we have generalized a novel approach to free-volume theory [51] based on FMT [13, 96, 97] to treat a depletion agent of arbitrarily shaped particles with a continuous distribution. Here, we introduced one parameter, $q$, to specify a continuously varying distribution of depletion agent. Secondly, we employed our approach to treat mixtures of colloids and polydisperse depletion agent of various shape. And thirdly, we used the general character of our approach to study ternary mixtures of one colloid species and two species of the depletion agent.

To evaluate the phase diagram within FVT an expression for the free-volume fraction is required. In the case of polydisperse size or shape distributions for the depletion agent, one can obtain an *effective* free-volume fraction, which in general

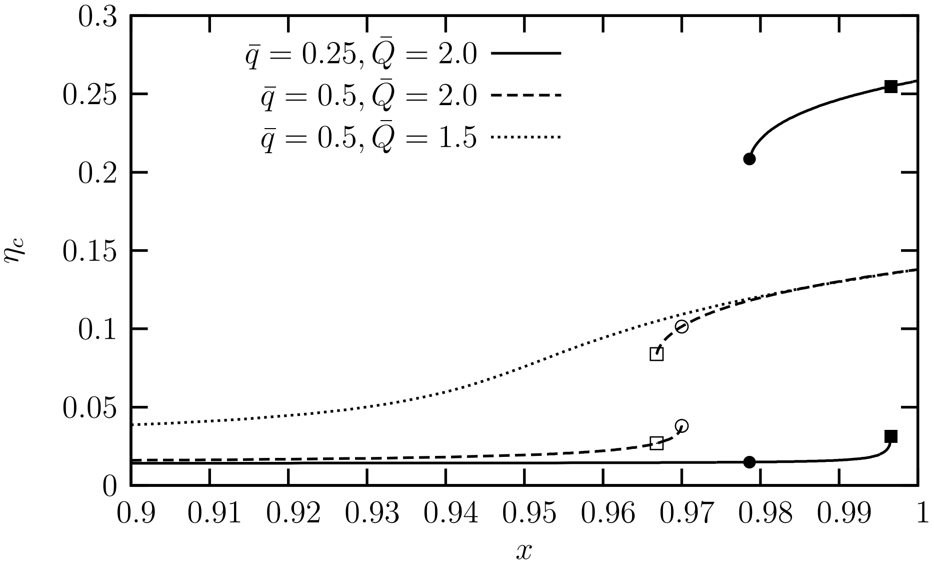

Figure 3.22: Colloid packing fraction of the critical points for varying mixing parameter $x$ in the bimodal distribution $d_S(q;x)$ with $z = 5$. The symbols have equal meaning as in the trajectories in phase diagram — see Fig. 3.21. In the range between the squares and the circles we find two critical points. Note that stability is not shown in this figure. For high asymmetry (full line) the range with two critical points is $x \in [0.9786, 0.9966]$, for intermediate asymmetry (dashed line) we find $x \in [0.9668, 0.97]$.

has to be calculated numerically. In the cases of infinitely thin needles or platelets we presented explicit expressions for the effective free-volume fraction $\alpha_{\text{eff}}$ for various distributions. Beside size polydispersity, we have also considered morphology polydispersity. To this end we have calculated phase diagrams of a mixture of colloidal spheres and ellipsoidal depletion agent. Based on our results we confirm that polydispersity has the tendency to stabilize the fluid–fluid coexistence region w.r.t. crystallization. This finding is in agreement with earlier studies [42, 101, 102] for size polydisperse spherical polymer coils. Moreover, we have shown that a similar behavior can be found for the case of shape polydispersity. Upon increasing the degree of polydispersity the fluid–fluid binodal crosses the fluid–solid coexistence line, and one obtains a stable critical point with associated liquid and gas phases and a triple point. This effect seems to be robust against various ways to incorporate polydispersity, which can be rationalized by the fact that particles of a polydisperse depletion agent can fill the available free volume in a system better than a monodisperse species.

The presented results are based on the White Bear version of FMT and the corresponding BMCSL equation of state (e.o.s.). As that e.o.s. is used for evaluating the effective free-volume fraction $\alpha_{\text{eff}}$ and for the pressure, our approach provides a consistent route. It is also possible to base the free-volume theory on a recent, slightly more consistent, mixture equation of state [82, 83]. We have studied the phase behavior based on expressions for pressure from the equation of state and from $\partial\Phi/\partial n_3$. We confirm that both routes give very similar results and the original White Bear version provides a consistent and accurate route.

We presented a remarkable result in Sec. 3.5 for mixtures of colloids and two components of polydisperse (spherical) polymer coils. The polymers were described by a bimodal distribution consisting of two polydisperse distributions, which within our approach can be done in a straightforward manner. For the averaged size ratios of the polymer components chosen here, $\bar{q} = 0.25$ and $\bar{Q} = 2.0$, we find for each of the values a fluid–fluid coexistence line in distinct parts of the phase diagram, i.e., in the two limiting cases $x = 1$, when only the smaller polymer species is present, and $x = 0$, when only the larger polymer species is present. For $x = 0$ the corresponding fluid–fluid phase separation is stable independent of the degree of polydispersity. In the second limiting case, $x = 1$, the fluid–fluid phase separation has to be stabilized by a sufficient degree of polydispersity. We choose $z_{\bar{q}} = z_{\bar{Q}} = 5$ and find for a range of the mixing parameter $x$ two stable liquid phases: Beside the gas phase, which is diluted in the density of colloids, we find a low density and a high density liquid phase. The fluid–fluid coexistence region is w shaped in this case, and the phase diagram exhibits two stable critical points and two triple points. For systems with two length scales in the inter-particle interactions, such as short-range repulsion and long-range attraction, Hemmer and Stell [52,53] found that two stable critical points may occur. More closely related to our situation is a system of star polymers [55] in which similar features of the phase diagrams are reported, since the effective interaction potential is comparable to those of the model of Stell and Hemmer. For other model fluids similar effects were observed [54, 103, 104]. We point out that our findings are not restricted to a polydisperse depletion agent. We find similar results for a ternary mixture in which we consider one colloid component and two distinct monodisperse components of depletion agent.

In theoretical and experimental studies polydispersity of any kind often is considered an undesirable side-effect. In experiments polydispersity may originate from imperfections of the particle synthesis. Based on our findings it is possible to make use of polydispersity by stabilizing fluid–fluid phase separations. Moreover, controlling the degree of polydispersity allows one to some degree to tune the phase diagram. From this point of view one might speculate about the opportunity of designing the phase behavior of colloidal mixtures by specifying the polydisperse distribution of the depletion agent.

# Chapter 4

# Fluids in Confined Geometry

When a *bulk* gas is confined in a narrow capillary with strongly attractive wall-particle interaction (hydrophilic pore) one might find a stabilized fluid phase and hence condensation [35, 56–58] of the fluid. On the other hand, when a *bulk* liquid is confined in a pore with strongly repulsive wall-particle interactions (hydrophobic pore) one might observe evaporation [59, 60, 66]. This observation is found for a wide range of fluids. A colloid-polymer (*cp*) mixture in the bulk exhibits fluid–fluid phase separation into a colloid poor (gas) and a colloid rich (liquid) phase and features phenomena observed also in simple fluids. For the AOV model we presented results concerning the bulk phase behavior in the previous chapter. In the following chapter we restrict ourselves to the *cp* mixture with monodisperse colloid and polymer components. All particles have spherical geometry. When the AOV mixture is brought to a single wall one finds rich surface phase behavior with layering transitions [22] and wetting [105] phenomena. This leads to the interesting question what happens when the AOV mixture is confined in a narrow slit-like pore as one expects a competition between the gas, the layering and the liquid phase. An analogous situation concerning the competition between capillary condensation and pre-wetting for simple fluids [106] is described in literature. In experiment confocal scanning microscopy allows one to study colloid-polymer mixtures in confined geometry [29].

The confined fluid in a slit-like pore exerts an excess pressure on the confining walls. Experimentally such an excess pressure, expressing itself in solvation forces, can be accurately measured by the surface force apparatus [61, 62] and in fluids confined between two mica plates [63, 64] which has also been applied to situations where capillary condensation occurs [65]. In addition to the phase behavior in the narrow pore we study its influence on the solvation force between two walls.

# 4.1 Phase behavior of the confined colloid-polymer mixture

## 4.1.1 Bulk phase behavior

In the previous chapter we presented the bulk phase behavior of the colloid-depletion agent mixture in detail. In this chapter we focus on a depletion agent which models polymer coils and we study mixtures of colloids $c$ and polymer $p$. Within the semi-grand canonical ensemble the phase diagram is described in terms of the packing fraction $\eta_c$ of the colloids in the system and the packing fraction $\eta_p^r$ of the polymer in the reservoir. For a wide range of values of the size ratio $q = \sigma_p/\sigma_c$ between the diameter of the spherical polymer and the diameter of the spherical colloids we showed the bulk phase diagrams in Figs. 3.1 and 3.2. We choose $q = 0.6$ in the following study. Many results are known for that particular value as it is frequently used in DFT studies and simulations [38, 84].

In Fig. 3.2 the dashed line shows the phase diagram for $q = 0.6$ based on the Carnahan-Starling equation of state obtained via free-volume theory. We find phase coexistence for chemical and mechanical equilibrium, i.e., if $\mu_c^I = \mu_c^{II}$ and $p^I = p^{II}$, respectively. At vanishing polymer packing fraction $\eta_p^r = 0$, i.e., for the pure one-component hard-spheres, one finds a fluid phase for $\eta_c \lesssim 0.494$ and a (colloidal) crystal for $\eta_c \gtrsim 0.54$. Upon increasing the polymer density above the critical point we find fluid–fluid phase separation into a gas (colloid poor) phase and a liquid (colloid rich) phase. Upon further increasing the polymer density a three-phase coexistence between the gas, the liquid, and the solid phase occurs. At values of $\eta_p^r$ above the triple point the gas–solid coexistence is stable. In this representation the polymer density in the reservoir takes the role of an inverse temperature. Increasing $\eta_p^r$ leads to a more pronounced colloid-colloid attraction.

## 4.1.2 Phase behavior at walls

A bulk colloid-polymer mixture modeled by the AOV fluid at a state-point close to the fluid–fluid coexistence undergoes further transitions when it is brought in contact with a substrate. For the case of a planar hard wall we can observe a series of layering transitions labeled $\tau_{i-j}$ between layering states $\lambda_i$ and $\lambda_j$. At the transition $\tau_{0-1}$ we find coexistence between a gas phase and a gas with one liquid like layer $\lambda_1$ adsorbed at the hard wall. Further transitions between states with more than one adsorbed liquid layer are possible. Accordingly, $i$ and $j$ denote the number of the adsorbed liquid layers, in these terms $i = 0$ denote the gas (with no liquid layer adsorbed). At

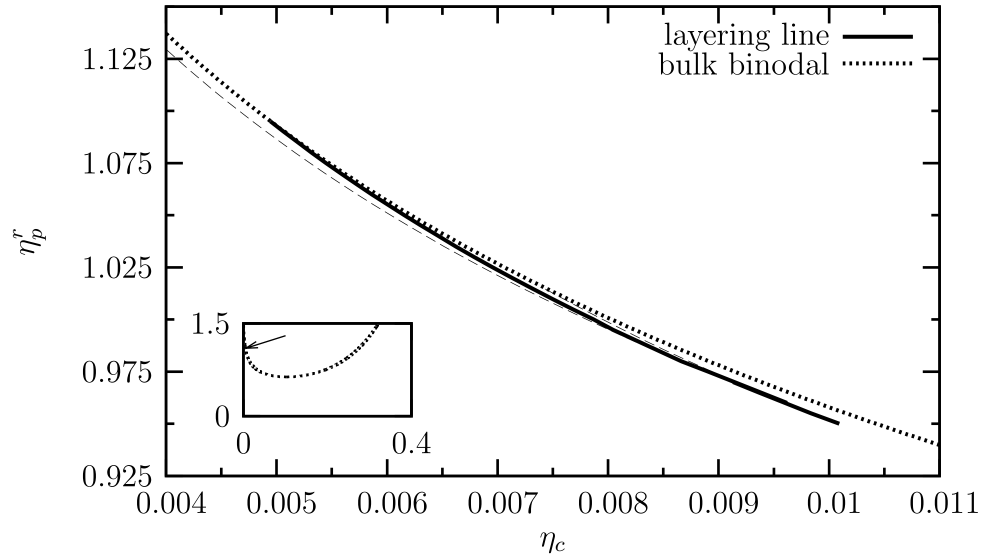

Figure 4.1: Layering line which displays the position of the transition between the (colloidal) gas phase and the first layering state for a colloid-polymer mixture with size ratio $q = 1.0$. The result is based on the MCSL equation of state. For values of $\eta_c$ below the layering line (full line) we find a stable gas phase. Above the transition line $\tau_{0-1}$ the first layer is stable. Note that transitions between further layering states are not considered in this figure. The dashed lines display the region where for $\eta_c$ below the layering line the layering occurs but is metastable, and for $\eta_c$ above the layering line the gas can be found but is metastable. The dotted line displays the corresponding fluid–fluid binodal in bulk. The arrow in the inset points to the region of the layering states.

the transitions we find a jump in the excess adsorptions of the colloids $\Gamma_c$ and the polymer $\Gamma_p$. However, the grand potential $\Omega$ is continuous but non-analytic upon increasing the colloid packing fraction $\eta_c$, for example. At this first order phase transition the equality of the grand potential $\Omega = -pV + \gamma A$ leads to a continuous but non-analytic surface tension $\gamma$. Hence, we find the coexistence lines by equating the surface tensions for the two different phases. The same relations hold for the transitions $\tau_{1-2}$, $\tau_{2-3}$, and so forth, between states which differ by one layer. At a lower value of $\eta_p^r$ we also find a point of complete wetting. In the following we choose state-points sufficiently far away from this point.

In Figs. 4.1 and 4.2(a) we show layering lines for $q = 1.0$ and 0.6. For $q = 0.6$ and the PY equation of state we display the transition by the line $\tau_{0-1}$ in Fig. 4.2(b). We confirm and highlight that results based on both, the PY and the MCSL, equations of state exhibit layering transitions to states with more than one liquid like layer, $\tau_{1-2}$, $\tau_{2-3}$, and so forth (not shown in the figures for clarity of display). In the following we

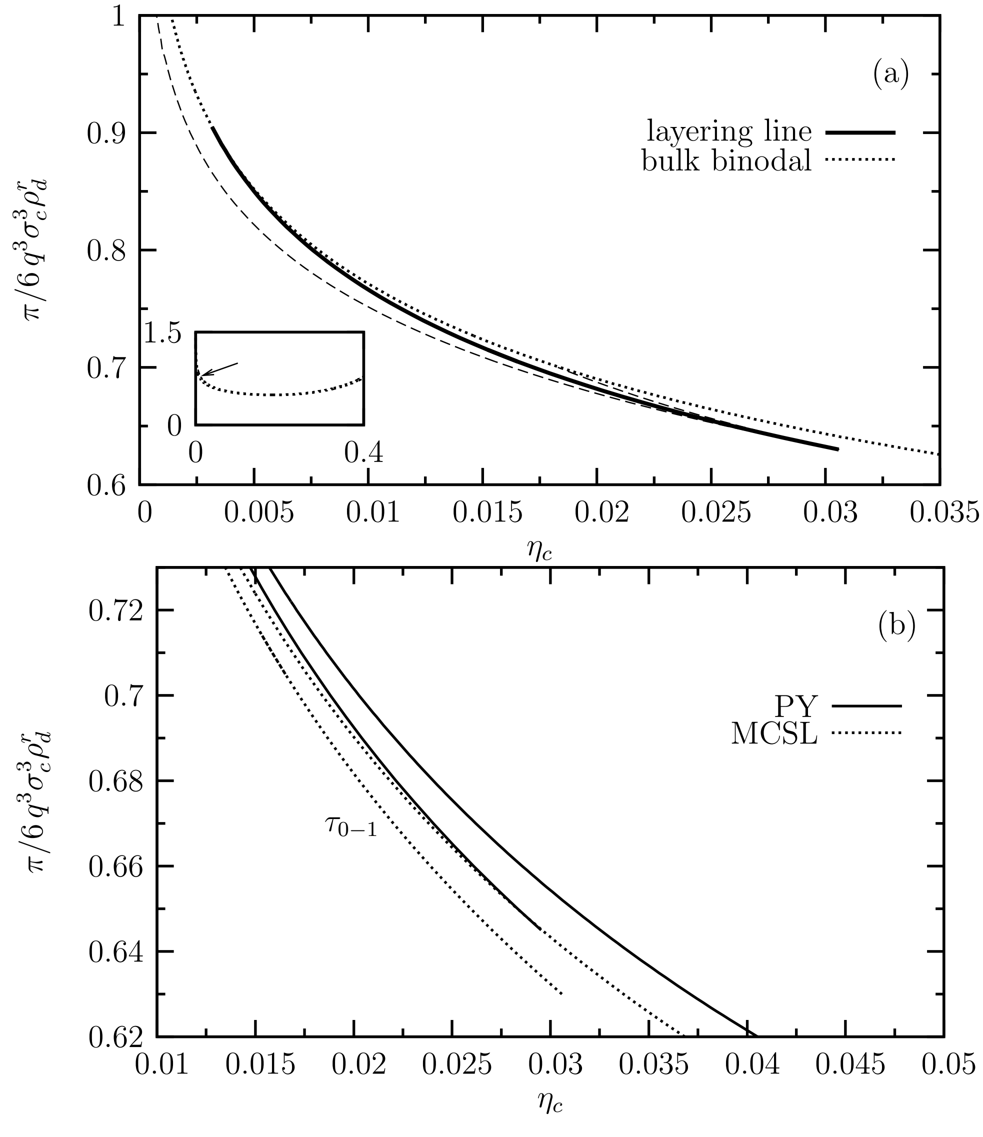

Figure 4.2: (a) We display the layering line $\tau_{0-1}$ (full line) for the MCSL equation of state and $q = 0.6$ in a wide range of $\eta_p^r$. The dashed lines show the region where two phases may exist, one being metastable. Note that further layering transitions ($\tau_{0-2}$ and so forth) are not shown. The inset shows the position of layering states as compared to the fluid–fluid binodal (dotted line). (b) We compare the results based on the PY (full lines) and the MCSL (dotted lines) equation of state. Both, the layering line and the fluid–fluid binodal, apart from a vertical shift, exhibit similar behavior in the two cases.

focus on the result corresponding to the MCSL equation of state. Within DFT this is achieved by the White Bear version of FMT. As the layering lines between states with more than one layer are very close to the bulk fluid–fluid coexistence we restrict our considerations to $\tau_{0-1}$. At the layering lines [full lines in Figs. 4.1 and 4.2(a)] it follows from equality of the grand potentials in both phases that the corresponding surface tensions are equal: $\gamma^{\lambda_i} = \gamma^{\lambda_j}$. The dashed lines display regions in which both phases, which coexist at $\tau_{0-1}$, can occur. However, for $\eta_c$ below the transition the layering $\lambda_1$ is metastable. For $\eta_c$ above the transition the gas phase is metastable. In an analogous fashion the same behavior is found at other transitions $\tau$. Obviously, the surface phase diagram which contains all the layering transitions is very rich. We focus on the transition between the gas and one layer and indicate its location in the bulk phase diagram w.r.t. the fluid–fluid phase coexistence in the insets of Figs. 4.1 and 4.2.

**Influence of polydispersity on layering**

Before we study the AOV mixture confined in a slit of two planar hard walls we rise the question how robust or generic the layering behavior is. We already pointed out that for different underlying equations of state, namely the PY and the MCSL e.o.s., we find layering transitions which exhibit little difference apart from a vertical shift. As the colloid-polymer mixture is a two component fluid we study the influence of the many-component character of a mixture and the effect of polydispersity. To this end we introduce a discrete Gaussian distribution with a finite number of components. Since FMT in constructed to treat mixtures this system can be studied in a straightforward fashion.

First we consider the $\lambda_1$ liquid layer, i.e., the phase with one layer. The polydisperse distribution is given by Eq. (3.8). We study four possible cases: i) monodisperse colloid and monodisperse polymer, ii) polydisperse colloid and monodisperse polymer, iii) monodisperse colloid and polydisperse polymer, and iv) polydisperse colloid and polydisperse polymer. Note that within the DFT approach polydispersity is modeled by a discrete distribution of single monodisperse components. The degree of polydispersity is given by $z_c = 100$ and $z_p = 100$. In Eq. (3.8) the parameter $z$ describes the broadness of the distribution and the subscript labels the polydisperse species. Note that the fugacity is sometimes labeled by the same symbol. The colloid distribution is described by 21 components and $\bar{\eta}_c = 0.0263$ if the colloids are polydisperse, otherwise $\eta_c = 0.0263$. Analogously, the polymer distribution is described by 25 components and $\bar{\eta}_p = 0.581166$ if the polymer species is polydisperse, otherwise $\eta_p = 0.581166$.

In Figs. 4.3 and 4.4 we show the colloid density profiles $\rho_c(z)$ and the polymer

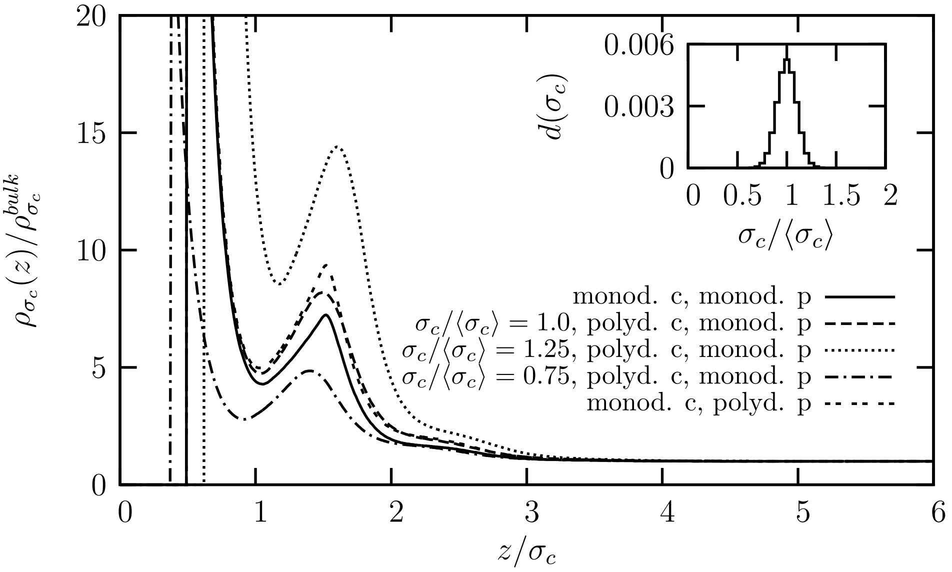

Figure 4.3: Colloid density profiles $\rho_c(z)$ of the colloid-polymer mixture with $q = \langle\sigma_p\rangle/\langle\sigma_c\rangle = 0.6$ at a planar hard wall. The state-point is fixed and lies in the region of the first layering state $\lambda_1$. The full line shows the profile for monodisperse components $c$ and $p$. The remaining profiles $\rho_c(z)$ show results for either polydisperse colloids or polydisperse polymer. The inset diplays the polydisperse size distribution of the colloids. The dashed line shows the profile of the component $\sigma_c/\langle\sigma_c\rangle = 1.0$ of the discrete distribution. The components $\sigma_c/\langle\sigma_c\rangle = 1.25$ (dotted line) and $\sigma_c/\langle\sigma_c\rangle = 0.75$ (dash-dotted line) display stronger or weaker layering structure, respectively, as compared to the component with $\sigma_c/\langle\sigma_c\rangle = 1.0$. In the case of monodisperse colloid and polydisperse polymer the profile is shown by the double-dashed line. In all profiles we find layering behavior.

density profiles $\rho_p(z)$, respectively, for the cases i), ii) and iii). In Fig. 4.3 we show results for the monodisperse reference system and for three selected components of the distribution of polydisperse colloids (see inset) with $\sigma_c/\langle\sigma_c\rangle = 1.25$, 1.0 and 0.75. The double-dashed line shows the result for monodisperse colloids and polydisperse polymer. When both species are polydisperse higher layering states or wetting seems to be preferable.

Accordingly, we find layering behavior in the polymer density profiles — see Fig. 4.4. The monodisperse reference system (full line) and the result for polydisperse polymer are similar — see the profiles for the component with $\sigma_p/\langle\sigma_c\rangle = 0.75$, 0.45 and those with maximum contribution $\sigma_p^* = 0.6\langle\sigma_c\rangle$. See the inset for the distribution of the polymer. The double-dashed line displays the behavior for monodisperse polymer and polydisperse colloids.

In all cases we find layering behavior. The liquid layer state $\lambda_1$ seems to be robust

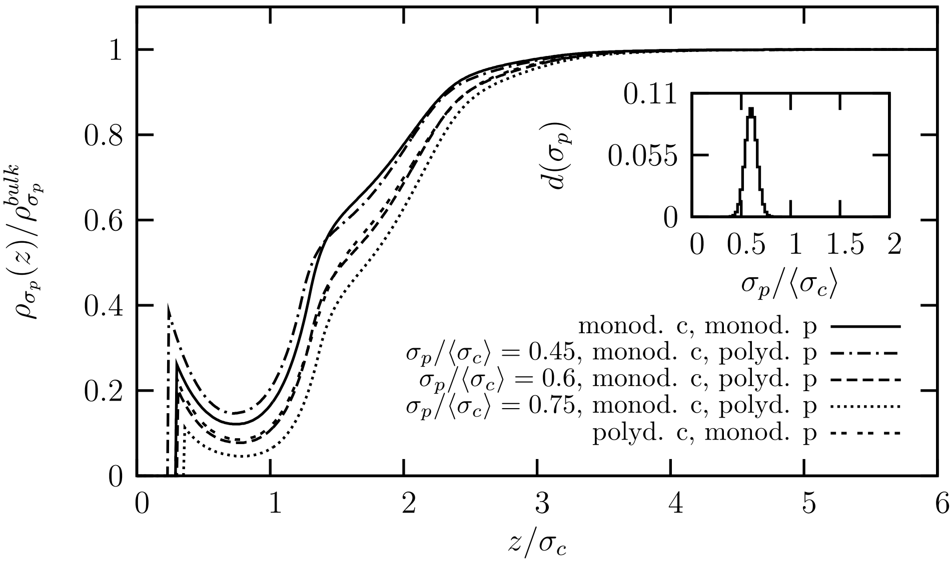

Figure 4.4: Polymer density profiles $\rho_p(z)$ of the colloid-polymer mixture at a planar hard wall. For a state-point in the first layering regime $\lambda_1$ we show results for one polydisperse species. The monodisperse reference system is shown by the full line. The profile of the component at maximum packing fraction $\sigma_p/\langle\sigma_c\rangle = 0.6$ in the distribution is shown by the dashed line. For smaller ($\sigma_p/\langle\sigma_c\rangle = 0.45$) or larger ($\sigma_p/\langle\sigma_c\rangle = 0.75$) size of the polymer the profiles are shown by the dotted or dash-dotted lines, respectively. For a comparison with the effect of monodisperse polymer and polydisperse colloids (with the distribution from Fig. 4.3) we display the corresponding result by the double-dashed line. All profiles display layering structure corresponding to the $\lambda_1$-state.

against varying the description of the colloid-polymer mixture. Moreover, we also find layering states of higher order when polydispersity is introduced. We confirmed this finding up to the forth layering transition and a distribution with $z_c = 50$.

### 4.1.3 Phase behavior in slit-like pores

In contrast to the bulk phase behavior, where we considered homogeneous (constant) densities, we employ the DFT route to obtain the phase behavior in the slit geometry for inhomogeneous density profiles. To this end we employ the FMT formalism for colloid-polymer mixtures. The density functional for the mixture is given by

$$\Omega[\rho_c,\rho_p] = \beta^{-1}\int \mathrm{d}\mathbf{r}\Phi^{AOV}(\{n_\alpha^c, n_\alpha^p\}) + \sum_{i=c,p}\mathcal{F}_{id}[\rho_i] + \sum_{i=c,p}\int \mathrm{d}\mathbf{r}\rho_i(\mathbf{r})\left(V_{ext}^i(\mathbf{r}) - \mu_i\right). \tag{4.1}$$

We use the linearized (w.r.t. the polymer density) version of the White Bear version of FMT to describe $\Phi^{AOV}(\{n_\alpha^c, n_\alpha^p\})$ given in Eq. (2.38). The ideal gas contribution

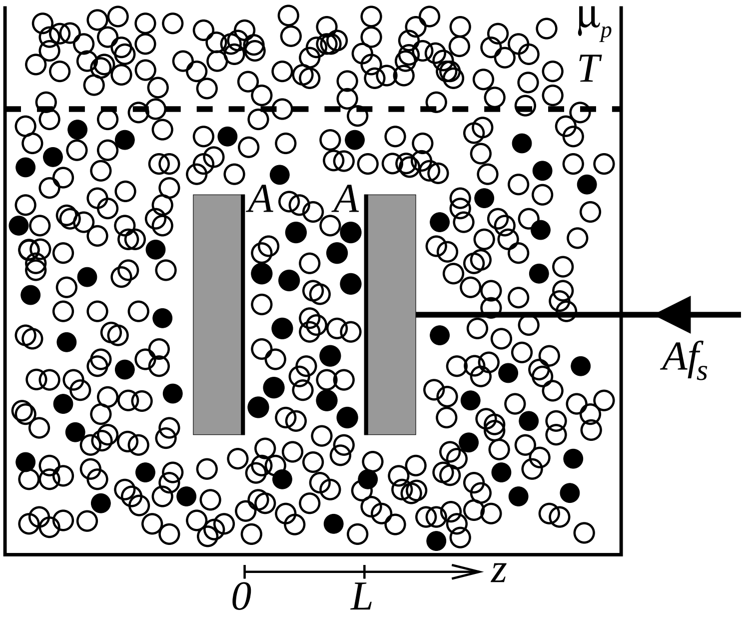

Figure 4.5: A colloid-polymer mixture confined between two planar parallel plates of infinite surface area $A$ and at distance $L$. The colloids (filled circles) are restricted to the system indicated by the thick dashed line. Within the semi-grand canonical description the polymer component (open circles) is in contact with a reservoir at temperature $T$ and chemical potential $\mu_p$. As indicated by the thick dashed line the polymer can exchange position between the system and the reservoir.

for the mixture with components $i$ is a straightforward generalization of Eq. (2.17) and we get $\beta\mathcal{F}_{id}[\rho_i] = \int d\mathbf{r}\rho_i(\mathbf{r})(\ln\lambda_i^3\rho_i(\mathbf{r}) - 1)$. For the mixture with species $c$ and $p$ the minimization condition results in two coupled equations (2.40) which have to be solved simultaneously.

In the semi-grand canonical ensemble the narrow slit-like capillary is filled with colloids $c$ and polymer $p$, see Fig. 4.5. The polymer is connected to a reservoir at temperature $T$ and chemical potential $\mu_p$. The (infinite) surface area of the pore amounts to $2A$. We consider one fixed planar hard wall and one planar hard wall at separation $L$. Due to packing effects and phase transitions one finds an excess pressure on the walls of the system. Positive values of the excess pressure $f_s$, or equivalently the force $Af_s$, represent repelling walls.

We obtain the phase behavior in the capillary from thermodynamic quantities that follow from the minimization procedure. From the density profiles we obtain the excess adsorption of the component $i$ from

$$\Gamma_i = \frac{1}{A}\int_V \mathrm{d}\mathbf{r}(\rho_i(\mathbf{r}) - \rho_i^{bulk}). \tag{4.2}$$

The excess contribution to the grand potential due to confinement originates from the fact that inhomogeneous density profiles develop. It is described by the surface tension which is defined as

$$\gamma = \frac{1}{A}\left(\Omega[\rho_c, \rho_p] + pV\right). \tag{4.3}$$

Both, $\Gamma_i$ and $\gamma$, are related via the Gibbs adsorption theorem

$$\Gamma_i = -\left(\frac{\partial \gamma}{\partial \mu_i}\right)_{T,V}. \tag{4.4}$$

It is important to note that the surface tension and the excess adsorption depend on the definition of the dividing interface. We choose the position of the planar hard wall as the dividing interface.

As already mentioned above, the presence of two confining walls may lead to capillary condensation of a bulk gas. The transition between the gas $g$ and liquid $l$ phase happens for state-points in the vicinity of the bulk fluid–fluid binodal. In both phases the grand potential for the mixture confined in the capillary in terms of the pressure $p_\alpha$ and the surface tension $\gamma_\alpha$ in each phase is approximated by

$$\Omega_\alpha \approx -p_\alpha AL + 2\gamma_\alpha A. \tag{4.5}$$

For very narrow slits correlations between the walls require further corrections. Note that $2A$ is the total surface area that originates from the two confining walls. At coexistence the grand potentials of both phases are equal,

$$\Omega_g(L) = \Omega_l(L), \tag{4.6}$$

and from Eq. (4.5) we obtain the wall-wall separation

$$L_{cond} \approx \frac{2\gamma_{wg} - 2\gamma_{wl}}{p_g - p_l} \tag{4.7}$$

at which capillary condensation occurs. Close to the bulk coexistence we can observe condensation at large values of the slit width $L_{cond}$, which comes from the fact that the difference between the pressures is small near coexistence and vanishes right at the coexistence. For small values of $L$ correlation effects between the two confining walls can be significant. These corrections in the grand potential have to be taken into account when very narrow pores are studied. The above treatment strictly holds only for wide slits. Indeed, for very narrow slits correlation effects due to the strong confinement lead to a shift of the layering line, which itself is a surface phase transition. The shift $\delta\eta_c$ in the layering line exhibits exponential behavior on $L$, in a similar fashion to the findings for the pre-wetting line, $\delta\eta_c \propto \exp\left(-L/\xi\right)$, where

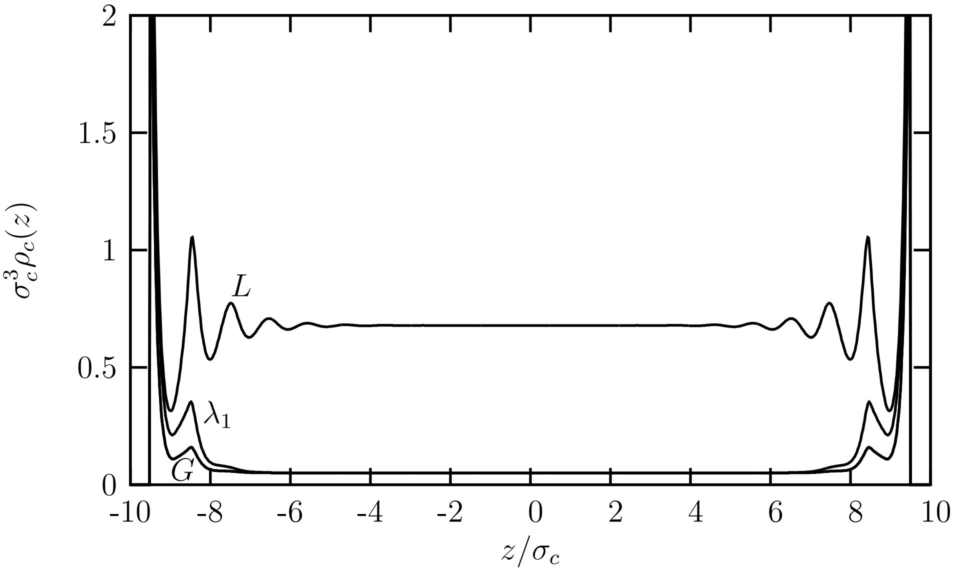

Figure 4.6: Colloid density profiles $\rho_c(z)$ of a colloid-polymer mixture with size ratio $q = 0.6$ confined between two parallel planar hard plates at distance $L = 20\sigma_c$. The lines show profiles of three different phases: the gas $(G)$, the layering $(\lambda_1)$ and the liquid $(L)$ phase. For the chosen state-point, $\eta_c = 0.0262$ and $\eta_p^r = 0.65$, the layering is stable.

the decay length $\xi$ is in the range of the correlation length of the gas, $\xi \approx \xi_{gas}$. Equation (4.7) can be rewritten into a one-component Kelvin equation [107] and $\Delta\mu_c = (2/L)(\gamma_{wl} - \gamma_{gl})/(\rho_c^l - \rho_c^g)$. We find $\rho_c^l - \rho_c^g \propto 1/L$ and, to compare with the findings for the shift of the layering line, $\delta\eta_c \propto 1/L$ at fixed polymer packing fraction $\eta_p^r$. The different behavior of the gas–liquid transition, where we find a power law behavior $1/L$ in the shift of the transition, as compared to the layering transition, where we find exponential shift, indicates a rich behavior due to the competition of both transitions.

In order to demonstrate the competition between the layering transitions and capillary condensation we choose a fixed value of the wall-wall distance $L$ and a state-point where both effects play a significant role. We restrict our consideration to the size ratio $q = 0.6$, but we have checked that similar effects can be observed for other size ratios where we find fluid–fluid phase separation and layering. We choose $\eta_p^r = 0.65$. For this value the layering line is in suitable distance from the fluid–fluid binodal and the state-points are far away from the layering critical point.

In the following we consider two routes. For a fixed state-point we vary the slit width $L$, or for fixed slit-width $L$ we vary the state-point by varying the value of $\eta_c$ at fixed $\eta_p^r = 0.65$. The latter route corresponds to trajectories along horizontal tie lines in the $(\eta_c, \eta_p^r)$ representation of the phase diagram. In Fig. 4.6 we show three density

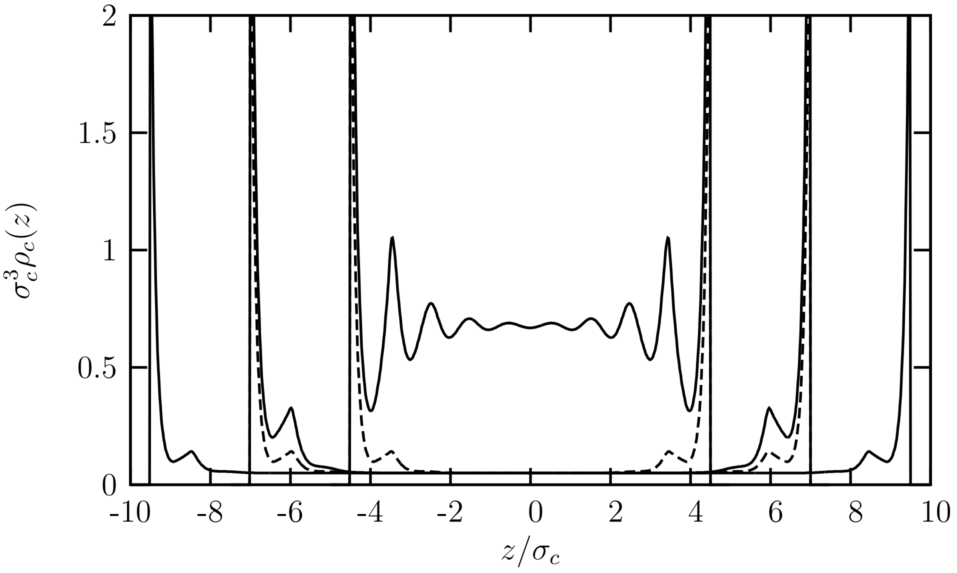

Figure 4.7: Colloid density profiles $\rho_c(z)$ of a colloid-polymer mixture with size ratio $q = 0.6$ confined between two hard walls. The state-point is fixed in all cases, $\eta_c = 0.0262$ and $\eta_p^r = 0.65$, while the wall-wall separation is varied $L = 20\sigma_c$, $15\sigma_c$ and $10\sigma_c$. For the largest separation ($L = 20\sigma_c$) we find a stable gas phase (full line) and metastable layering and liquid phase (not shown in this figure). Upon decreasing the separation ($L = 15\sigma_c$) we observe stable layering structure (full line) while the gas phase has become metastable (dashed line). At small separations ($L = 10\sigma_c$) we observe capillary condensation and the liquid phase is stable (full line) while the colloidal gas phase (dashed line) and the layering are metastable.

profiles $\rho_c(z)$ of the colloid component for fixed $L = 20\sigma_c$ *and* fixed state-point. We find three density profiles for $\eta_c = 0.0262$, however, those for the gas phase ($G$) and the liquid ($L$) are metastable w.r.t. layering $\lambda_1$. The stability follows from comparing the values of the resulting grand potentials: $\Omega_{\lambda_1} < \Omega_g$ and $\Omega_{\lambda_1} < \Omega_l$. We study the stability in more detail in the next section.

Figure 4.7 shows colloid density profiles for three different values of the slit width $L = 20\sigma_c$, $15\sigma_c$ and $10\sigma_c$. At high values of $L$ we show a profile of a stable colloidal gas (full line). Upon reducing the wall-wall separation we observe the transition $\tau_{0-1}$ and we show the stable layering profile for $L = 15\sigma_c$. For this parameter the gas became metastable. When $L$ is further decreased the mixture undergoes capillary condensation as it is shown by the profile of the confined stable liquid for $L = 10\sigma_c$. Note that for all values of $L$ the full lines denote the profile of the stable state and we did not show all metastable phases at each value of $L$.

We have presented a variety of phenomena which manifest themselves in the density profiles. This has been achieved for selected state-points. From studying the

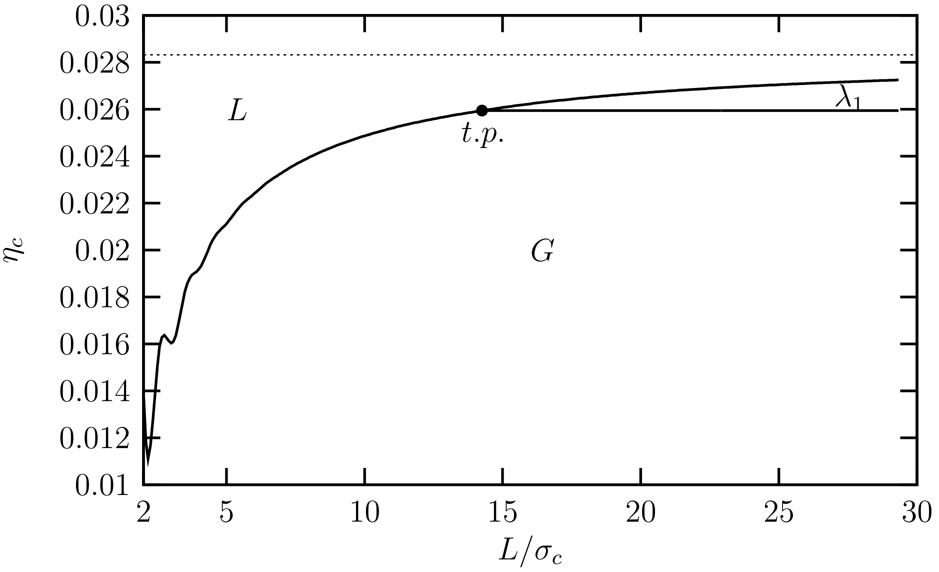

Figure 4.8: Phase diagram in the $(L, \eta_c)$-representation for a confined colloid-polymer mixture with size ratio $q = 0.6$ and fixed polymer packing fraction in the reservoir, $\eta_p^r = 0.65$. We observe three stable phases at large wall-wall separations: the gas $(G)$, the layering $(\lambda_1)$ and the liquid $(L)$ phase. Upon decreasing $L$ we find a triple point (filled circle) between these phases. At low values of $L$ the layering is metastable and we find stable gas–liquid coexistence.

grand potential $\Omega$ within the minimization procedure of DFT in a wide range of slit-widths $L$ and colloid packing fractions $\eta_c$, we are able to evaluate the phase diagram of the confined AOV mixture in the $(L, \eta_c)$-representation. Figure 4.8 shows the result. We observe three regimes which we denote the colloidal gas (G), the layering $(\lambda_1)$ and the liquid $(L)$ phase. The full lines show the lines between two coexisting phases. The bulk fluid–fluid coexistence is indicated by the dotted line. At high values of $L$ we find three stable regimes — compare these results to a trajectory with fixed $\eta_p^r = 0.65$ in the surface phase diagram in Fig. 4.2(a). Below the triple point (*t.p.*) the layering $\lambda_1$ becomes metastable and only the gas–liquid coexistence remains. The coexistence lines display power law and exponential dependence on $L$ as described above, little of the latter is visible for large $L$ and the gas–layering coexistence line is almost described by a straight line. At low values of $L$ the gas–liquid coexistence displays strong correlation effects which also manifest themselves in the oscillations of one curve.

## 4.2 Competition between layering and capillary condensation

### 4.2.1 Influence of confinement on the coexistence lines

We highlight the competition between the layering transition and capillary condensation by studying the shift of corresponding state-points of coexistence due to confinement in more detail. As we already pointed out, we expect an exponential shift of the gas–layering coexistence state-point, i.e., points where $\Omega_{\lambda_1} = \Omega_g$. In Fig. 4.9 we show the shift $\log|\eta_c^{lay} - \eta_{c,wall}^{lay}|$ of the layering point as a function of the slit width $L$. In the logarithmic representation we find a straight line for the shift (full line) in accordance with the prediction. The fit (dashed line) serves as guide to the eye. Moreover, from the fit we can extract the inverse decay length $\xi \approx 2.5\sigma_c/2$. This is in good agreement with the inverse decay length $a_0 \approx 2.4\sigma_c/2$ which describes the exponential monotonic decay of structural properties for state-points in the same region of the phase diagram. Note that we show results for small widths $L$ which denote a branch of the coexistence line that lies in the metastable regime (cf. Fig. 4.8). Due to the exponential decay we cannot resolve the decay at values of $L$ above the triple point for the chosen parameters. Our observation shows that in the region where the gas–layering transition is stable the value of $\eta_c$ is only weakly dependent on $L$; see the regime for $L$ above the triple point in Fig. 4.8 where the coexistence line is almost horizontal. As mentioned above we find that the exponential behavior for the layering is similar to that for the behavior of the pre-wetting line in confined geometry.

In Fig. 4.10 we display the shift of the capillary condensation as compared to the bulk fluid–fluid binodal, $\eta_{c,bulk}^{cond} - \eta_c^{cond}$. Depending on the slit width we can observe transitions from the gas phase or from the layering to the confined liquid phase. Figure 4.10 shows those lines upside down and shifted vertically as compared to the phase diagram Fig. 4.8. The gas–liquid coexistence (full line) and the layering–liquid coexistence (dashed line) are well described by the power law behavior indicated by the fitted lines (dotted and dash-dotted line). In Figs. 4.11 and 4.12 the power law behavior of the shift of the liquid–gas coexistence line is more clearly visible when we plot $\delta\eta_c$ vs. $1/L$ or $L$ vs. $1/\delta\eta_c$, respectively. We find good agreement with the prediction from Eq. (4.7) above.

The present results show the behavior for values along a horizontal line in the bulk phase diagram with $\eta_p^r = 0.65$. This value has been chosen since on the one hand the layering line and the (bulk) fluid–fluid binodal are sufficiently separate, and, on the other hand, we are far away from the layering critical point. For higher values of

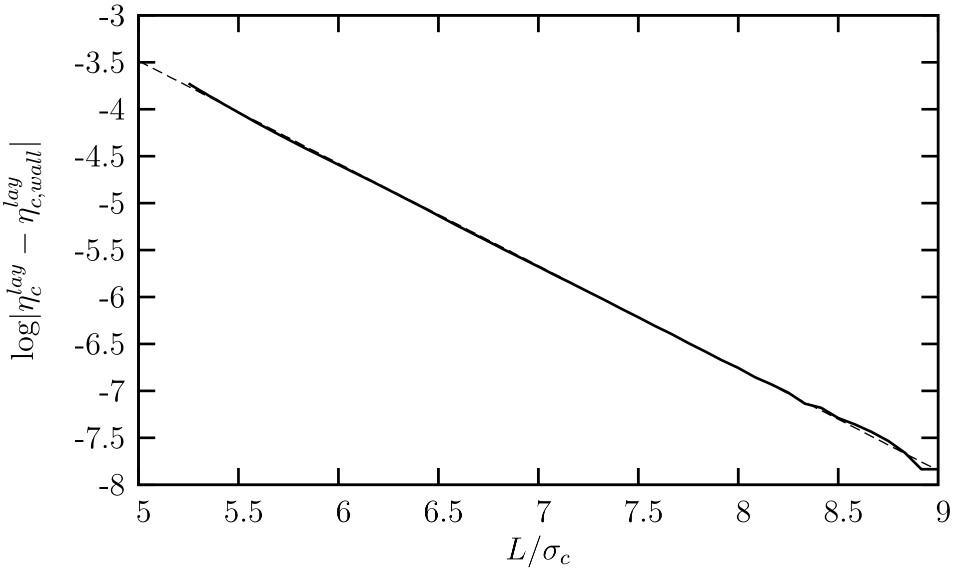

Figure 4.9: Exponential shift of the layering line $\eta_c^{lay}$ for the confined fluid with $q = 0.6$ and $\eta_p^r = 0.65$. In the logarithmic representation $\log|\eta_c^{lay} - \eta_{c,wall}^{lay}|$ we find linear behavior in the whole range (full line) in which the gas–layering transition can be found for these parameters. The dashed line is a linear fit and serves as guide to the eye. Due to the exponential behavior it is difficult to resolve the shift of the layering line for wall-wall separations $L > 9\sigma_c$.

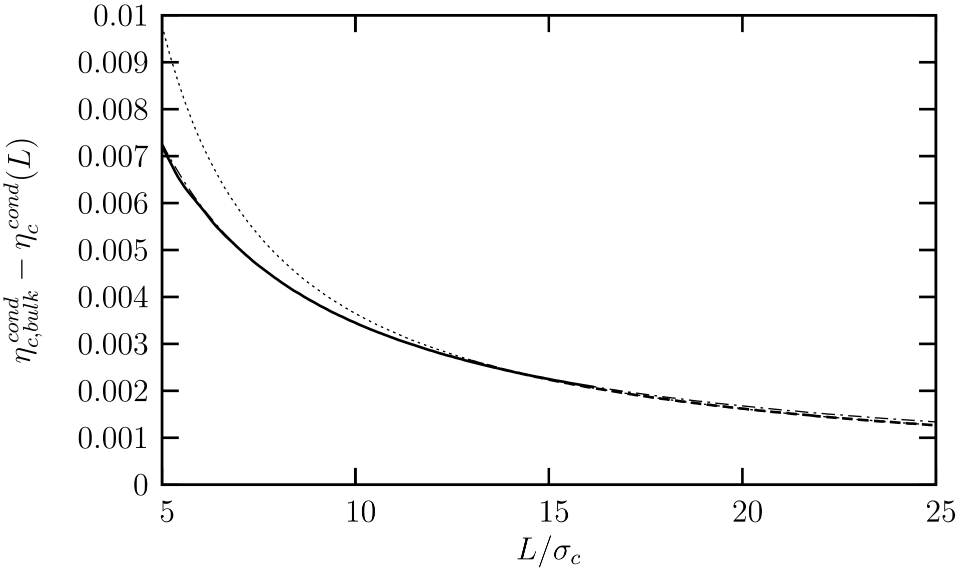

Figure 4.10: Shift $\delta\eta_c = \eta_{c,bulk}^{cond} - \eta_c^{cond}(L)$ of the gas–liquid (full line) and the layering–liquid (dashed line) coexistence. The dotted and the dash-dotted lines are guide to the eye and each line results from the fit $\delta\eta_c = \bar{b}/(L + \bar{c})$. We find clear agreement.

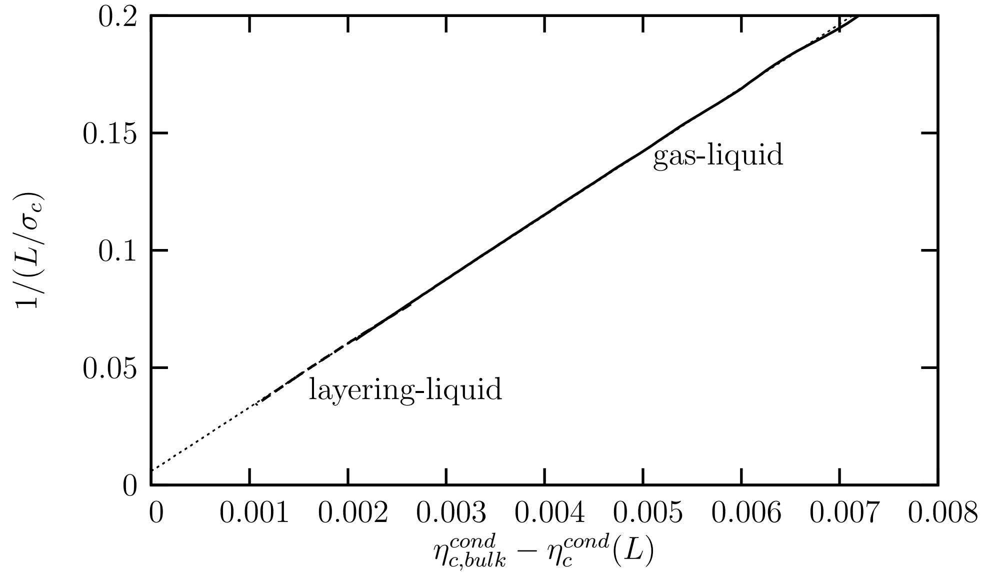

Figure 4.11: Power law behavior of the shift $\delta\eta_c = \eta_{c,bulk}^{cond} - \eta_c^{cond}(L)$ of the gas–liquid (full line) and the layering–liquid (dashed line) coexistence for the confined fluid with $q = 0.6$ and $\eta_p^r = 0.65$. Both lines are in good agreement with the linear fit (dotted line) to $1/L = (\delta\eta_c + c)/b$.

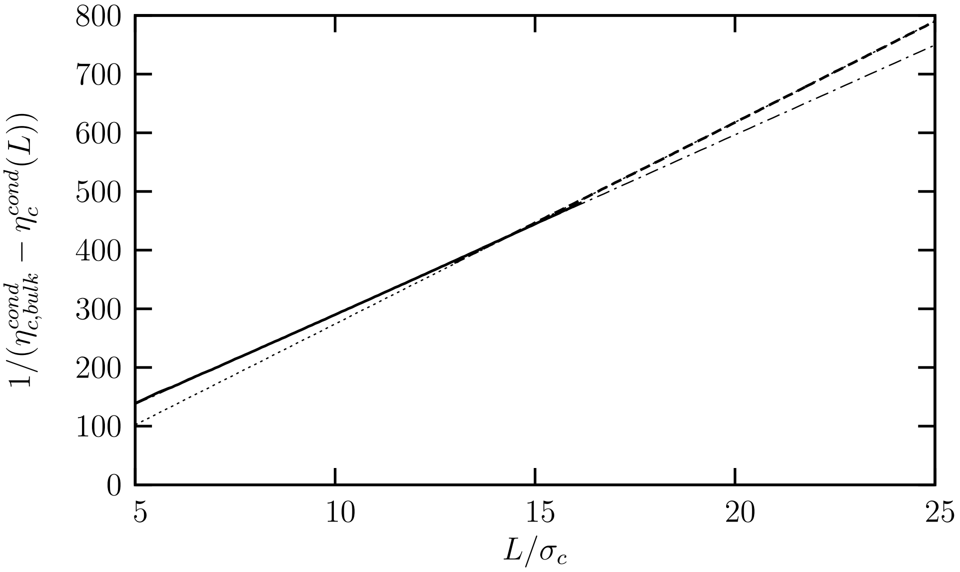

Figure 4.12: Power law behavior of the shift $\delta\eta_c = \eta_{c,bulk}^{cond} - \eta_c^{cond}(L)$ of the gas–liquid (full line) and the layering–liquid (dashed line) coexistence. The dashed and the dash-dotted lines show a linear fit to the data with $1/(\delta\eta_c) = (L + \tilde{c})/\tilde{b}$.

the polymer packing fraction $\eta_p^r$ in reservoir we find a narrow layering region and the triple point (*t.p.*) in the $(L, \eta_c)$ phase diagram (cf. Fig. 4.8) moves to larger values of $L$. Analogously, for decreasing $\eta_p^r$ the triple point moves to smaller values of $L$. When plotted in the $(\eta_c, \eta_p^r)$ phase diagram one finds that the trajectory of the triple points is close to the layering line $\tau_{0-1}$. The reason for this result is the exponential behavior of the shift of the layering line (cf. Fig. 4.2). Below the layering critical point at a single wall the gas–layering coexistence line also disappears in the slit geometry.

### 4.2.2 Stable vs. metastable phases

The phase diagram in Fig. 4.8 shows the coexistence lines between the three phases, namely the gas, the layering, and the liquid. The density profiles in Figs. 4.6 and 4.7 reveal that the full phase diagram which includes a metastable regime and spinodal lines is complex. We obtained the coexistence lines from demanding the equality of the grand potential of the two phases. The metastable regime is obtained from studying the adsorption isotherms. Figure 4.13 shows the result for fixed $L = 15.5\sigma_c$ and varying colloid packing fraction $\eta_c$. At low values of $\eta_c$ we find low excess colloid adsorption $\Gamma_c$ which corresponds to the gas phase. At high values of $\eta_c$ we find high excess adorption of the colloids in the pore which reflects the filled liquid pore. In between, the system undergoes phase transitions. The parameters are chosen such that three stable phases occur and two transitions take place. When following the gas branch of the adsorption isotherm at the value $\eta_c \approx 0.025941$ we observe the transition $\tau_{0-1}$ from gas to layering. Slightly above, at $\eta_c \approx 0.02616$, the mixture undergoes the second transition from layering to liquid. The gas–liquid transition at $\eta_c^* \approx 0.02614$ is in the metastable regime w.r.t. layering.

As it is displayed in Fig. 4.13 we find metastable regions of each phase which are bounded by the dashed vertical lines. These endpoints for various values of $L$ and $\eta_c$ denote the spinodal lines. In Fig. 4.14 we show the whole phase diagram for the colloid-polymer mixture in the slit geometry. Coexistence lines between two phases are displayed by the full lines. As compared to the result in Fig. 4.8 we see the gas–layering coexistence in the full range $L > 5.25\sigma_c$. In the vicinity of the triple point the gas–liquid and the layering–liquid coexistence almost coincide and can hardly be distinguished. The dashed and the dash-dotted lines display the spinodal regions. The gas phase is stable for values of $\eta_c$ below the top dashed curve (at $\eta_c \approx 0.02624$ for $L > 8\sigma_c$) and we can observe the liquid phase for $\eta_c$ above the bottom dashed curve (at $\eta_c \approx 0.0148$ for large values of $L$). The dash-dotted lines bound the regime in which layering can occur, but only in the region above the triple point we find stable layering.

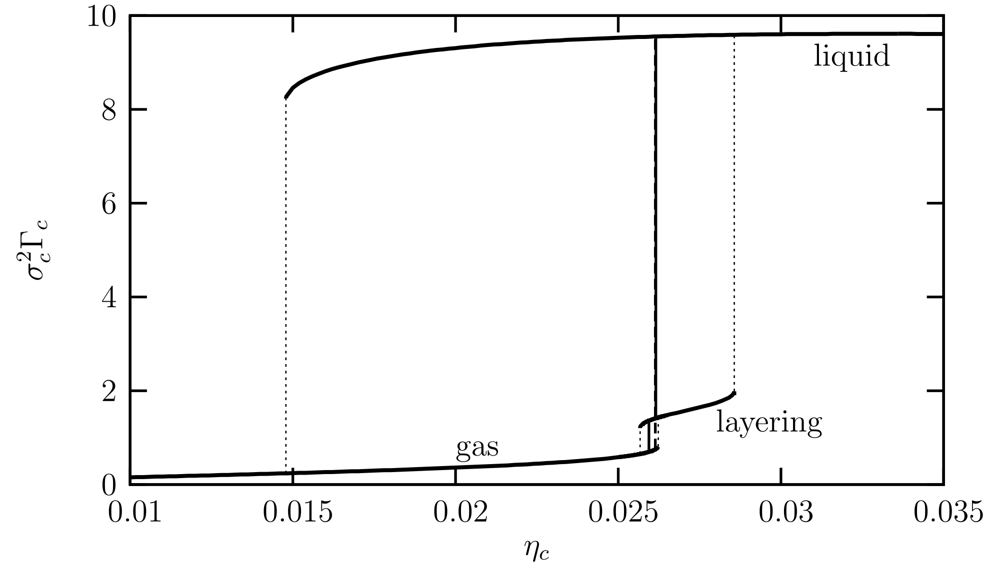

Figure 4.13: Colloid excess adsorption $\Gamma_c$ in a slit pore. The wall-wall separation $L = 15.5\sigma_c$ and the polymer packing $\eta_p^r = 0.65$ are fixed. Upon varying the colloid packing fraction $\eta_c$ we find stable regimes of the gas, the layering and the liquid phase. The transitions between the stable states, i.e., the gas–layering and the layering–liquid transitions, are shown by full vertical lines. The (gas–liquid) transition between metastable states is shown by the dashed vertical line. At the endpoints of each branch of the adsorption isotherm the spinodal is indicated by the dotted vertical lines.

We highlight the region in the vicinity of the triple point to figure out the behavior of the coexistence lines around this point (see Fig. 4.15). The full (almost) horizontal line at $\eta_c \approx 0.025941$ shows the gas–layering coexistence. The full line at low values of $L$, which ends at the upper dashed line, is the gas–liquid binodal and the full line at high $L$, which ends at the bottom dash-dotted line, shows the layering–liquid coexistence. In this figure we clearly see the three distinct lines.

### Fixed slit width $L$

The competition between different phases close to phase transitions manifests itself in thermodynamic quantities. We study the surface tension $\gamma$ to determine the state-points of coexistence and the excess colloid adsorption $\Gamma_c$ to obtain in addition the spinodal regions. We show both quantities in Fig. 4.16(a) and (b), respectively. The slit width is $L = 15.5\sigma_c$ and we observe three stable phases. Note that (a) shows a part of the gas–layering transition regime from Fig. 4.13. The three vertical dashed lines show the three transitions of which those with the lowest value of $\eta_c$ and the highest value of $\eta_c$ describe transitions between stable phases. Figure 4.16(b) clarifies this result as we find three branches of the surface tension $\gamma$ corresponding to the

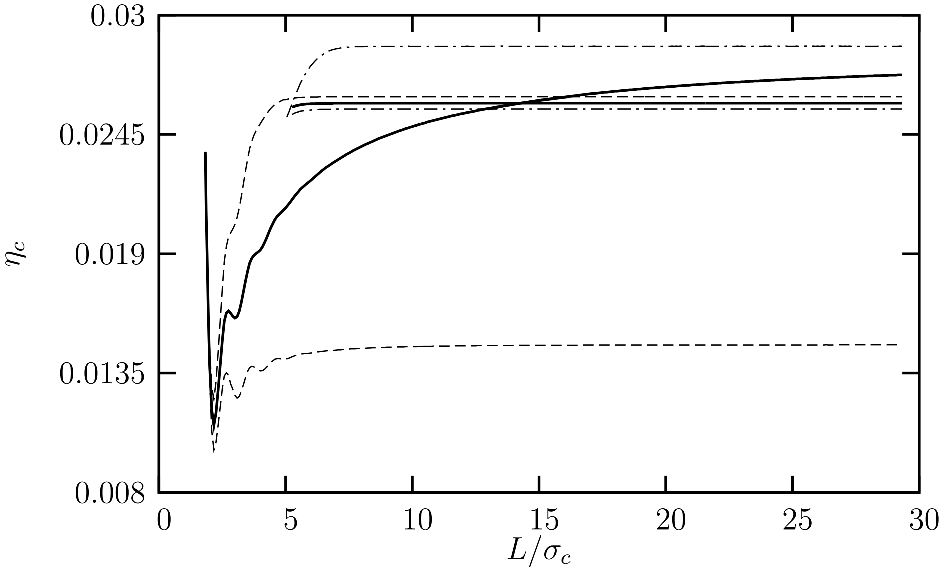

Figure 4.14: Phase diagram in the $(L, \eta_c)$-representation for a confined *cp* mixture for the same system as discussed in Fig. 4.8. Besides the coexistence lines (full lines) we show the spinodal regions. The gas–liquid, the gas–layering and the layering–liquid coexistence are shown over the whole range — see Fig. 4.8 for the stable part of each line. The dash-dotted lines show the layering spinodal. Below the dashed line at low values of $\eta_c$ the liquid is unstable, above the dashed line at high values of $\eta_c$ the gas is unstable.

different phases. However, for a given value of $\eta_c$ the phase with the lowest value of $\gamma$ is stable. At low $\eta_c$ the gas phase takes the lowest value and is stable. Upon increasing $\eta_c$ up to the first dashed vertical line we find a gas–layering transition. Above $\eta_p^r \approx 0.025941$ the branch corresponding to layering takes the lowest values until the intersection point with the line corresponding to the liquid phase. From that figure we can infer in which regions one or two additional metastable phases and further transitions occur.

For a series of slit widths $L/\sigma_c \in [12, 17]$ we show the surface tensions for the three different phases [Fig. 4.17(a)-(g)]. For narrow slits, $L = 12\sigma_c$, only the gas and the liquid phase are stable, at high values of $\eta_c$ we observe a broad range in which the layering phase is stable. In between, at $L = 14.25\sigma_c$ we find that the three branches intersect in a single point, the triple point. The vertical lines indicate the state-point with lowest value of $\eta_c$ for layering, the intersection point between the gas and the layering branch, and the state-point with highest value of $\eta_c$ for the gas phase.

### Fixed state-point

It is instructive to study variable slit width $L$ as it is easier in experiment to control

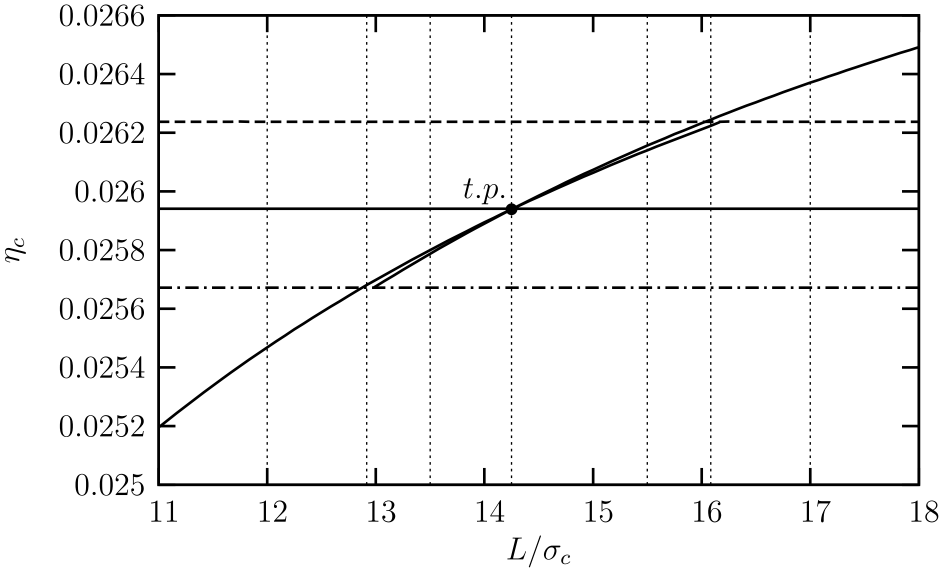

Figure 4.15: Phase diagram for a confined *cp* mixture in the vicinity of the triple point (t.p.). The full lines show the two-phase coexistence lines which intersect at the triple point where the gas, the layering and the liquid phase can coexist. The dashed horizontal line displays the gas spinodal and the dash-dotted horizontal line displays the layering spinodal. The values of $L$ chosen in Fig. 4.17 are illustrated by the vertical lines.

this property than the state-point. From the $(L, \eta_c)$ phase diagram we know that the gas–layering coexistence $\tau_{0-1}$ line is almost horizontal for large values of $L$, and therefore, one has to choose a state-point in the vicinity of this line to observe a transition triggered by varying slit width. We select three values of the colloid packing fraction $\eta_c$: 0.0257, 0.025941, and 0.0262. Only the intermediate value is sufficiently close to the transition line $\tau_{0-1}$. In Fig. 4.18(a) we show the difference in the grand potentials $\Omega^g - \Omega^l$ and $\Omega^{\lambda_1} - \Omega^l$. For negative values of the difference in the grand potential we find stable gas $g$ or layering state $\lambda_1$, respectively. For $\eta_c = 0.0257$ and $\eta_c = 0.0262$ we observe for values of $L$ above the point of capillary condensation one stable phase, i.e., the gas or the layering. For $\eta_c = 0.025941$, which is close to the transition $\tau_{0-1}$, the lines corresponding to gas and layering almost coincide and can hardly be distinguished. The difference increases at low values of $L$ which is, however, in the metastable regime w.r.t. the liquid. The vertical lines display the location of the transitions. In the inset we display the region where the gas and the layering become unstable. Note that the oscillations originate from the contribution of the liquid.

In Fig. 4.18(b) at high and intermediate wall-wall separations $L$ we observe that the colloid excess adsorption is basically constant. This means that the adsorption

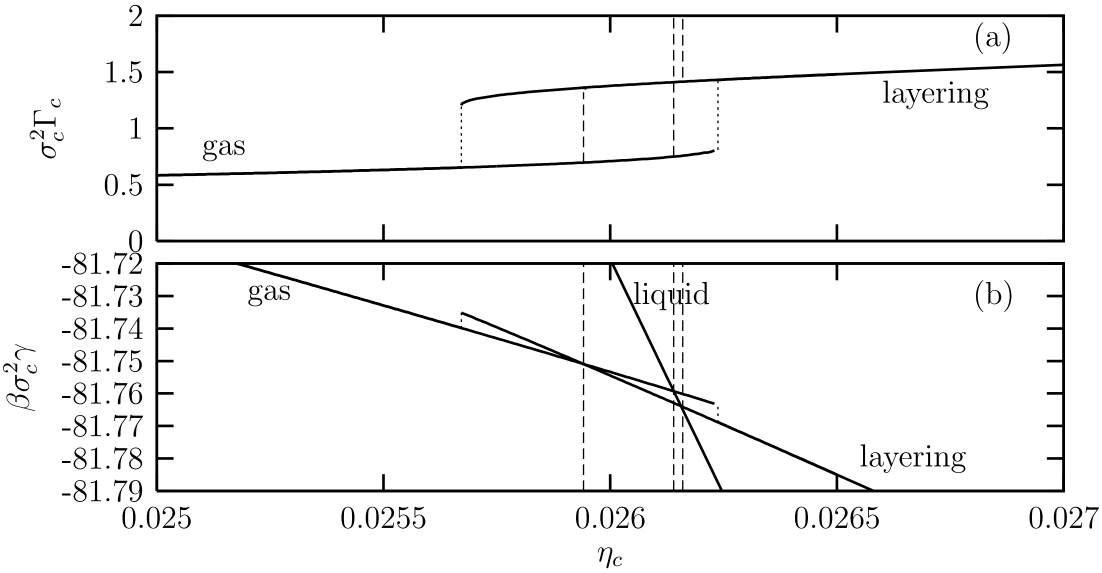

Figure 4.16: (a) Colloid adsorption $\Gamma_c$ in a slit-like pore for the same parameters as in Fig. 4.13, $L = 15.5\sigma_c$. The region where the gas–layering transition takes place is enlarged. The dotted vertical lines indicate the layering spinodal and the gas spinodal at low and high $\eta_c$, respectively. The dashed lines indicate the transitions between the three phases. (b) Shown are the corresponding surface tensions. The three full lines correspond to the gas, the layering and the liquid phase. Clearly, for the chosen parameters we find three intersection points which correspond to the three possible transitions: gas–layering, layering–liquid and gas–liquid. In this case the latter is in the metastable regime while the former two are stable.

originates from the two independent separate walls. The locations of the transitions are indicated by the arrows. Only for small $L$, i.e., in the metastable regime, we find an increase in the adsorption by roughly 10%. In contrast to the gas and the layering phase we see that the adsorption of the liquid is linear in $L$. This can be explained by the fact that for capillary condensation the pore is completely filled with the colloidal liquid. Deviations occur at small widths $L$.

### Further layering transitions

Above we have discussed results for the layering transition $\tau_{0-1}$. As already pointed out in Sec. 4.1.2 and Fig. 4.2(b) one finds layering states with more than one liquid layer adsorbed at the wall [22]. We confirmed such states for the White Bear version of FMT. As for increasing number of layers the layering lines in the $(\eta_c, \eta_p^r)$ phase diagram are very close to the bulk fluid–fluid binodal it follows that the triple point between gas, layering $(\lambda_{i>1})$ and liquid is in a region where $L$ is very large. Moreover, it is demanding to consider further layering states and to figure out the full $(L, \eta_c)$

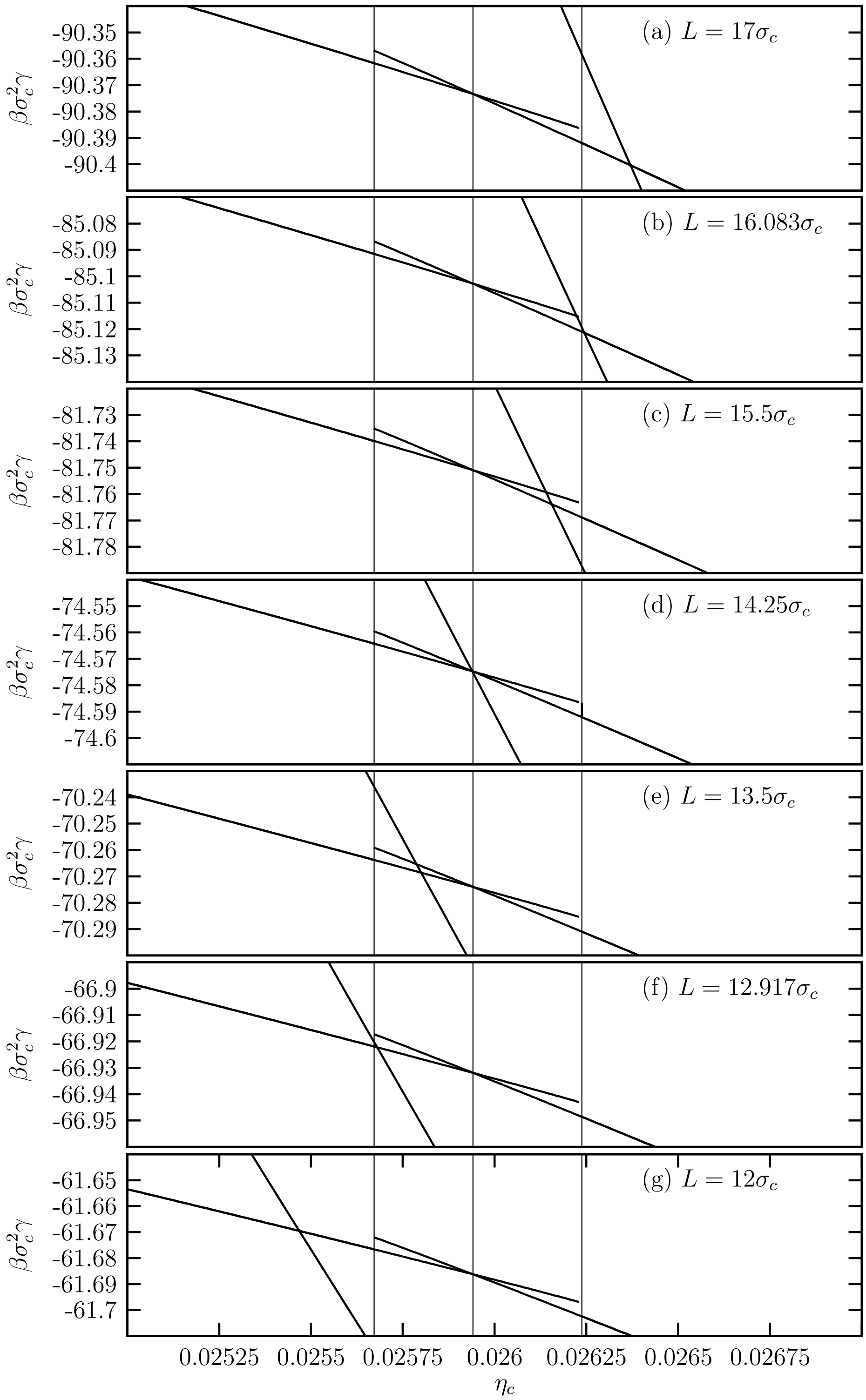

Figure 4.17: Surface tensions $\gamma$ of the colloid-polymer mixture confined between two walls at selected wall-wall separations $L/\sigma_c \in [12, 17]$. For large separation ($L = 17\sigma_c$) we find three stable phases bounded by the intersection points of the three branches of $\gamma$: the gas, the layering and the liquid phase. For small separations ($L = 12\sigma_c$) we find two stable phases (gas and liquid) as layering is metastable w.r.t. condensation. At intermediate values of $L$ the competition between the three phases implies complex behavior (see text). For the value $L = 14.25\sigma_c$ we see the intersection between three lines at the triple point.

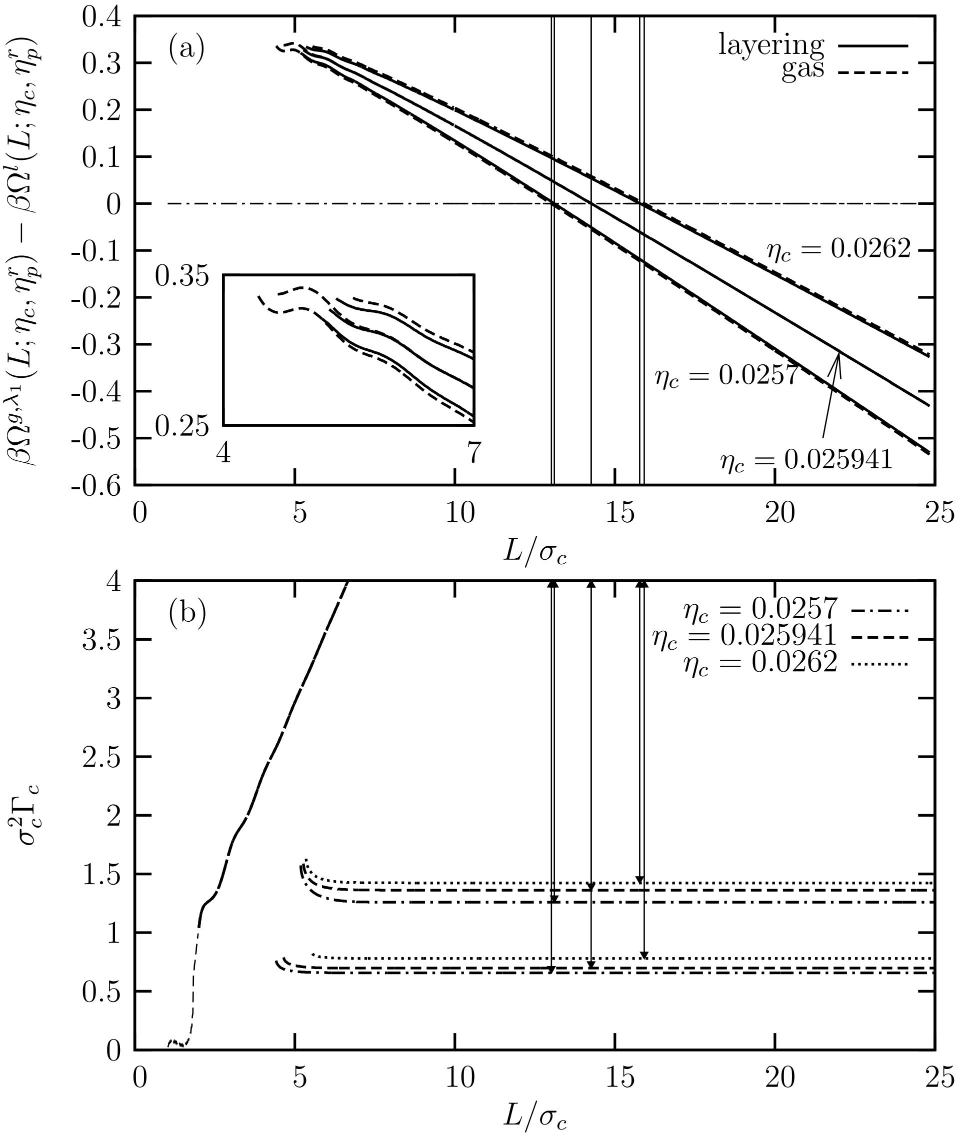

Figure 4.18: Grand potential $\Omega$ and colloid excess adsorption $\Gamma_c$ of a colloid-polymer mixture confined between two parallel walls. The size ratio $q = 0.6$ and the state-point is fixed. We show the results for three different values of $\eta_c$ and fixed $\eta_p^r = 0.65$. For $\eta_c = 0.0257$ the gas phase is stable, for $\eta_c = 0.0262$ we find stable layering behavior. At the intermediate value $\eta_c \approx 0.025941$ we are in the gas–layering coexistence regime. In (a) we show the difference between the grand potentials of the layering and the liquid phase, $\Omega^{\lambda_1} - \Omega^l$, and of the gas and the liquid phase, $\Omega^g - \Omega^l$, respectively. For $\eta_c = 0.0257$ we find a stable gas phase above the transition at $L^* \approx 13.0\sigma_c$; for $\eta_c = 0.0262$ we observe stable layering above $L^* \approx 15.8\sigma_c$. At $\eta_c \approx 0.025941$ the branch for the gas and the layering almost coincide in this representation. In (b) we show the corresponding colloid adsorptions. The lines at $\sigma_c^2\Gamma_c \approx 0.7$ result for the gas phase, those at $\sigma_c^2\Gamma_c \approx 1.3$ correspond to the layering state $\lambda_1$. The lines with (almost) linear behavior correspond to capillary condensation. The transitions are indicated by the arrows. Note that for stability considerations one has to confer to (a).

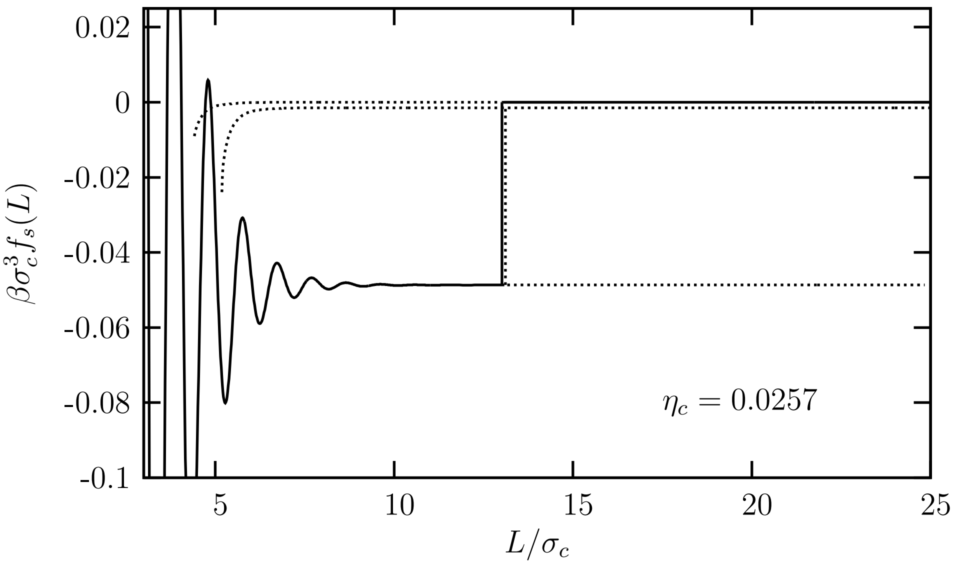

Figure 4.19: Solvation force $f_s$ between two planar hard walls which confine a colloid-polymer mixture with size ratio $q = 0.6$ and $\eta_p^r = 0.65$. The state-point is chosen such that for large $L$ the gas phase is stable (full line). $\eta_c = 0.0257$ which is slightly below the gas–layering coexistence line. Upon decreasing the wall-wall separation we find a transition to the liquid phase shown by the vertical full line. Below that value of $L$ the liquid phase is stable (full line). The transition between the layering and the liquid phase is indicated by the vertical dotted line. However, the layering is metastable in the whole range (middle dotted line).

phase diagram because many metastable regimes can overlap. We have confirmed that similar behavior to that presented above for $\lambda_1$ can be found for $\lambda_2$. However, studying the first layering transition already provides the relevant insights.

## 4.3 Solvation forces

### 4.3.1 Effect of solvent phase separation

The adsorption in the slit-like pore is closely related to the force between the two confining walls. We study the solvation force for the AOV mixture and, in particular, we focus on its complex behavior due to the rich phase behavior of the confined fluid. In the slit an infinitesimal variation of the grand potential has the following form

$$\mathrm{d}\Omega = -p\mathrm{d}V - S\mathrm{d}T - \sum_{i=c,p} N_i \mathrm{d}\mu_i + 2\gamma\mathrm{d}A - Af_s\mathrm{d}L. \tag{4.8}$$

The last term describes the variation due to variations of the slit-width and the force $Af_s$ describes the following interactions: the wall-wall, the wall-fluid, and the fluid–

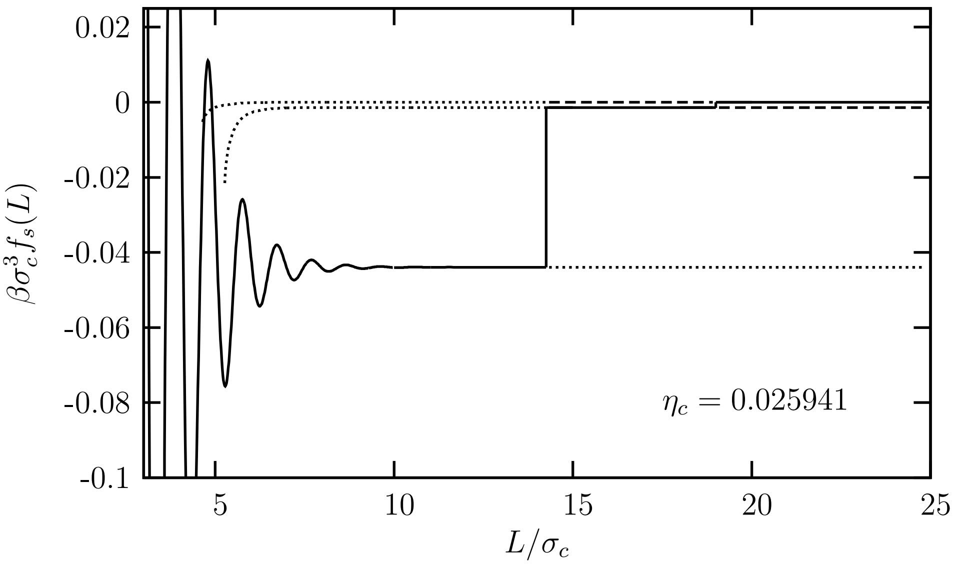

Figure 4.20: Solvation force $f_s$ between two planar hard walls confining a *cp* mixture. The size ratio $q = 0.6$ and $\eta_p^r = 0.65$. The colloid packing fraction is chosen such that the state-point lies on the gas–layering coexistence line, $\eta_c \approx 0.025941$. Due to the exponential dependence of the shift of the layering line on $L$ only a small variation $\delta\eta_c$ suffices to result in a state-point below or above the coexistence line. As we cannot resolve the exponential behavior for the wall-wall separation above the triple point we find for $\eta_c \approx 0.025941$ a transition between the gas phase and the layering state. This finding is indicated by the dashed lines and the short full vertical line. At small $L$ we observe capillary condensation (full vertical line) and a stable liquid phase.

fluid interactions. The effect of the latter two contributions is called the *solvation force*. In these terms $f_s$ denotes a surface excess pressure and is given by

$$f_s = -\frac{1}{A}\left(\frac{\partial\Omega}{\partial L}\right)_{\mu_i,T,A} - \, p^{bulk}. \tag{4.9}$$

To obtain a directly measurable expression for $f_s$, we use the following relation

$$-\frac{1}{A}\left(\frac{\partial\Omega}{\partial L}\right)_{\mu_i,T,A} = -\int \mathrm{d}V \frac{\delta\Omega}{\delta(\mu - V_{ext}(\mathbf{r}))}\frac{\partial V_{ext}(\mathbf{r})}{\partial L}, \tag{4.10}$$

where $\delta\Omega/\delta((\mu - V_{ext}(\mathbf{r})) = -\rho(\mathbf{r})$. For planar hard walls this reduces to [108]

$$\beta f_s(L) = \sum_{i=c,p}[\rho_{i,L}(0^+) - \rho_{i,\infty}(0^+)]. \tag{4.11}$$

From the contact values $\rho_{i,L}(0^+)$ and $\rho_{i,\infty}(0^+)$ of each component of the AOV mixture at finite $L$ and $L \to \infty$, respectively, we can evaluate the solvation force.

In Figs. 4.19, 4.20 and 4.21 we show the solvation force $Af_s$ for three different state-points $\eta_c = 0.0257$, 0.025941, and 0.0262. The polymer packing fraction in the

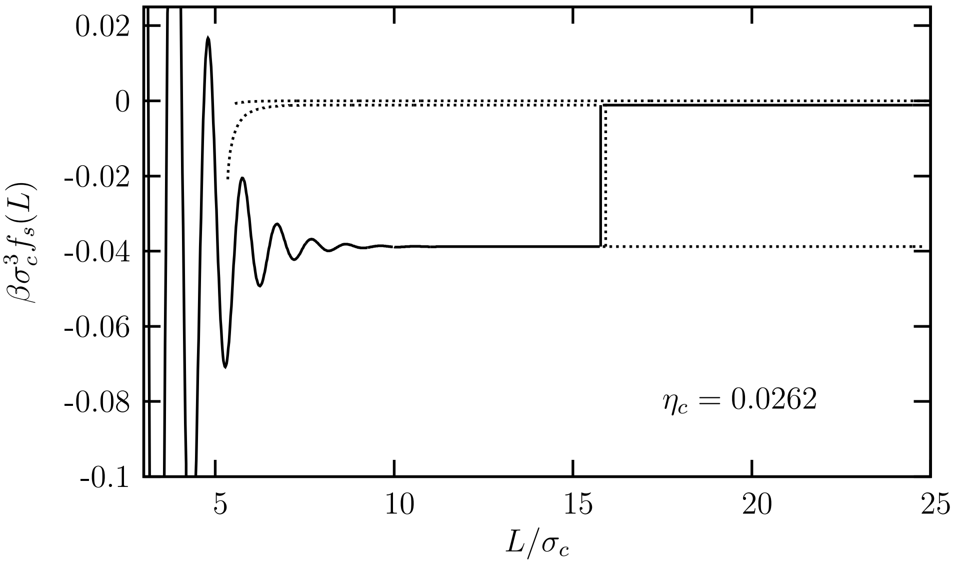

Figure 4.21: For $q = 0.6$, $\eta_p^r = 0.65$, and $\eta_c = 0.0262$ we find a jump in the solvation force $f_s$ due to the transition from layering to liquid (full vertical line). Above that value the layering is stable (full line), below we observe capillary condensation (full line). The dotted lines display the metastable regimes. The dotted vertical line shows the position of the transition from gas to liquid, which for the chosen parameters corresponds to a transition between metastable states.

reservoir $\eta_p^r = 0.65$ and the size ratio $q = 0.6$. We show the solvation force $f_s(L)$ in the range $L/\sigma_c \in [3, 25]$. For the value $\eta_c = 0.0257$ we find two regimes of $f_s$. For large slit widths we observe a low and almost constant value of the solvation force $Af_s$ (full line). This is in accordance with the observation of the exponential decay of structural properties in this region of the phase diagram that manifests in the density profiles and depletion potentials in the AOV mixture. Upon decreasing the value of $L$ we find a jump in the solvation force at $L = 13.02\sigma_c$ (full vertical line) arising from capillary condensation (see the phase diagram in Fig. 4.15). At the slightly larger value $L = 13.11\sigma_c$ we indicate the transition between the (metastable) layering and the liquid by the dotted vertical line. Further decreasing of the wall-wall separation $L$ leads to pronounced oscillations in the solvation force due to the filled pore. The wavelength of the oscillations is similar to the size of the colloids, $\sigma_c$.

For the largest value, $\eta_c = 0.0262$, similar behavior occurs. However, at large slit widths we find stable layering (see the phase diagram Fig. 4.15) and the solvation force follows the full line which takes larger absolute values than for the corresponding gas phase. In a similar fashion we observe a transition to the liquid at $L = 15.78\sigma_c$, while the transition between the stable liquid and the metastable gas occurs at the slightly larger value $L = 15.92\sigma_c$. At small $L$ the behavior on the liquid branch is very similar to the case of lower $\eta_c = 0.0257$.

We find a competition between the layering and gas phases for $\eta_c \approx 0.025941$, i.e., at a state-point which is very close to the gas–layering coexistence. At high values of $L$ only a tiny variation suffices to trigger the transition from gas to a layering state. We indicated the transition by the short full line for an exemplary value $L = 19\sigma_c$. Below this point the layering is stable until we decrease $L$ below $14.25\sigma_c$ where condensation occurs and the liquid fills the pore. This regime is similar to the cases discussed in the previous paragraphs. Close to gas–layering coexistence we can find solvation forces which exhibit two jumps $\Delta f_s$, each related to a transition. This finding is in accordance with theoretical predictions as the jump in adsorption is adjoined by a jump in the solvation force [57, 87]. We discuss this point in the following section.

### 4.3.2 Thermodynamic relations

We have observed that at the state-points of the transitions we find a jump in the excess adsorptions which is accompanied by a jump in the solvation forces. We study a quantitative relation between $\Delta\Gamma_c$ and $\Delta f_s$ at the state-points of the gas–layering ($g$–$\lambda_1$), the layering–liquid ($\lambda_1$–$l$) and the gas–liquid ($g$–$l$) coexistence. Moreover, we investigate whether at the transitions we find different types of dependence of $\Delta f_s$ on the slit-width $L$ in a similar fashion to the shift of the coexistence lines due to confinement where we observed qualitatively different behavior (see Figs. 4.9 and 4.11).

The Gibbs adsorption equation [87] for a binary mixture of colloids and polymer is given by

$$\mathrm{d}\Omega = 2A\mathrm{d}\gamma + 2As\mathrm{d}T + A\sum_{i=c,p}\Gamma_i\mathrm{d}\mu_i + 2\gamma\mathrm{d}A - (Af_s)\mathrm{d}L \tag{4.12}$$

which is appropriate for our situation. In the following we recall some arguments from Ref. [87]. The surface area of the walls $A$ is fixed. From the Gibbs-Duhem equation $\sum_{i=c,p}\rho_i^{bulk}\mathrm{d}\mu_i = 0$ at constant pressure $p$ and temperature $T$ we can eliminate $\mathrm{d}\mu_p$ and obtain $2\mathrm{d}\gamma + \Gamma_c^r\mathrm{d}\mu_c + f_s\mathrm{d}L = 0$ [109]. The relative colloids adsorption w.r.t. the polymer is defined as $\Gamma_{c,\alpha}^r = \Gamma_{c,\alpha} - \Gamma_{p,\alpha}\rho_c^{bulk}/\rho_p^{bulk}$. At coexistence and by equating $\gamma$ for the two phases $\alpha$ and $\beta$ one obtains

$$(\Gamma_{c,\alpha}^r - \Gamma_{c,\beta}^r)\mathrm{d}\mu_c + (f_{s,\alpha} - f_{s,\beta})\mathrm{d}L = 0. \tag{4.13}$$

At fixed pressure and fixed temperature the Clapeyron relation in terms of the difference in the adsorption and the difference in the solvation force reads

$$\left.\frac{\partial L}{\partial \mu_c}\right|_{T,p} = -\frac{\Gamma_{c,\alpha}^r - \Gamma_{c,\beta}^r}{f_\alpha - f_\beta}. \tag{4.14}$$

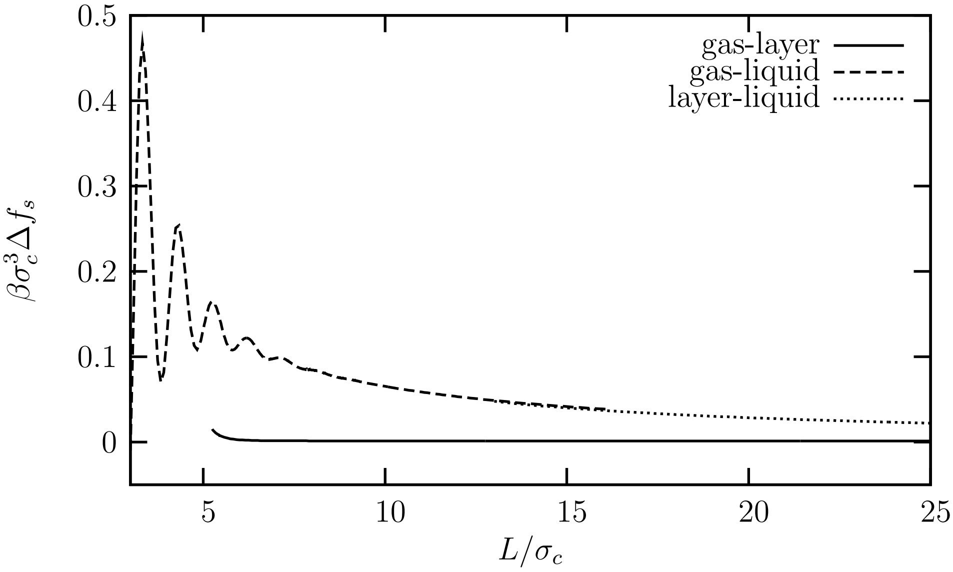

Figure 4.22: Jump in the solvation force $\Delta f_s$ between two walls which confine a *cp* mixture for state-points along the coexistence lines. We show the result for the three possible lines allowing to compare the order of magnitude between the results corresponding to the different transitions. At state-points along the gas–layer coexistence line we find exponential decay with increasing $L$ (full line). For the gas–liquid coexistence line we find oscillatory power law decay (dashed line) while along the layer–liquid coexistence line we observe monotonic power law behavior of $\Delta f_s$ (dotted line).

With the considerations exposed in 4.1.3 by use of Young's equation $\gamma_{wg} = \gamma_{wl} + \gamma_{gl}\cos\Theta$ we obtain, in terms of a general expression for two coexisting phases $\alpha$ and $\beta$, $(2\gamma_{\alpha\beta}\cos\theta)/L = \Delta\mu_c(\rho_{c,\alpha} - \rho_{c,\beta}\rho_{p,\alpha}/\rho_{p,\beta})$. Then, for the difference in the (relative) adsorption and the difference in the solvation force between coexisting phases $\alpha$ and $\beta$ follows that $\Gamma^r_{c,\alpha} - \Gamma^r_{c,\beta} \sim L(\rho_{c,\alpha} - \rho_{c,\beta}\rho_{p,\alpha}/\rho_{p,\beta}) \propto L$ and $f_\alpha - f_\beta \sim -\Delta\mu_2(\rho_{c,\alpha} - \rho_{c,\beta}\rho_{p,\alpha}/\rho_{p,\beta}) \propto -1/L$. In our case, these arguments hold for transitions where $\alpha = l$.

In Fig. 4.22 we show the jump in the solvation force at all the transitions ($g$-$l$, $g$-$\lambda_1$, $\lambda_1$-$l$) in the whole range of $L$ where they occur. At the transitions to the liquid phase we find slower decay as compared to the result along the $g$-$\lambda_1$ coexistence line. Both results, $g$-$l$ and $\lambda_1$-$l$, are of very similar character at intermediate and large values of $L$. For small slit-widths, $L < 7.5\sigma_c$, we observe correlation induced oscillations.

We can verify the $1/L$ dependence of the jump in $\Delta f_s$ in the log-log plot. We display the result in Fig. 4.23 where we plot $\Delta f_s$ vs. $1/L$. In this representation the curves follow a line which demonstrates the power law. The region with small $L$ is on the right hand side of the plot. Note that the $1/L$ behavior follows from a macroscopic formula [87] which strictly holds only for sufficiently large values of

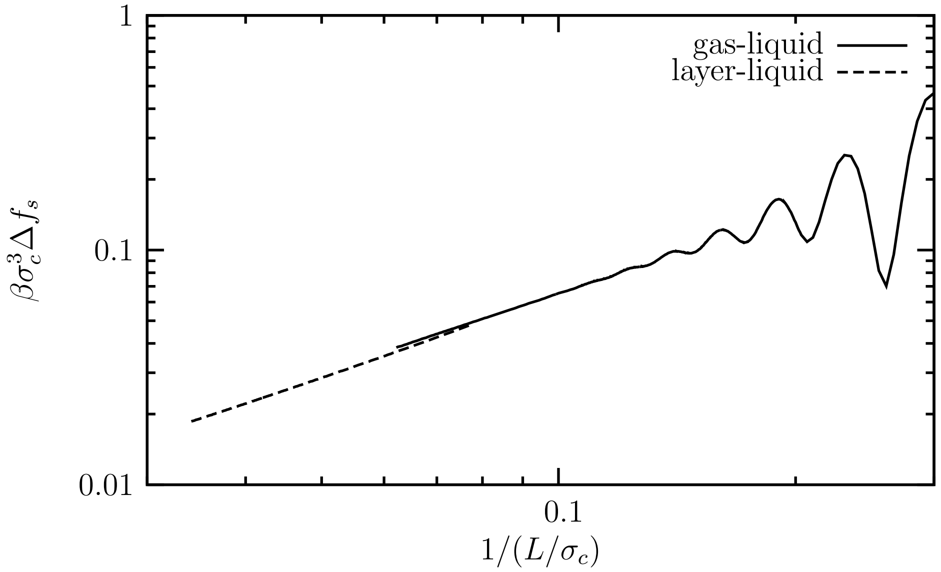

Figure 4.23: The power law behavior of the jump in the solvation force $\Delta f_s$ is captured in a wide region of state-points along the gas–liquid (full line) and the layering–liquid (dashed line) coexistence. At low values of $1/L$ we find good agreement with the power law behavior. At higher values of $1/L$, or equivalently low values of $L$, we observe the oscillatory structure in the jump of the solvation force.

$L$. In the region of small $L$ we observe deviations in the form of oscillations. It is remarkable that for both cases, the gas–liquid and the layering–liquid transition, we find similar results.

In contrast to the gas–liquid phase separation, that can occur in the bulk, the gas–layering transition is a surface phase transition. Already at one surface we find a jump in the contact values of the colloid and the polymer density profile. Note, however, that the sum of the contact densities equals the bulk pressure and does not jump. We study the behavior of the jump in $\Delta f_s$ from the contact values in slit geometry and at one single planar hard wall which, according to sum rules, equals the bulk pressure. In the logarithmic representation we show the result in Fig. 4.24. In the whole range that we can resolve ($L < 9.5\sigma_c$), we find good agreement to exponential decay of $\Delta f_s$. The exponential decay reflects the previous observations of the shift in the layering line and exhibits a comparable shift as a pre-wetting line in confined geometry. In a similar fashion to the shift in the layering line and the gas–liquid coexistence lines we find two types of decay for the present transitions.

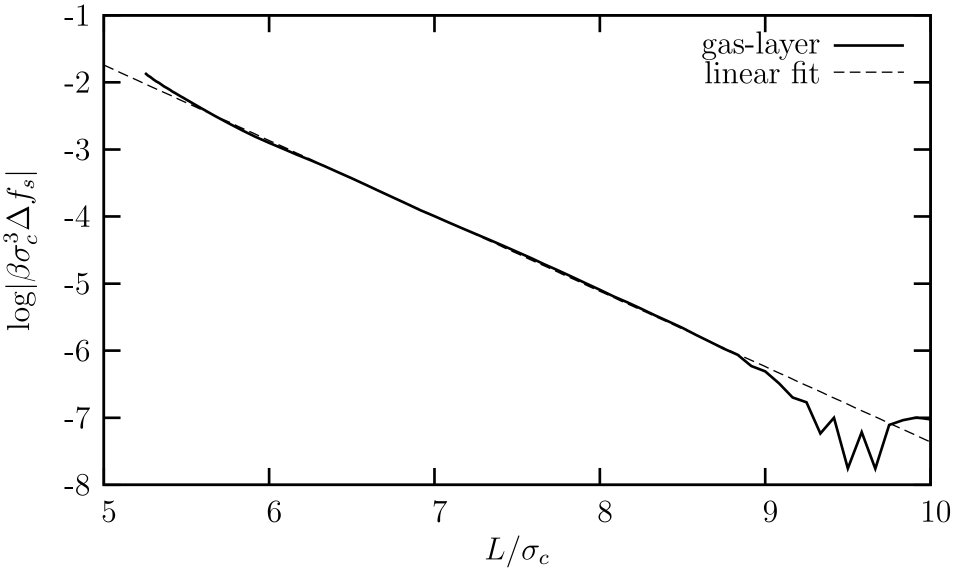

Figure 4.24: Logarithmic representation of the jump in the solvation force $\Delta f_s$ between two walls for the same parameters as in Fig. 4.22. For statepoints at gas–layering coexistence we find good agreement with the exponential behavior indicated by the fit (dashed line). Note that it is difficult to resolve the difference for wall-wall separations $L > 9.5\sigma_c$.

## 4.4 Conclusions

Within our model, the AOV mixture of colloids and polymer with its simple interaction between particles, we recover a rather complex phase behavior and a rich variety of phenomena in the bulk, at one single wall, and in confinement. On a single planar hard wall we observe layering effects. The layering transitions are robust against variation which can be due to the underlying equations of state or due to a polydisperse size distribution which can describe experimental situations more realistically than the binary colloid-polymer mixture. In confined geometry we find distinct phase transitions. Capillary condensation occurs due to a shift of the bulk fluid–fluid binodal whereas layering effects exhibit less pronounced influence. This rises the question of the competition between those two effects. When studying the dependence of thermodynamic quantities on $L$ we find qualitatively different behavior. For capillary condensation we find power law dependence for the shift of the gas–liquid coexistence and for jumps in the solvation force. At the layering line we observe exponential dependence of the same quantities on $L$. In narrow pores the capillary condensation will suppress layering effects, while those will arise for sufficiently large pores. The complexity of the phase diagram manifests in various coexistence lines and regimes of metastable phases. Results from both routes, varying $L$ or varying the state-point, may be of relevance for experimental verifications. We expect that similar competition also takes place in confined geometries which are more complex than the narrow pore, such as, for instance, porous media.

# Chapter 5

# Effective Interactions

Phase behavior, equilibrium structure, and thermodynamic properties of colloidal systems are determined by the mutual interaction between the particles of the involved species. The thermodynamics can be studied via various approaches [37,80,93,110]. For mixtures the situation is more complex than for systems with one single species of solute particles. One way to treat mixtures is to map $(n-1)$ species of a $n$-component mixture onto effective interaction potentials and reduce the complexity of the full problem to a remaining effective one-component system. This procedure can be employed in different situations, however, one has to consider the range in which the mapping is accurate or even valid, in particular, for phase separating solvents and bridging phenomena [111,112]. For ideal polymer [9,10], interacting solvent particles [113], additive [15,17,18] or non-additive hard-sphere mixtures [20,100], and systems with soft interactions [19,114] accurate mapping routes are known under certain special assumptions. For mixtures of hard spheres or the AOV mixtures when the size ratio is too symmetric, many-body interactions have to be taken into account which reduces the accuracy of the mapping. We employ a mapping procedure for the interaction between a planar hard wall and a big colloidal particle immersed in a solvent. For hard-sphere solvents or within the AO approximation, i.e., for the ideal polymer solvent, the mapping has been done successfully and provides accurate results in the region of the phase diagram where no wetting and bridging phenomena occur [18,20,22,105]. For the full mixture of colloids and polymer one inevitably has to take its phase behavior into account. We study the effective interaction between a spherical colloidal particle and a substrate with particular focus on the solvent properties.

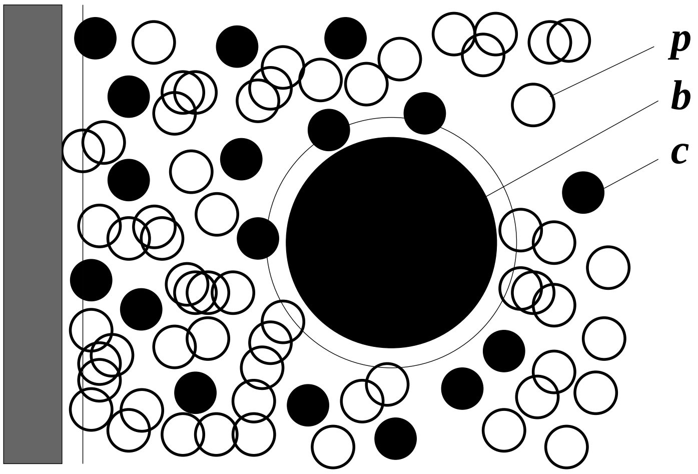

Figure 5.1: Sketch of an AOV mixture of colloids $c$ and polymer $p$ at a planar hard wall. A big colloid $b$ is immersed in the solvent. The size ratio in the sketch between the particles of the different species is $\sigma_p : \sigma_c : \sigma_b = 1 : 1 : 5$. The solvent particles consist of two species indicated by open and small filled circles. The interaction potentials among colloids are of hard-core type while the polymer may overlap freely among each other. The thin lines indicate regions not accessible to the (centers of the) smaller species $c$ and $p$.

## 5.1 Depletion potentials in colloid-polymer mixtures

In this section we study the interaction between a big colloidal particle $b$, modeled as a hard sphere, and a planar hard wall $w$. The colloid is immersed into an AOV mixture of smaller colloids $c$ and ideal polymer $p$ (see Fig. 5.1). The intrinsic interaction potential $V_{ij}(\mathbf{r}_{ij})$ of the solvent is the same as that used throughout the previous chapter and given in Eq. (2.33) for $ij = cc, cp, pc$ and $V_{pp}(\mathbf{r}_p) = 0$. In the limiting case, $\rho_c \rightarrow 0$, where the solvent is composed of ideal polymer only, the effective interaction potential between the wall and the big colloid $b$ is known exactly. For a pure hard-sphere solvent, $\rho_p \rightarrow 0$, the interaction potential can be described by accurate expressions within a general approach [18]. In the case of a solvent described by a full AOV mixture we have to treat the ternary $bcp$ mixture of colloids $b$, colloids $c$ and polymer $p$. In this case the effect of phase separation of the $cp$ mixture has to be taken into account when we address the interaction between the wall and the big colloidal particle. We may ask in which region of the phase diagram the colloids $c$ or the polymer $p$ play a dominant role in the effective wall-colloid interaction $V_{wb}(z)$. We show results which relate $V_{wb}(z)$ to the phase behavior of the solvent $cp$ mixture.

The depletion potential between a big colloid, denoted by $b$, and a planar hard wall can be obtained once the density profile of the component $b$ in the dilute limit, $\rho_b \to 0$, is known [17, 18],

$$\beta W(z) = -\lim_{\mu_b \to -\infty} \ln\left(\frac{\rho_b(z)}{\rho_b(\infty)}\right) - \beta V_b(z) + \beta V_b(\infty). \tag{5.1}$$

The depletion potential in terms of the one-body direct correlation functions $c_b^{(1)}(z)$ is given by [18]

$$\beta W(z) = c_b^{(1)}(z \to \infty; \{\mu_i \neq b\}; \mu_b \to -\infty) - c_b^{(1)}(z; \{\mu_i \neq b\}; \mu_b \to -\infty), \tag{5.2}$$

and follows from the density profiles of the *cp* solvent via Eq. (2.32). Within the FMT approach we use the route of Eq. (5.2) to evaluate the depletion potentials. In Figs. 5.2(a) and 5.2(b) we show depletion potentials for state-points following a horizontal line in the phase diagram, i.e., at fixed polymer packing fraction in the reservoir $\eta_p^r = 0.63$ and increasing colloid packing fraction $\eta_c$. All solvent particles are of equal size, $\sigma_c = \sigma_p$, while the size of the inserted big colloidal particle is $\sigma_b = 5\sigma_c$. Figure 5.2(a) shows a deep potential and little oscillatory effects for low concentrations of the colloid $c$ (full line). Upon increasing $\eta_c$ the potential at intermediate distance $z$ becomes significantly deeper. At contact, $z = 2.5\sigma_c$, however, the depth of the potential decreases for larger values of $\eta_c$ (dashed and dotted lines). In Fig. 5.2(b) we find that upon increasing $\eta_c$ further (full line) the potential becomes less deep at contact and the oscillations are more pronounced. At $\eta_c = 0.3$, the largest value shown here, we find strong oscillations and the depletion potential exhibits similar behavior to the one of a binary hard-sphere mixture [18] as the polymer species has little influence. Note that the value of the depletion potential at contact increases at first for increasing $\eta_c$, while it decreases for very high $\eta_c$. Besides those at the axis with $\eta_c = 0$ we did not find depletion potentials with purely monotonic behavior in the whole $z$-range. The oscillations in the range of small and intermediate distance $z$ also occur for very low values of $\eta_c$, though they are of small amplitudes in that regime. In the asymptotic regime, $z \to \infty$, for low values of $\eta_c$ the depletion potential exhibits monotonic exponential decay, while for higher values of $\eta_c$ the increasing contribution of hard spheres leads to oscillatory exponential decay. The line in the phase diagram which separates regions with those two different types of decay in the structure and in the depletion potential is called the Fisher-Widom (FW) line [115].

## 5.2 Surface virial coefficient

The phase behavior of a one-component fluid is determined by the mutual interaction potential between the particles. The virial coefficient $B_2$ relates both, the

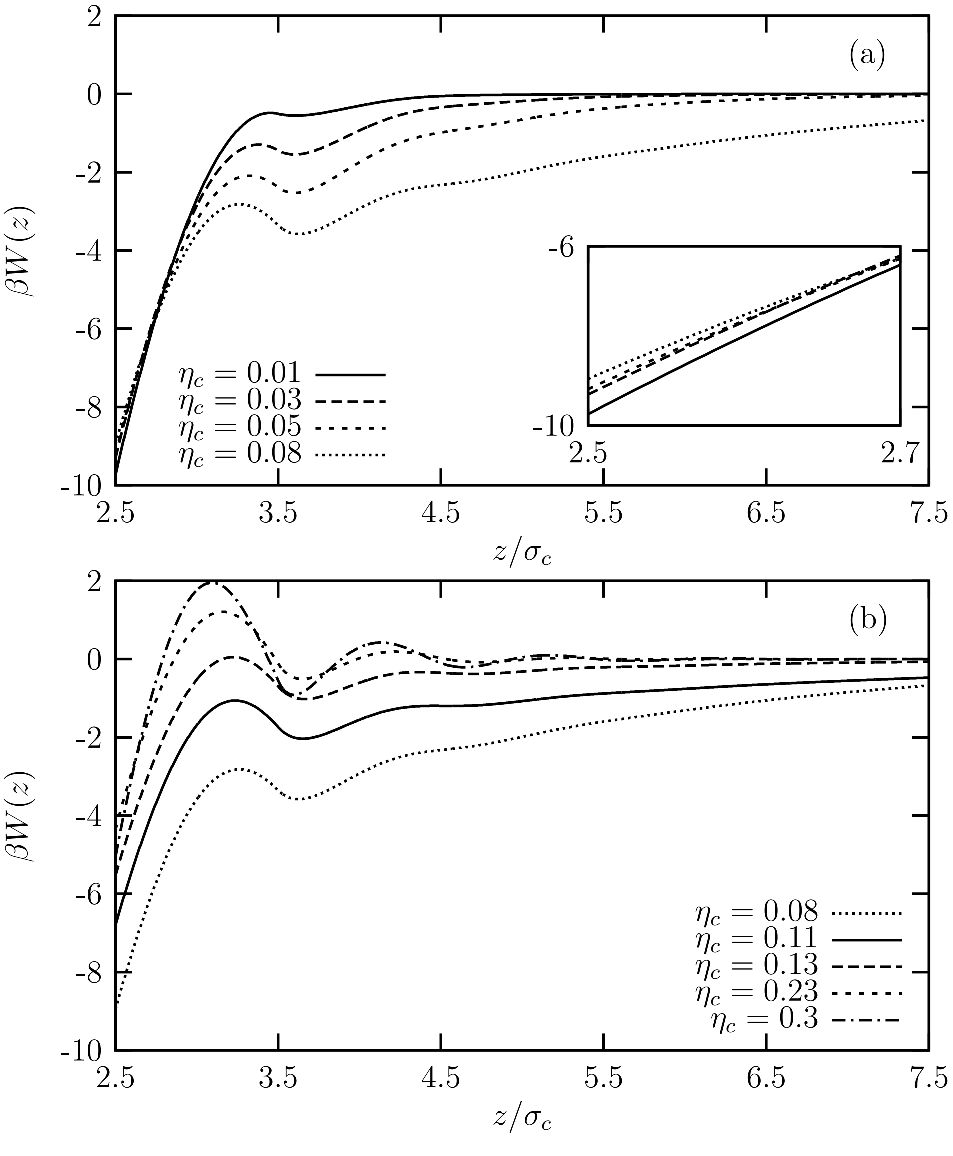

Figure 5.2: Depletion potentials between a spherical colloidal particle $b$ and a planar hard wall $w$. The solvent is the AOV mixture of smaller colloids $c$ and polymer particles $p$. The size ratio among the different components is $\sigma_p : \sigma_c : \sigma_b = 1:1:5$. We show results for state-points on a horizontal line in the fluid phase of the phase diagram with $\eta_p^r = 0.63$. In (a) we show results for lower values of the colloid packing fraction $\eta_c$. Figure (b) shows depletion potentials for higher values of $\eta_c$. In the limit $\eta_c \rightarrow 0$ the depletion potential within the AO approximation is known exactly (not shown here).

phase behavior and the interaction potentials, as it appears in expansion approaches to the equation of state and is based on the interparticle interaction potential, $B_2 = -1/2 \int f(\mathbf{r}) \mathrm{d}\mathbf{r}$, where $f(\mathbf{r})$ is the Mayer-f function. For a solvent with rich phase behavior it is interesting to figure out how much of the phase behavior can be described by the complex interactions that capture the solvent influence in terms of an expansion approach. We study the virial coefficient which relates the bulk phase behavior of the solvent to the depletion interaction between a planar hard wall $w$ and a big colloid $b$ immersed in the AOV mixture, which in bulk for a symmetric size ratio between the colloids $c$ and the polymer $p$ exhibits fluid–fluid phase separation. To this end we use the following definition of the second surface virial coefficient

$$\hat{B}_2 = -\frac{1}{2} \int [\exp\left(-\beta V_{wb}(z)\right) - 1] \, \mathrm{d}\mathbf{r}, \tag{5.3}$$

with $V_{wb}(z) = V_{HW}(z) + W(z)$. We divide the wall-particle interaction $V_{wb}(z)$ into two terms, one describing the hard-core repulsion between the hard wall and the big colloid, $V_{HW}(z)$, and a second describing the effective potential $W(z)$ due to the solvent, and obtain

$$\hat{B}_2 = \frac{A}{2} \int_0^{\sigma_{bb}/2} [1 - \exp\left(-\beta V_{HW}(z)\right)] \mathrm{d}z + \frac{A}{2} \int_{\sigma_{bb}/2}^{\infty} [1 - \exp\left(-\beta W(z)\right)] \mathrm{d}z. \tag{5.4}$$

The first term equals $A\sigma_{bb}/4$, while the second expression contains the contributions due to the effective interactions of the solvent and is more difficult to obtain. We define the effective interaction potential contribution $\tilde{B}_2$ to the second surface virial coefficient,

$$\tilde{B}_2 \equiv \int_{\sigma_{bb}/2}^{\infty} [1 - \exp\left(-\beta W(z)\right)] \mathrm{d}z. \tag{5.5}$$

Note that the depletion potential $W(z)$ and hence the virial coefficient $\tilde{B}_2$ are known exactly for a big colloid $b$ immersed in a solvent composed of the ideal polymer $p$ only. In Fig. 5.3 we show the result for state-points at a trajectory in the phase diagram with $\eta_c + \eta_p^r = 0.3$ and the size ratios $\sigma_p : \sigma_c : \sigma_b = 1 : 1 : 5$. For pure ideal polymer, $\eta_c \to 0$, we find the (analytic) minimum of $\tilde{B}_2$, and increasing the colloid packing fraction leads to increasing values of $\tilde{B}_2$ — see the depletion potentials shown in Fig. 5.4 for the same trajectory in the phase diagram. The full line shows the result for very low colloid packing fraction, $\eta_c = 0.001$, which is very close to the exact result. Though the depletion potentials for intermediate and large values of $\eta_c$ exhibit pronounced oscillations, the value at contact becomes more negative and determines the behavior of $\tilde{B}_2$. At intermediate colloid packing fractions $\eta_c$ (dotted lines) the negative region of $W(z)$ is narrower and the absolute value is lower. Hence, the virial coefficient $\tilde{B}_2$ increases and is maximal at approximately $\eta_c = 0.13$. Upon further increasing $\eta_c$,

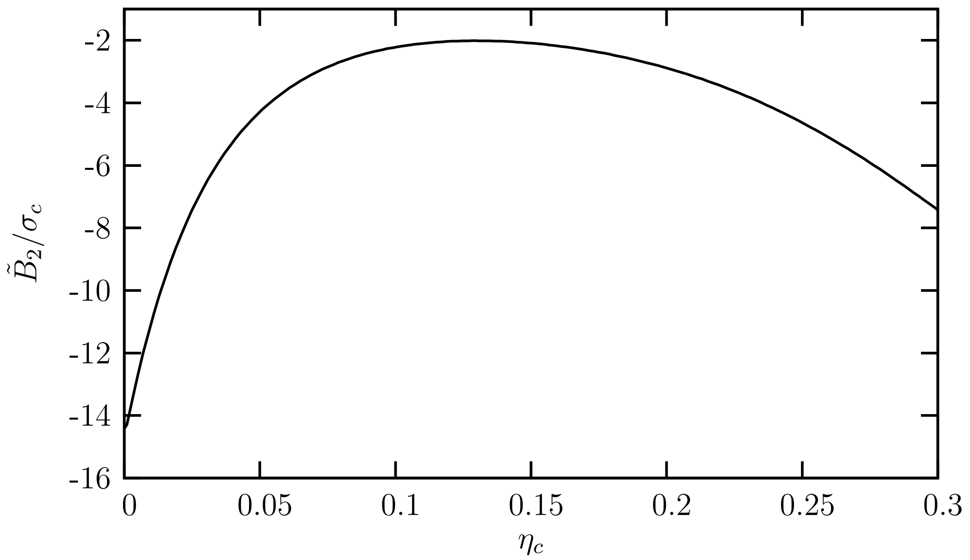

Figure 5.3: The effective interaction potential contribution to the second surface virial coefficient $\tilde{B}_2$ along a trajectory in phase diagram, $\eta_c + \eta_p^r = 0.3$. The full line shows the result for an AOV mixture with size ratio between the solvent particles $\sigma_p : \sigma_c = 1 : 1$. The size of the big particle is $\sigma_b = 5\sigma_c$. We observe one minimum at $\eta_c = 0$ and one at $\eta_p^r = 0$, or equivalently at $\eta_c = 0.3$. In the intermediate regime we find a maximum value of $\tilde{B}_2$.

i.e., equivalently upon reducing the contribution $\eta_p^r$ of the polymer, the oscillatory behavior in the potential becomes more pronounced. It is important to note that the value of the depletion potential at contact decreases when further increasing $\eta_c$ (cf. the dash-dotted lines in Fig. 5.4). In Fig. 5.3 we find a local minimum in $\tilde{B}_2$ for the maximum value of $\eta_c$ considered here and the limit value of a pure hard-sphere solvent.

So far we have shown results for $\tilde{B}_2$ for state-points in the (bulk) fluid phase of the AOV mixture, i.e., for sufficiently low polymer density. In Fig. 5.5(a) we show results for a range of both packing fractions, $\eta_c$ and $\eta_p^r$ respectively. Due to the strong increase of the absolute value of $\tilde{B}_2$ for high packing fractions we show the data also in a logarithmic representation, $\log|\tilde{B}_2/\sigma_c|$, in Fig. 5.5(b). In both representations, the linear and the logarithmic, we find lines of extremal values in the $(\eta_c, \eta_p^r)$-plane. When we follow horizontal trajectories in the phase diagram, i.e., we keep $\eta_p^r$ fixed and vary $\eta_c$, we find a maximum value of the virial coefficient $\tilde{B}_2$ and accordingly a minimum value for $\log|\tilde{B}_2/\sigma_c|$. Figure 5.6 shows contour lines to the result of the logarithmic representation shown in Fig. 5.5(b). Along path $A$, i.e., for low values of $\eta_p^r$, the value of $\tilde{B}_2$ decreases in the whole range shown. The depletion potentials close to the axis, $\eta_c = 0$, are flat such that upon increasing the values of $\eta_c$ the influence

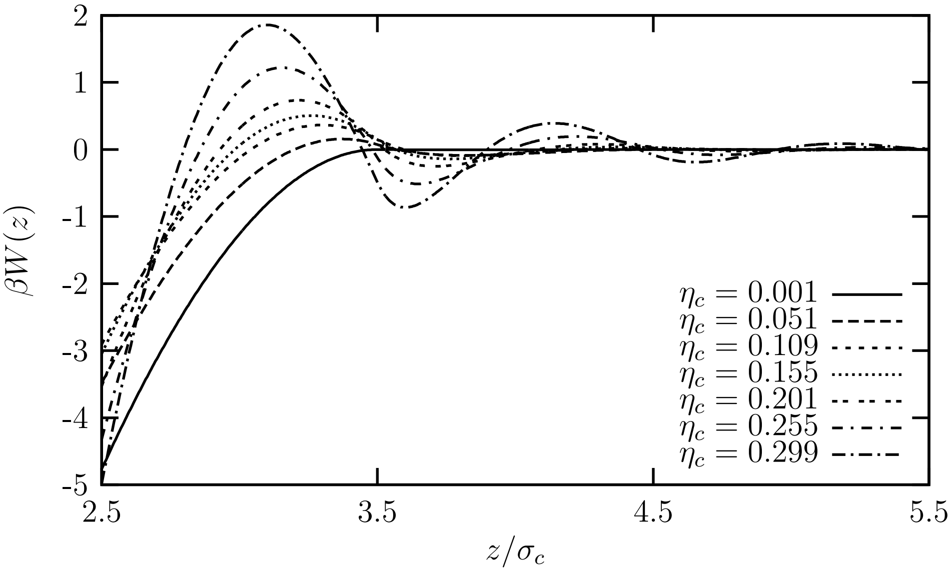

Figure 5.4: Depletion potentials between a spherical colloidal particle $b$ and a planar hard wall. The selected state-points are on a line in phase diagram with $\eta_c + \eta_p^r = 0.3$ and $\sigma_p = \sigma_c$. The diameter of the inserted big colloidal particle is $\sigma_b = 5\sigma_c$. We find low values of the potentials at contact for very high and very low values of $\eta_c$. In the intermediate regime of $\eta_c$ the oscillations are more pronounced than for low values, however, the absolute value at contact is low and leads to small contributions to the surface virial coefficient $\tilde{B}_2$.

on the depletion potential due to the hard-sphere colloids is increased gradually and $\tilde{B}_2$ exhibits monotonic behavior. For the path $B$, i.e., at an intermediate value of $\eta_p^r$, for low values of $\eta_c$ we find increasing $\tilde{B}_2$ and a decrease in $\tilde{B}_2$ for larger $\eta_c$. Along this path for low $\eta_c$ the influence of the polymer is stronger than for path $A$ and the depletion potential has a deep minimum at contact. For increased colloid packing fraction we find a competition between the polymer and the colloid contribution to the depth of the depletion potential. At low values of $\eta_c$ the value of the depletion potential near contact is strongly negative and leads to strong negative values of $\tilde{B}_2$. At intermediate values of $\eta_c$ the contact value of $W(z)$ is less negative, which gives smaller contribution to $\tilde{B}_2$, but due to pronounced oscillations we have an additional contribution to $\tilde{B}_2$. The sum of both contributions leads to increasing $\tilde{B}_2$ in that range of $\eta_c$. For large values of the colloid packing fraction $\eta_c$ the oscillations become more pronounced and the value of the depletion potential at contact becomes strongly negative. In this range the contribution of the colloids to the surface virial coefficient $\tilde{B}_2$ becomes very strong and due to the deep minimum at contact the value of $\tilde{B}_2$ becomes strongly negative. The contour lines in Fig. 5.6 visualize the behavior of

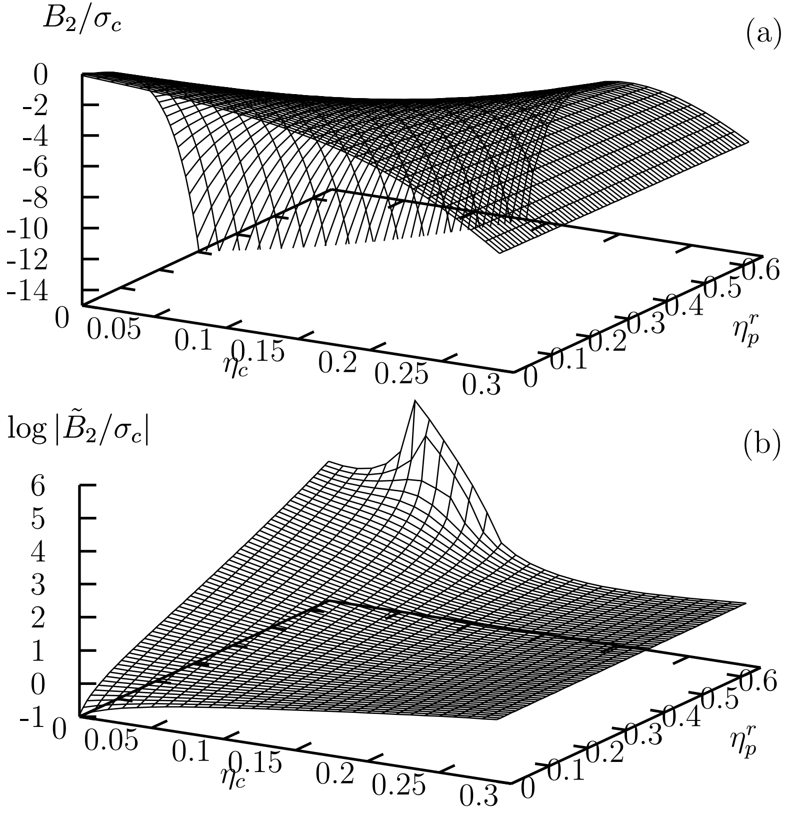

Figure 5.5: (a) Surface virial coefficient $\tilde{B}_2$ for the same parameters as in Fig. 5.3 but now in a wide range of packing fractions $\eta_c$ and $\eta_p^r$ of the solvent species. At horizontal lines in the phase diagram, i.e., fixed $\eta_p^r$, we find points with maximum values of $\tilde{B}_2$. Upon increasing packing fractions the (absolute) value of $\tilde{B}_2$ increases strongly. In Fig. (b) we show the virial coefficient $\tilde{B}_2$ in logarithmic representation. For increasing packing fractions we find very strong increase. Note that the critical point is in the same region, $\eta_c = 0.103$ and $\eta_p^r = 0.635$, and the strong increase occurs in the vicinity of the fluid–fluid binodal (cf. Fig. 3.2).

the surface virial coefficient $\tilde{B}_2$ in the whole $(\eta_c, \eta_p^r)$-plane. The maximum values of the contour lines in the $(\eta_c, \eta_p^r)$ representation yield a line which divides the phase diagram into regions where the virial coefficient $\tilde{B}_2$ increases (above the full line) upon increasing $\eta_c$ and where $\tilde{B}_2$ decreases (below the full line) upon increasing $\eta_c$. In Fig. 5.6 we compare this line of the maxima (full line) to the Fisher-Widom line (dashed line) which separates regions in phase diagram with purely monotonic and oscillatory exponential decay of the depletion potential. We find that both lines exhibit similar behavior.

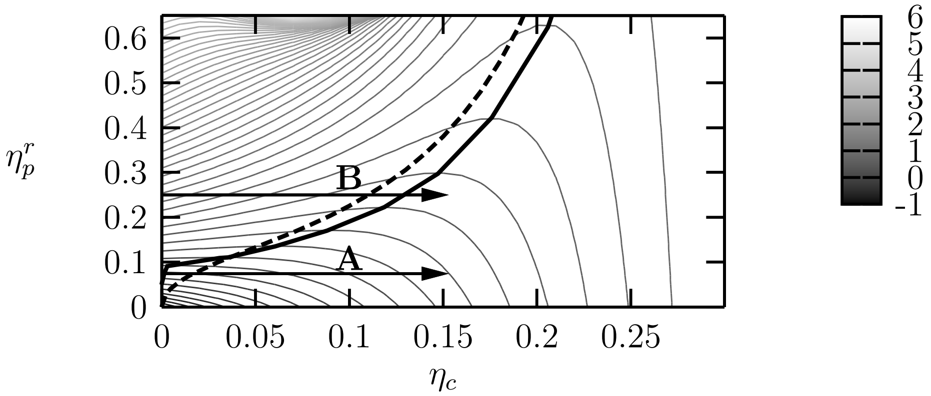

Figure 5.6: Contour lines of the logarithmic representation of the virial coefficient $\tilde{B}_2$. From bottom to top the lines show increasing $\log|\tilde{B}_2/\sigma_c|$. Along the path *A* we find increasing values only, however, path *B* indicates increasing values $\log|\tilde{B}_2/\sigma_c|$, i.e., increasing $\tilde{B}_2$ for low $\eta_c$ and decreasing $\tilde{B}_2$ for larger values of $\eta_c$. Points with vanishing slope of the contour lines yield a line which separates the phase diagram into two regions (full line). Following a path at fixed $\eta_p^r$, the latter line equals points with maximum $\tilde{B}_2$. The dashed line is the Fisher-Widom line which separates regions in phase diagram with oscillatory and monotonic exponential decay for large $z$ of density profiles and the depletion potential.

## 5.3 Effective interaction and phase behavior

In the previous section we found a maximum value of the virial coefficient $\tilde{B}_2$ in the fluid regime of the phase diagram and numerical results which display a strong increase of the absolute value of $\tilde{B}_2$ if the packing fractions $\eta_p^r$ are sufficiently high. In this section we relate the virial coefficient $\tilde{B}_2$ to thermodynamic bulk properties and analytically study the strong increase in the vicinity of the fluid–fluid phase separation. The effective interaction between a big colloidal particle $b$ and a planar hard wall in a sea of smaller colloid $c$ and polymer $p$ is given by [18]

$$\beta W(z) = - \lim_{\mu_b \to -\infty} \ln \left( \frac{\rho_b(z)}{\rho_b(\infty)} \right). \tag{5.6}$$

The second surface virial coefficient [116–119] then reads

$$\begin{aligned} \frac{1}{A}\hat{B}_2 &= \frac{\sigma_{bb}}{4} + \frac{1}{2} \int_{\sigma_{bb}/2}^{\infty} \left[ 1 - \lim_{\mu_b \to -\infty} \left( \frac{\rho_b(z)}{\rho_b(\infty)} \right) \right] \mathrm{d}z && (5.7) \\ &= \frac{\sigma_{bb}}{4} + \frac{1}{2} \lim_{\mu_b \to -\infty} \int_{\sigma_{bb}/2}^{\infty} \left[ \frac{1}{\rho_b(\infty)} \left( \rho_b(\infty) - \rho_b(z) \right) \right] \mathrm{d}z. && (5.8) \end{aligned}$$

We relate the virial coefficient to the excess adsorption, which in the following is defined as $\Gamma_i = \int_0^\infty (\rho_i(z) - \rho_i(\infty)) \mathrm{d}z$, and obtain for the integral in the latter equation

$$\lim_{\mu_b \to -\infty} \int_{\sigma_{bb}/2}^{\infty} \left( \frac{\rho_b(z)}{\rho_b(\infty)} - 1 \right) \mathrm{d}z = \sigma_{bb}/2 + \lim_{\mu_b \to -\infty} \frac{\Gamma_b}{\rho_b(\infty)} \tag{5.9}$$

and finally the second surface virial coefficient is given by

$$\frac{1}{A}\hat{B}_2 = -\frac{1}{2} \lim_{\mu_b \to -\infty} \frac{\Gamma_b}{\rho_b(\infty)}. \tag{5.10}$$

The adsorption is related to the wall-fluid surface tension via the Gibbs adsorption theorem

$$\Gamma_i = - \left. \frac{\partial \gamma^{wf}}{\partial \mu_i} \right|_{T,V,\mu_{j \neq i}}, \tag{5.11}$$

where we set $i = b$ and $j = c, p$ in our situation. In the limit of vanishing density $\rho_b$ of the big colloidal component, or equivalently $\mu_b \to -\infty$, we obtain

$$\lim_{\mu_b \to -\infty} \left. \frac{\partial \gamma^{wf}}{\partial \mu_b} \right|_{\mu_{j \neq b}} \propto \lim_{\rho_b \to 0} \left[ \int_{\sigma_{bb}/2}^{\infty} \left( 1 - \frac{\rho_b(z)}{\rho_b(\infty)} \right) \mathrm{d}z \right]. \tag{5.12}$$

As the variation of the surface tension w.r.t. the chemical potential is not known directly we employ the chain rule to split the derivative in the latter expression into the following series of products

$$\begin{aligned} \Gamma_j &= - \left. \frac{\partial \gamma}{\partial \mu_j} \right|_{\{\mu_{k \neq j}\},V,T} && (5.13) \\ &= - \sum_i \left. \frac{\partial \gamma}{\partial \rho_i} \right|_{\{\mu_{k \neq j}\},V,T} \left. \frac{\partial \rho_i}{\partial \mu_j} \right|_{\{\mu_{k \neq j}\},V,T}. && (5.14) \end{aligned}$$

Within FMT the pressure $p$, the surface tension $\gamma$ and the bending rigidities $\kappa$ and $\bar{\kappa}$ are related to derivatives of the excess free energy density $\Phi$. For mixtures of colloids and polymer we employed a linearized w.r.t. polymer density expression for $\Phi$. Then the first factor in Eq. (5.14), which we do not need in the following, is given by the following approximate expression

$$\beta \frac{\partial \gamma}{\partial \rho_i}\bigg|_{\{\mu_{k\neq j}\},V,T} = \frac{\partial}{\partial \rho_i}\left(\frac{\partial \phi^{ex}(\{n_\alpha^c, n_\alpha^p\})}{\partial n_2^c}\right)\bigg|_{\{\mu_{k\neq j}\},V,T}. \tag{5.15}$$

This relation strictly holds only for low values of the density $\rho_p$ as $\beta\gamma = \partial\phi^{ex}/\partial n_2^c$ is linear in $\rho_p$. In a more accurate description one should also consider higher order terms. The second factor with $\mu_j = \partial f/\partial \rho_j$ and $\beta f = \phi^{ex} + f^{id}$ yields

$$\frac{\partial \mu_j}{\partial \rho_i} = \frac{\partial^2 \phi^{ex}}{\partial \rho_i \partial \rho_j} + \delta_{ij}\frac{1}{\rho_j}. \tag{5.16}$$

We insert these expressions into Eq. (5.14) and obtain the following result

$$\frac{\partial \gamma}{\partial \mu_j}\bigg|_{\mu_{k\neq i}} \approx \sum_{i=b,c,d}\left[\frac{\partial}{\partial \rho_i}\frac{\partial \phi^{ex}}{\partial n_2^c}\right]\left[\frac{\partial^2 \phi^{ex}}{\partial \rho_i \partial \rho_j} + \delta_{ij}\frac{1}{\rho_j}\right]^{-1}. \tag{5.17}$$

Note that second factor denotes an inverse matrix. Taking this fact into account we may express the latter result for the second surface virial coefficient in terms of a nominator $N$ and denominator $D$, $-\frac{2}{A}\hat{B}_2 = \frac{N}{D}$. We obtain diverging values of $\hat{B}_2$ when we consider $D = 0$. In this limiting case of a divergent value of the second surface virial coefficient, we find an implicit equation which relates the packing fraction of the colloid $c$ and the polymer $p$

$$\eta_p = \frac{(1-\eta_c)^4(2\eta_c+1)/\eta_c}{12(1-\eta_c)^3 + 15q(1-\eta_c)^2(2\eta_c+1) + 6q^2(1-\eta_c)(2\eta_c+1) + q^3(2\eta_c+1)^3}, \tag{5.18}$$

with $q = \sigma_p/\sigma_c$ the size ratio of the solvent particles. The result is shown in Fig. 5.7 for a solvent with $q = 0.6$ and upon employing the linearized AOV version of Rosenfeld's expression for the excess free energy. The result in Eq. (5.18) equals the explicit expression for the fluid–fluid spinodal within the same formulation of FMT. This is not surprising since the equation for the spinodal is given by $\partial^2 f/\partial \rho_i \partial \rho_j = 0$ [see Eq. (2.46)].

## 5.4 Conclusions

We showed the influence of the phase behavior of a colloid-polymer solvent onto the interaction between a big colloidal particle and a planar wall. We find that the corresponding depletion potential exhibits rich behavior. For state-points near phase coexistence we find long-ranged behavior when still short-ranged structure occurs in the density profiles. The depletion interaction reflects the phase behavior

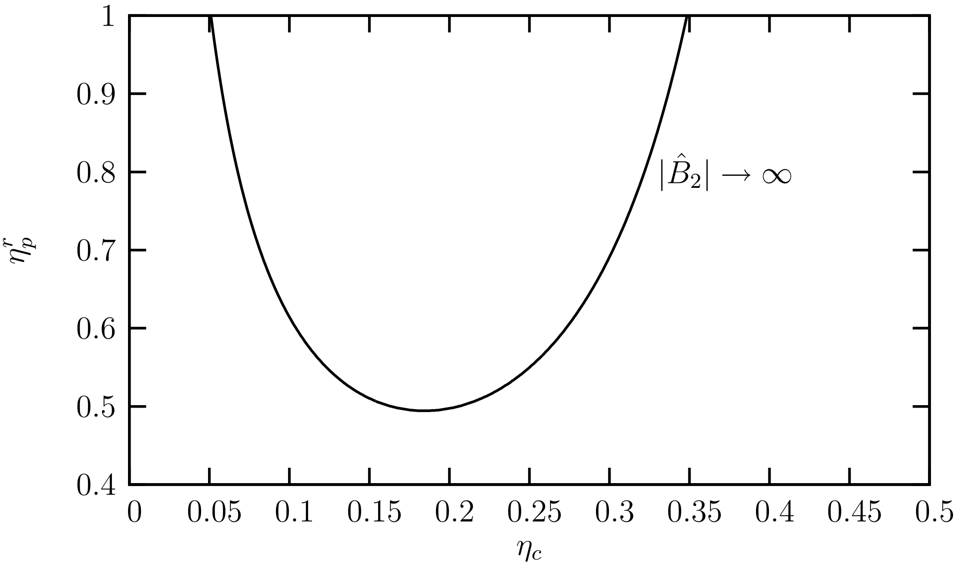

Figure 5.7: Divergence of the second surface virial coefficient $\hat{B}_2$ based on the implicit expression in Eq. (5.18). The line shows values in phase diagram where the denominator of $\hat{B}_2$ vanishes, $D = 0$. The explicit expressions for the line with diverging surface virial coefficient, $|\hat{B}_2| \to \infty$, and the one for the fluid–fluid spinodal coincide.

of the AOV mixture in bulk. Via the second surface virial coefficient we find a relation between the depletion interaction mediated by the solvent and its bulk phase behavior. These findings establish a basis for further study of the effective interactions between particles immersed in a phase-separating solvent.

# Chapter 6

# Complex Solvents

It is a demanding task to figure out the effective interaction a phase-separating solvent mediates between two colloids [120–122], or between a particle and a flat planar wall as shown by means of simulations [111] or DFT calculations [112]. An appropriate model to treat phase-separating many-component fluids is the AOV model. The influence of a complex solvent onto the mapping procedure has been studied in various cases. Size-polydisperse hard-sphere solvents exhibit strong influence on the effective interaction between two very big colloids [47], and simulations for particles with the repulsive part of the Lennard-Jones potential show that wetting effects induce depletion attraction [123]. In this chapter we study the rich phenomenology of a colloid-polymer mixture at two big colloids and at one ellipsoidal particle. We study some aspects of the influence of the rich solvent properties on the interaction and thermodynamics of colloids. To this end we employ the AOV model to describe the solvent as it covers many effects. We can benefit from the fact that the approaches to treat AOV mixtures are well-developed [14, 38, 84] as presented in the three previous chapters in the case of bulk and inhomogeneous mixtures. In the following we focus on the mixture PY equation of state and Rosenfeld's original formulation of FMT for the hard spheres and the corresponding linearized Rosenfeld formulation of FMT [Eqs. (2.38) and (2.39)] for the AOV mixture.

## 6.1 Two colloids in a phase-separating solvent

In Chapter 4 we presented results from density functional theory for a mixture confined between two parallel plates. In that case we used the symmetry of the system, $\rho(\mathbf{r}) = \rho(z)$, for a DFT approach. Exploiting symmetries makes the DFT approach numerically efficient and more accurate. Usually, the depletion potential is calculated using the insertion approach, where one particle is fixed at the origin and turned into an external potential and the second particle is inserted into the inhomogeneous solvent [Eqs. (5.1) and (5.2)]. The inserted particle is described as a further component in the limit $\rho_b \to 0$. When we evaluate the depletion potential between two particles $b$ in a sea of a solvent within the present DFT approach, the density profiles required for the evaluation of the depletion potential via Eqs. (5.1) and (5.2) are those of a system of one fixed particle. For a further species of the same particles one considers $\rho_b \to 0$ and the second particle is not yet inserted into the system. To this end we employ the fundamental measure approach within DFT for systems with rotational symmetry. Then, the density profile $\rho(\mathbf{r}) = \rho(z, r)$ and both particles of species $b$ are inserted into the system when the density profiles are evaluated. We show results in three different situations: Firstly, a one-component hard-sphere fluid around two large colloids which corresponds to a binary hard-sphere mixture in the low density limit of the larger component, $\rho_b \to 0$. Secondly, we show results for a colloid-polymer solvent around two colloids and turn our attention on the influence of solvent phase separation, and thirdly, we present results for the AOV mixture at an ellipsoidal particle.

Depending on the shape of the fixed particle, which is considered as an external potential in the DFT route, one usually employs appropriate coordinate systems, e.g., spherical coordinates for one fixed spherical colloid or bispherical coordinates for two fixed spherical colloids. In contrast to those commonly used coordinates we generate a grid from triangulation of the space in which $V_{ext} = 0$ and regions which are required for the convolutions within FMT. We employ the Tanemura-Ogawa-Ogita algorithm. For carrying out the integrations we use a Gaussian quadrature in high order, which for evaluating weights, must be performed only once. Special care has to be taken for particles which intersect the symmetry axis. Based on this general procedure we are able to represent any object with hard-core repulsion and rotational symmetry around one axis. However, we have to pay the price for this comfort by a considerable numerical effort. In contrast to the Fast-Fourier-Transform for which in one dimension the convolutions can be performed in $\mathcal{O}(N \log N)$ operations, in real-space it takes $\mathcal{O}(N^2)$. For the two-dimensional grids in real-space the convolutions take $\mathcal{O}(N^4)$ operations. Moreover, studying layering and wetting phenomena dramatically increases the number of iterations in the minimization procedure within DFT. For example, for an AOV mixture around two colloids it takes $10^4$ iterations for a state-point far from layering effects and increases to $3.5 \cdot 10^5$ in the vicinity of layering. Due to this fact we consider the systems with up to $7 \cdot 10^4$ grid points which is roughly 265 points for each direction. In Fig. 6.1 we show a part of an example grid.

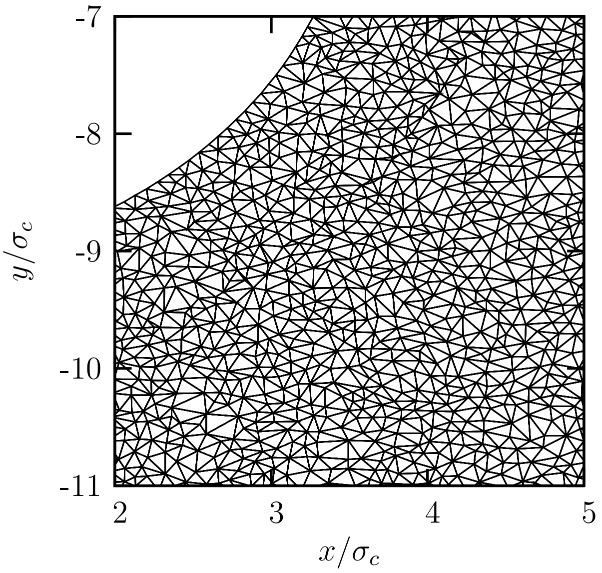

Figure 6.1: Triangular grid generated via the Tanemura-Ogawa-Ogita algorithm. In the top left corner there are no points, here $V_{ext} = \infty$ and in addition the points are not accessed in the convolutions. Only a cut-out of the complete grid for two large colloids as external potential is shown, which in this example contains much less points than the ones in the DFT calculations below.

We consider two big colloids $b$ in a sea of a one-component hard-sphere fluid of colloids $c$. This situation corresponds to a binary hard-sphere mixture in the dilute limit, $\rho_b \to 0$. We choose $\sigma_c : \sigma_b = 1 : 10$. A natural question is to study the grand potential which can be employed to evaluate the depletion potential between the big colloids $W(r) = \Omega(r) - \Omega(r \to \infty)$ [124,125]. In our approach we use a different grid for each distance $2L$ of the big colloids which leads on the one hand to a low accuracy of $W(r)$ in the intermediate and the asymptotic regime of $r$. However, on the other hand we gain results for the adsorption of the small colloids when the separation between the big colloids becomes smaller. At contact, $L = 5\sigma_c$, we find a maximum of $|W(r)|$ and a decrease for increasing distance. A minimum appears at $L \approx 5.35\sigma_c$ and the following maximum we can resolve is at $L \approx 5.6\sigma_c$. More directly we can benefit from our approach, $\rho(\mathbf{r}) = \rho(z, r)$, when we compare to the density profiles from the case when employing radial symmetry, $\rho(\mathbf{r}) = \rho(r)$. The asymptotic behavior of the density profile $\rho(z, r)$ is shown in Fig. 6.2 in the logarithmic representation, $\log |\sigma_c^3(\rho_c(z, r) - \rho_c^{bulk})|$. We find eight oscillations which correspond to the radial distance from one of the big colloids $u = 4\sigma_c$. According to Refs. [126–128] this range for $u$ is sufficient to describe the onset of the asymptotic behavior of quantities which are related to the structure of the fluid, e.g., the density profile and depletion potentials.

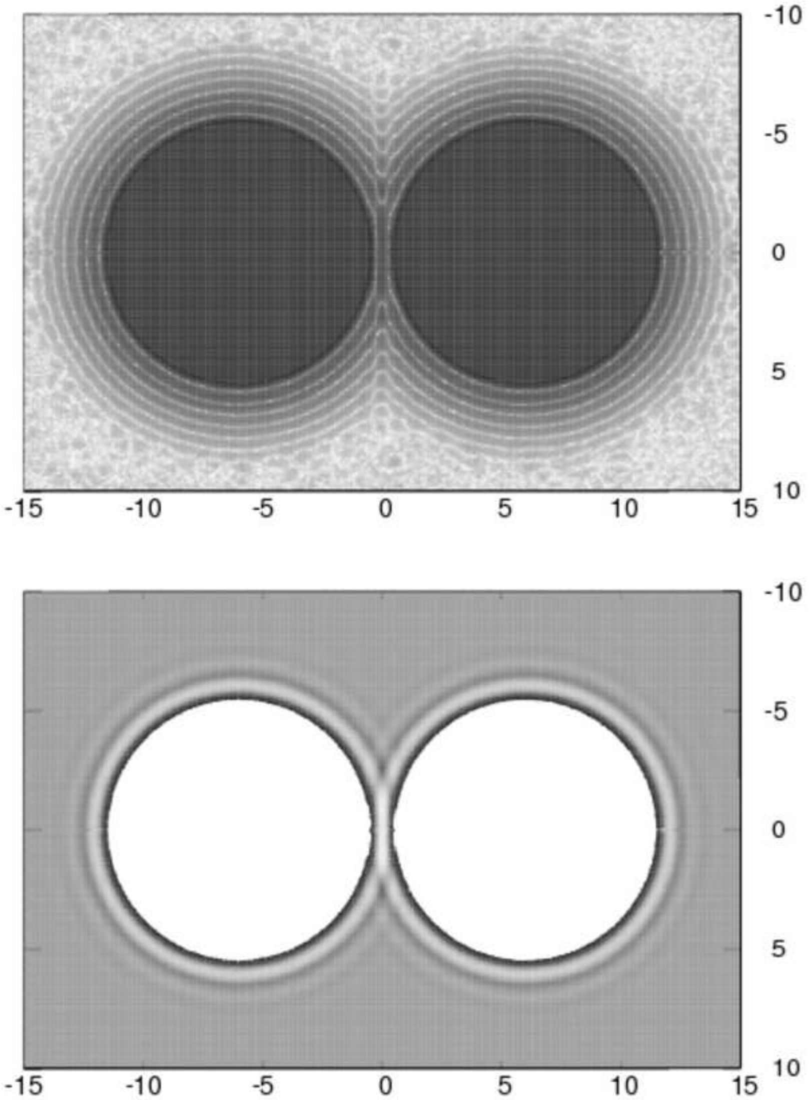

Figure 6.2: Density profile of a one-component hard-sphere fluid of colloids $c$ around two bigger colloids $b$ with diameter $10\sigma_c$ in the logarithmic representation $\log|\sigma_c^3(\rho_c(z,r) - \rho_c^{bulk})|$ (top) and in the linear representation $\rho_c(z,r)$ (bottom). Dark color denotes regions of higher values of $\log|\sigma_c^3(\rho_c(z,r) - \rho_c^{bulk})|$ or $\rho_c(z,r)$, respectively. This case corresponds to a binary hard-sphere mixture in the dilute limit $\rho_b \to 0$ and the colloid packing fraction $\eta_c = 0.3$. Within this approach we can resolve oscillations in the density up to $4\sigma_c$ in the radial direction from one of the big colloids.

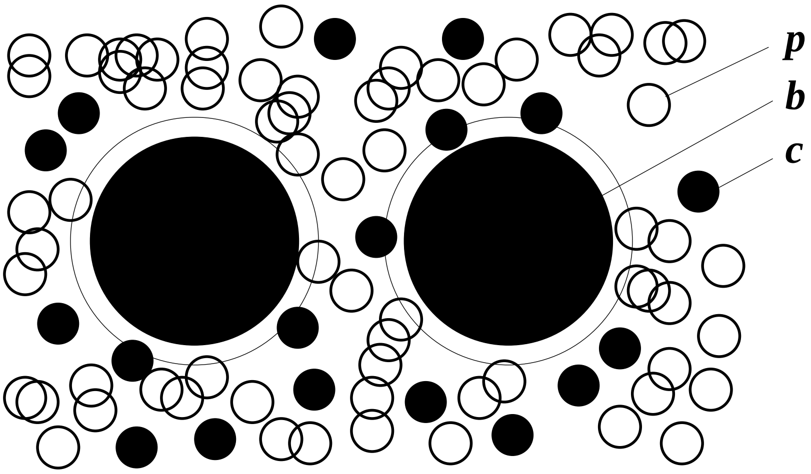

Figure 6.3: Sketch of a solvent modeled by the AOV mixture of colloids $c$ and ideal polymer $p$ in the vicinity of two big colloids labeled $b$. The size ratio between the diameters of the particles is $\sigma_p : \sigma_c : \sigma_b = 1 : 1 : 5$. The polymer may overlap freely among themselves. All the other interactions are hard-core type and no overlap is possible. The thin lines around the big colloids show the free volume which cannot be accessed by center of mass of the solvent particles. Note that only one single line each is needed in this example as $\sigma_c = \sigma_p$.

**Influence of solvent phase separation on the interparticle interaction**

For mixtures of colloids and polymer treated as an AOV fluid a phase separation between a gas (colloid poor) and a liquid (colloid rich) phase can occur for appropriate size ratios of the solvent components (cf. the phase diagrams in Chapter 3). In contact with walls and other big particles a rich surface phase behavior is found and capillary phenomena affect the phase behavior in narrow pores. We study a system of two big colloids labeled $b$ in a sea of an AOV type solvent with one colloid $c$ and one polymer $p$ species (see Fig. 6.3). As for that solvent we find phase separation into two bulk fluid phases we primarily focus on phenomena associated with this finding. To this end one can consider to study the system following two different routes. In the first setup we fix the state-point and vary the distance $L$ between the two big colloids. Thereafter, we study the system with fixed distance $L$ and vary thermodynamic variables, i.e., the state-point. As layering and wetting effects are known from an AOV mixture brought in contact with walls, we pay special attention to that issue. Throughout the following study we keep the size ratios between the particles fixed at $\sigma_p : \sigma_c : \sigma_b = 1 : 1 : 10$.

As we already pointed out above, for the binary hard-sphere mixture our approach due to low numerical accuracy for varying the distance $L$ between the colloids is best suitable for a fixed grid, i.e., fixed distance $L$ and varying state-points. Analogously to the pure hard-sphere solvent in the case of the solvent AOV mixture, we find richer structure in the density profiles $\rho_c(z,r)$ and $\rho_p(z,r)$ in the interspace between the two big colloids as compared to profiles around two separated particles. That finding affects the adsorption and the (mean) contact values of the solvent. We find increased colloid density in the circular wedge-like zone when the two big colloids are close to each other. We find that the depletion potential of two big colloids immersed in an AOV mixture for low $\eta_c$ is very similar to the one obtained from the insertion method.

In the following we focus on a fixed distance of the big colloids and vary the state-point. Via that route we can more clearly show the influence of the phase separation of the solvent on the thermodynamic properties of the system. We keep the reservoir packing fraction $\eta_p^r$ of the polymer fixed and vary the colloid packing fraction $\eta_c$ which means following horizontal tie lines in the $(\eta_c, \eta_p^r)$ representation of the phase diagram. The size ratio $\sigma_p : \sigma_c = 1 : 1$ is fixed, while $\sigma_c : \sigma_b = 1 : 10$ or $1 : 20$ and the packing fraction of the polymer in reservoir $\eta_p^r$ is considered to be a parameter. The surface-to-surface distance of the two big colloids is fixed, $h = 2L - \sigma_b = 1.5\sigma_c$. For the selected polymer packing fractions $\eta_p^r = 0.98, 0.9$ and $0.8$ and low values of the solvent colloid packing fraction $\eta_c$ we consider state-points in the gas phase of the phase diagram. Upon increasing $\eta_c$ we follow a path along horizontal tie lines in phase diagram — see the inset in Fig. 6.5(a). In Fig. 6.4(a) we show the resulting adsorption isotherm for $\sigma_c : \sigma_b = 1 : 10$ and $\eta_p^r = 0.98$. For high colloid packing fractions $\eta_c$ we find a series of transitions between different states. When we examine the density profiles and the difference in the jumps of the adsorption this observation corresponds to layering effects. However, the state-point is in the metastable regime w.r.t. bulk fluid–fluid phase separation. For larger diameters of the big colloids, $\sigma_c : \sigma_b = 1 : 20$, the series of jumps is shifted to lower values of $\eta_c$ [see Fig. 6.5(a)]. The layering lines (at a single sphere) move as a function of the size ratio $\sigma_c : \sigma_b$, i.e., the smaller the value of $\sigma_b$, the closer one finds the layering lines to the critical point. This behavior is similar to curvature dependence of the pre-wetting line on a curved wall [129]. Due to increasing computational effort we cannot increase the size of the big colloids $b$ further. In Fig. 6.5(a) for $\eta_p^r = 0.9$ and $0.8$ we show a series of transitions in the adsorption $\Gamma_c$ at higher values of $\eta_c$.

The grand potentials $\Omega$ for the same state-points are shown in Fig. 6.5(b). In all four cases studied here we find kinks at the positions of the jumps in the adsorption, or equivalently a remainder of a first order phase transition. In the situation of a curved wall we describe a finite number of particles and observe a pseudo phase

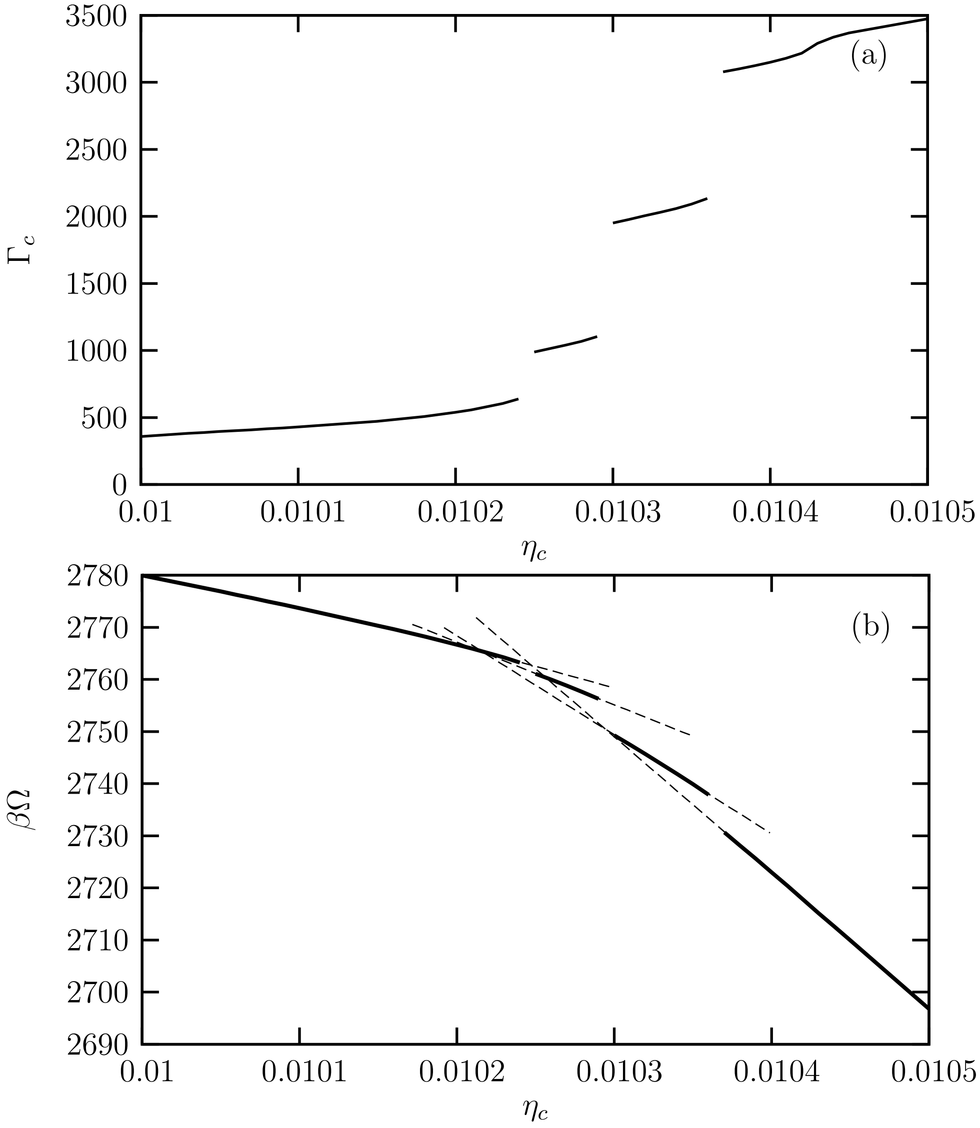

Figure 6.4: Figure (a) shows the excess adsorption $\Gamma_c$ of the solvent colloid in a system of an AOV mixture at two big colloids. The size ratio between the particles is $\sigma_p : \sigma_c : \sigma_b = 1:1:10$. The separation between the big colloids $b$ is fixed, $L = 11.5\sigma_c$, and we choose state-points on horizontal tie lines in phase diagram. The series of jumps corresponds to layering effects. For very high values of $\eta_c$ the adsorption is disturbed by boundary effects. In Fig. (b) we show the corresponding grand potential. We find regions with different slopes which indicate intersection points at lower values $\eta_c$ than shown in the jumps of the adsorption in Fig. (a).

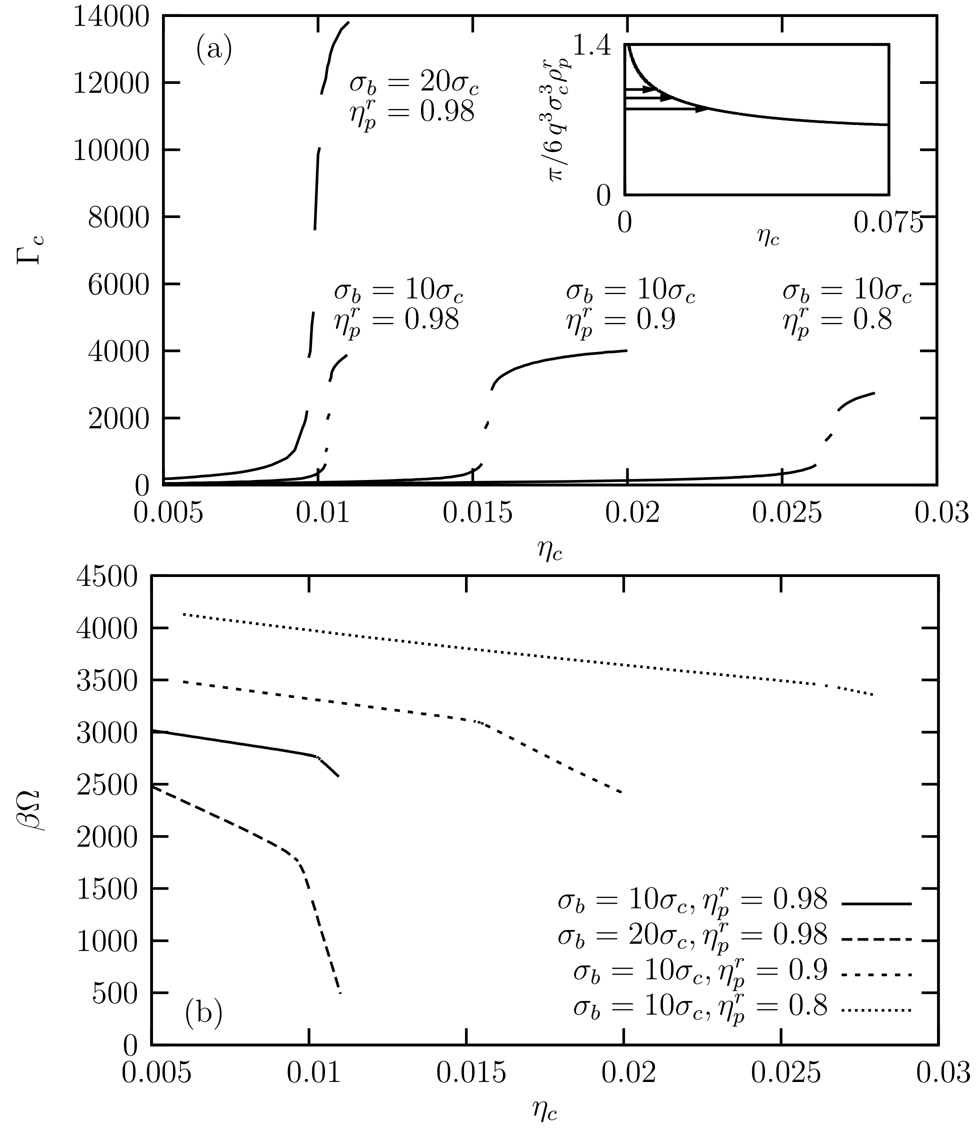

Figure 6.5: In Fig. (a) we show the excess adsorptions $\Gamma_c$ of the solvent colloid in a system of an AOV mixture at two big colloids with fixed distance. For state-points on horizontal tie lines in phase diagram we observe a series of jumps for various parameters of the depletion agent packing fraction $\eta_p^r$ and size of the big colloid $b$. For increasing size $\sigma_b$ the transitions are shifted to lower values of $\eta_c$. Upon decreasing $\eta_p^r$ the curves are shifted to higher values of $\eta_c$. The inset shows the position of the tie lines in the phase diagram. The full line is the fluid–fluid binodal for the AOV mixture with size ratio $\sigma_p/\sigma_c = 1$ based on the PY equation of state. The arrows illustrate the paths along horizontal tie lines with fixed packing fraction of the polymer, $\eta_p^r = 0.98, 0.9$ and 0.8, and varying colloid packing fraction $\eta_c$. The grand potentials for the same parameters are shown in Fig. (b). We find sections with different slopes which lead to intersection points. These points mean the transitions between the layering states which are at slightly lower colloid packing fractions $\eta_c$ than indicated by the jumps in the adsorptions in Fig. (a).

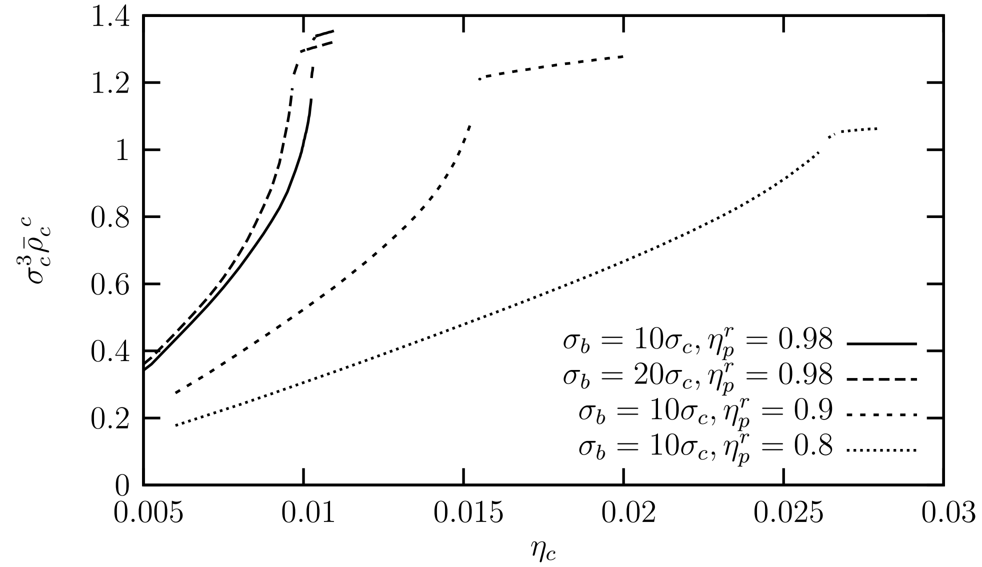

Figure 6.6: Average colloid contact values $\bar{\rho}_c^c$ at state-points on horizontal tie lines in phase diagram. The kinks correspond to layering transitions and the complete wetting regime. At the plateau the contact value of the condensed phase is reached.

transition. Figure 6.4(b) clarifies the situation and we see that two branches of the grand potential (dashed lines) intersect at a slightly lower value of $\eta_c$ than indicated by the jump in the adorption. Note that only the data shown by the full lines are calculated. The dashed lines, which serve as guide to the eye, are extrapolations of the full lines. Some of the data points (full lines) are apparently located on a metastable branch. Similar behavior is found for the case of larger big particle $b$ and state-points with lower $\eta_p^r$. In the average contact values $\bar{\rho}_c^c$ of the solvent colloids and the values $\bar{\rho}_p^c$ of the solvent polymer we find jumps at the transitions (see the inset in Fig. 6.7). The sum $\bar{\rho}_p^c + \bar{\rho}_c^c$, however, is almost independent of $\eta_c$ (see Fig. 6.7) but displays discontinuous behavior at the positions of the transitions indicated by the intersection points of the different branches of $\Omega$. Upon following the path along a tie line and increasing $\eta_c$ the contact values $\bar{\rho}_c^c$ increase strongly and for large $\eta_c$ we find a regime which is weakly dependent on $\eta_c$.

The density profiles $\rho_c(z, r)$ for systems with fixed distance $2L = 11.5\sigma_c$ between the big colloids and for a path along tie lines in the phase diagram exhibit rich structure. For six values we show the results in Fig. 6.8. The values $\eta_c = 0.008, 0.0099$, and 0.01024 correspond to the lowest branch in the adsorption shown in Fig. 6.4(a). For $\eta_c = 0.01025$ and 0.01027 we have chosen state-points which correspond to the branch after the first and in the case $\eta_c = 0.01033$ after the second jump. At $\eta_c = 0.008$ we find the colloidal gas phase. The region between the big colloids is enriched

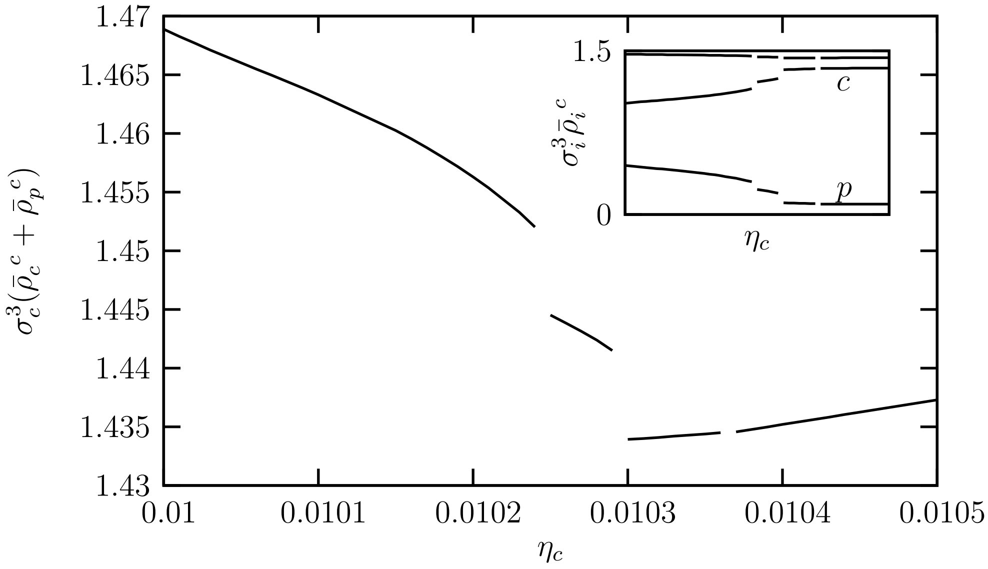

Figure 6.7: Sum of average contact values $\bar{\rho}_p^c + \bar{\rho}_c^c$ at state-points on tie lines in phase diagram. The inset shows the single contributions of the colloids $\bar{\rho}_c^c$ (line labeled $c$) and the polymer $\bar{\rho}_p^c$ (line labeled $p$). The sum is almost constant in the whole range of $\eta_c$ shown, however, we observe jumps with small amplitude at the positions of the transitions.

in the solvent colloid species. According to this finding the density of the polymer is reduced (not shown in the figures). This effect cannot be captured by a DFT route for spherical symmetry and a ternary mixture of species $p$, $c$, and $b$. Upon increasing the colloid packing fraction $\eta_c$ further the smaller colloids are accumulated in this region, and for higher values of $\eta_c$ we find a condensed region between the two big colloids (see Fig. 6.8). The structure clearly exhibits oscillations in this region. The overall shape of the liquid region is dumbbell shaped for lower $\eta_c$ and prolate shaped for higher values. Upon further increasing $\eta_c$ the volume of the liquid region increases, as indicated by the adsorption in Fig. 6.4(a). For very high values of $\eta_c$ the complete space is filled by the colloid liquid phase.

## 6.2 Behavior of a colloid-polymer solvent at curved surfaces

Thermodynamic properties of a fluid depend strongly on the curvature of the objects inserted into the fluid. For example, at planar hard walls layering effects in an AOV fluid are known to be stable while they vanish when very small hard spheres are immersed in an AOV mixture. In the case of objects with non-constant local

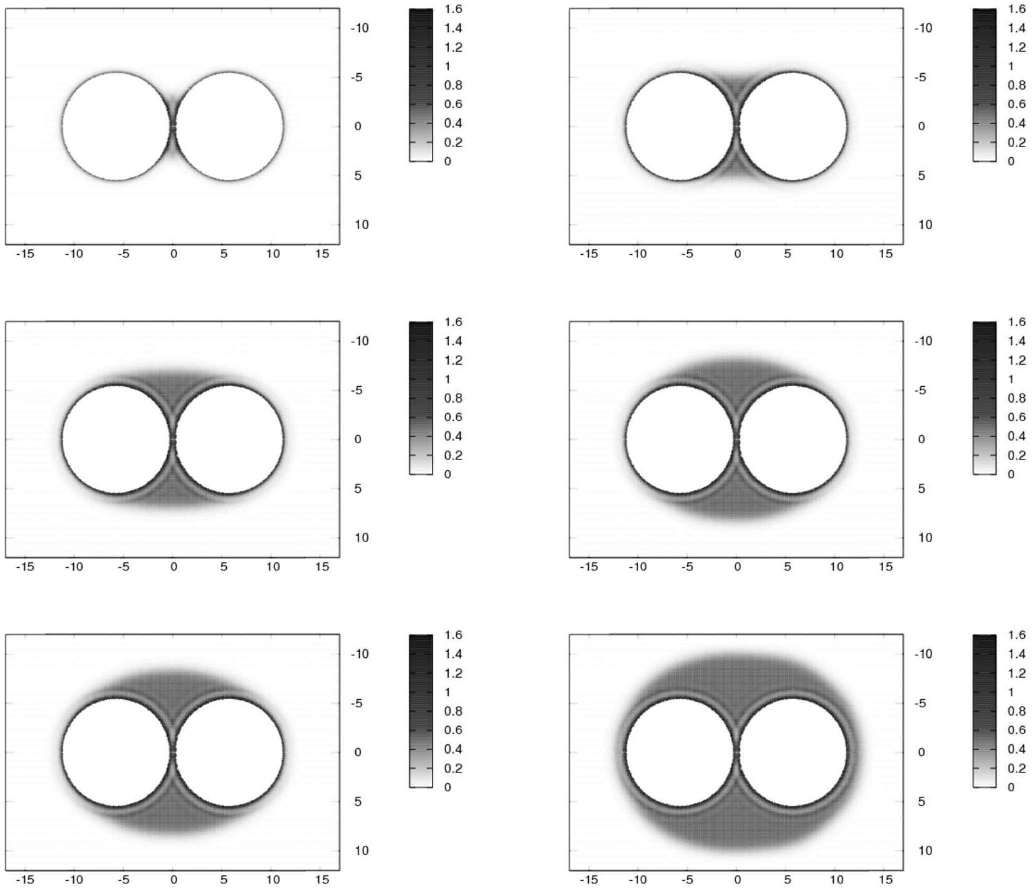

Figure 6.8: Density profiles $\rho_c(z, r)$ of the colloid component of an AOV mixture around two big colloids. The size ratio between the solvent and the big particles is 1 : 10 and $\eta_p^r = 0.98$. In the series of density profiles we fix the distance between the big particles and choose state-points on a horizontal tie line in phase diagram. The colloid packing fraction is varied, $\eta_c = 0.008$ (top left), 0.0099 (top right), 0.01024, 0.01025, 0.01027, and 0.01033 (bottom right). Note the increase in colloid accumulation when $\eta_c$ is slightly increased from 0.01024 to 0.01025 shown by the plots in the middle row and compare to the jump in the adsorption [Fig. 6.4(a)]. For all values we find a strong enrichment of the solvent colloidal particles in the region between the big colloids. The oscillatory structure of the condensed phase is apparent. Corresponding to these results the polymer component of the AOV mixture is repelled from the interspace (not shown here).

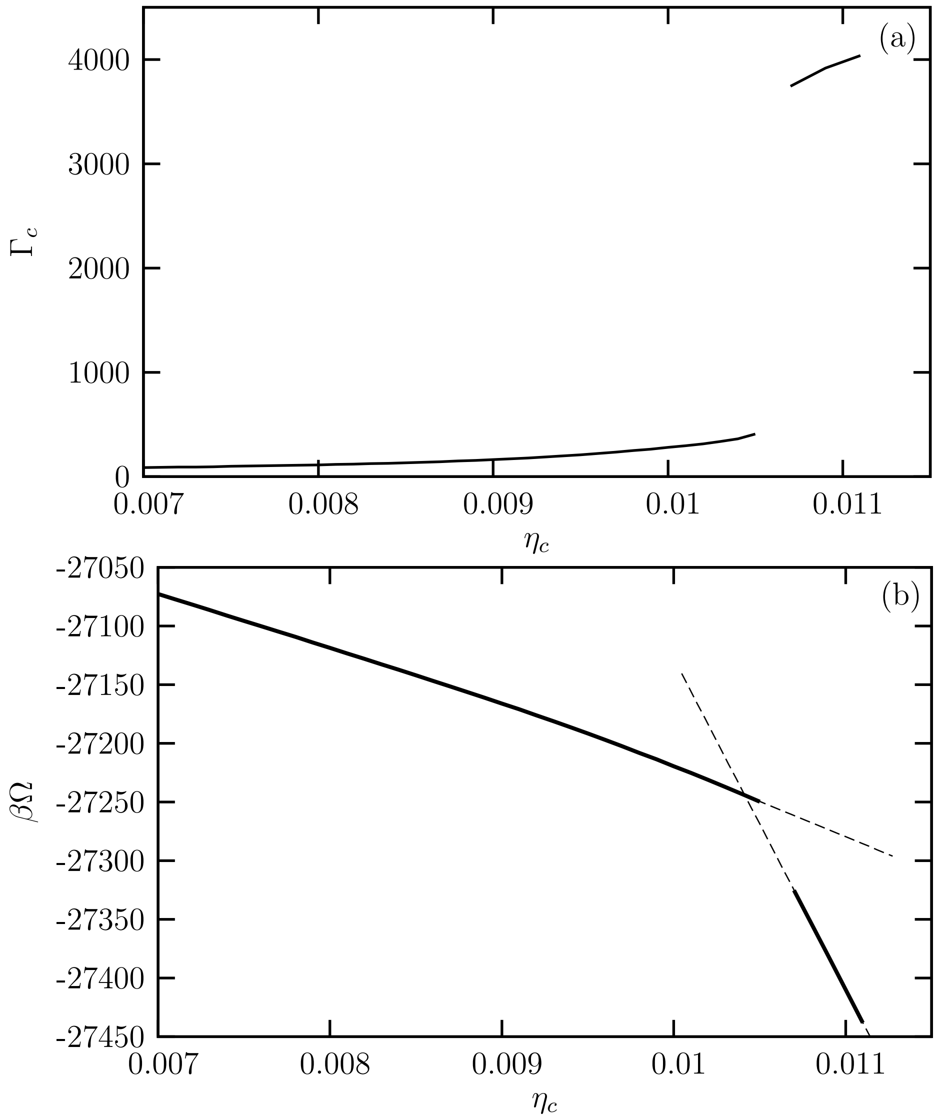

Figure 6.9: Excess adsorption $\Gamma_c$ of the colloid component of an AOV mixture at a prolate ellipsoid — see (a). The size ratio among the two solvent species is 1. For fixed geometry of the ellipsoid we follow state-points on horizontal tie lines in phase diagram. We find a jump in the adsorption which indicates two different states. The situation is clarified when considering the grand potential $\Omega$. Figure (b) shows the grand potential along the same path in phase diagram. At high and at low values of $\eta_c$ we find regions with different slopes. Assuming the lines continue linearly, we find an intersection at $\eta_c \approx 0.0103$. When we compare to the adsorption in (a) we find an indication of a transition between states of different density.

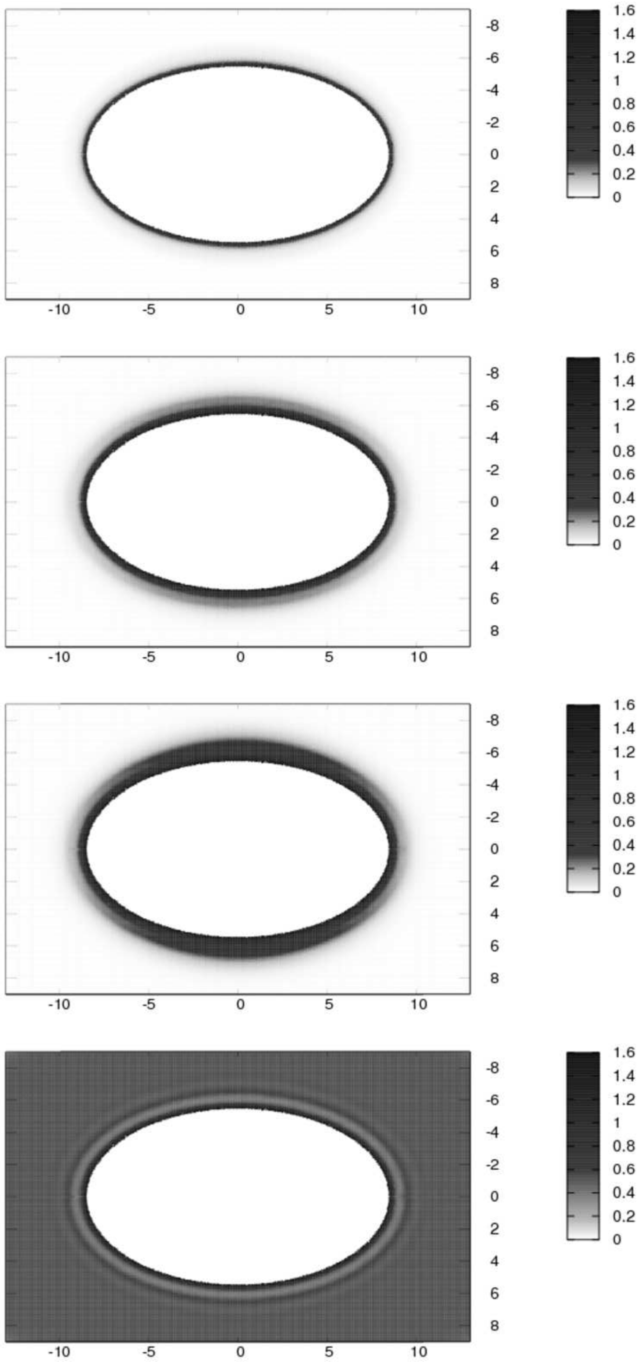

Figure 6.10: Density profiles $\rho_c(z, r)$ of an AOV mixture at a prolate ellipsoidal particle with half-axes $a = 8\sigma_c$ and $b = 5\sigma_c$. For low packing fractions $\eta_c = 0.008$ (top) we find similar behavior in the normal direction at all surface points. Upon increasing $\eta_c$ the local density at the short half-axes increases stronger and we observe layer-like structure ($\eta_c = 0.01$ and $0.0105$). When increasing the packing fraction further, $\eta_c = 0.0111$ (bottom), we find a jump in the adsorption and the whole space is filled with a colloid rich (condensed) phase. In the bottom figure we use different palette for clarity of display.

curvature the thermodynamics is demanding to study. In Ref. [86] a general approach is presented to describe the thermodynamic properties of a fluid in contact with curved walls. The surface tension $\gamma = \sigma + \kappa\bar{H} + \bar{\kappa}K$ depends on the averaged mean- and Gaussian curvatures. The coefficients $\sigma$, $\kappa$ and $\bar{\kappa}$ can be evaluated when using simple geometry. Further thermodynamic quantities can also be expressed in terms of the curvature, for example the average contact value in a general form is given by $\bar{\rho}^c = \beta p + 2\beta\sigma\bar{H} + \beta\kappa\bar{K}$. Density profiles, however, locally depend on the curvature — see Ref. [130] for more details.

In this section we study the behavior of the AOV mixture close to a curved wall. The geometry is kept fixed and we vary the state-point in the same manner as in the case of the two big colloids presented above. We consider the fluid at a big ellipsoidal particle with half-axes $a = 8\sigma_c$ and $b = 5\sigma_c$, where the long half-axis is parallel to the symmetry axis in our numerical procedure. The size ratio of the solvent components is $\sigma_p : \sigma_c = 1:1$. For the packing fraction of the depletion agent $\eta_p^r = 0.98$ and for sufficiently low packing fractions of the solvent colloid $\eta_c$, we choose a state-point in the gas phase of the bulk phase diagram. We increase the value of $\eta_c$ and follow a horizontal tie line in phase diagram. In Fig. 6.9(a) we observe a continuous increase of the excess adsorption of the colloids $\Gamma_c$ while increasing the value of $\eta_c$. In the region $\eta_c \approx 0.0105$ we find a dramatic increase in $\Gamma_c$. As no data are available for this regime we refer to the grand potential $\Omega$. In a similar manner to the case of two big colloids treated in the previous section, we find two regimes with different slopes. Assuming both branches to continue in a well-behaved fashion an intersection point is located at $\eta_c^* \approx 0.0103$. Around this point we find a continuous behavior of the adsorption isotherm at a low value of $\Gamma_c$. Both findings indicate a (first-order) pseudo phase transition in this finite system. For the ellipsoidal geometry we have chosen $\sigma_p : \sigma_c = 1:1$ such that the surface of contact of the colloid $c$ with the ellipsoidal particle and the surface of contact of the polymer $p$ with the ellipsoidal particle are equal. The average contact value of the colloids $\bar{\rho}_c^c$ exhibits similar behavior to the case of two big colloids. We find increasing values of $\bar{\rho}_c^c$ until we reach $\eta_c^*$. For higher values, $\eta_c > \eta_c^*$, we have little data but we find a smaller slope for values above $\eta_c^*$. The local density profiles $\rho_c(z, r)$ directly show the influence of curvature (see Fig. 6.10). At low colloid packing fractions ($\eta_c = 0.008$) the profile is similar in every direction normal to the surface. Upon increasing $\eta_c$ we find a strong increase of the colloid density at the position with lower curvature, i.e., at the short half-axis of the ellipsoid, $z = 0$. Increasing the colloid packing fraction further ($\eta_c = 0.0105$) leads to a layer-like structure in this region while we find vanishing layering structure at the region with largest degree of the curvature. The local contact value of the colloid component shows structure along the surface. Note that many thermodynamical relations are — in terms of sum rules — based on all components. Here the result should illustrate the behavior of the structure along one trajectory. At $r = 0$ and $z = 8.5\sigma_c$ we find minimum values of $\rho_c^c$. Upon continuously decreasing $z$ for the values at contact the colloid density increases until we find a plateau-like behavior. Further decreasing $z$ leads to a small variation of $\rho_c^c$. According to this observation the region enriched by the colloids is depleted in the polymer component.

## 6.3 Outlook

In the case of big colloids immersed in a phase-separating solvent modeled by the AOV mixture we find a rich variety of effects. Layering and bridging effects between two colloidal spheres reveal that mapping of a colloidal mixture of big colloids immersed in a solvent close to phase separation onto an effective one-component system requires much caution. Our approach provides a method to describe many aspects of thermodynamics of colloids like a test of the insertion method or the study of three-body forces. Moreover, we presented results for fluids at ellipsoidal particles and confirmed that curvature effects strongly affect thermodynamic properties.

# Chapter 7

# Conclusions and Outlook

In this thesis we have studied the phase behavior and effective interactions of colloidal suspensions in bulk, in contact with surfaces, and in confined geometry. Colloidal systems cover a broad range of materials as, in general, colloids are defined by their size range. For mixtures of particles with hard-core interactions the AOV model provides an appropriate starting-point. Based on that model we have employed the free-volume theory and the density functional theory.

In experimental systems one faces particles that do not possess well defined characteristics but rather differ in various properties such as the size or shape that arise for example in imperfections of the fabrication process. To capture that issue we have generalized an approach for treating binary mixtures of colloids and a depletion agent [51] to an approach that is capable to cover mixtures with a discrete number of depletion agent components. To describe natural and experimental situations better, we have generalized this approach further to a continuous distribution of the depletion agent. Within the free-volume theory we obtain an *effective* free-volume fraction $\alpha_{\text{eff}}$. For particles of simple geometry and some commonly used size distributions we have derived explicit expressions for $\alpha_{\text{eff}}$. In the case of three-dimensional depletion agent particles and spherical colloids, $\alpha_{\text{eff}}$ has to be obtained numerically. We have presented results for the bulk phase diagram. Based on our results we conclude that polydispersity favors fluid–fluid phase separation. This finding seems to be robust against the way polydispersity is introduced, as demonstrated for different distributions of the depletion agent, for different underlying equations of state, for size and morphology polydispersity.

We have obtained a remarkable result for bulk mixtures in Sec. 3.5 where we have applied our generalized approach to study ternary mixtures of one colloid component and two species of the polydisperse depletion agent. When the size ratio between the two depletion agent components is asymmetric enough, we find that the phase diagram may exhibit two stable critical points, two triple points and three fluid phases, namely the gas phase, the low density and the high density liquid. This finding seems to be of general character as we find similar results also for two monodisperse species of the depletion agent and for particles of different than non-spherical shape.

Though the AOV model describes a simple fluid — a mixture of hard spheres and ideal polymer — the phenomenology is rather rich. The AOV mixture brought in contact with a wall leads to layering and wetting effects. When confined in a narrow pore one finds capillary condensation. In Chapter 4 we have presented results which highlight the competition between the layering transitions and the capillary condensation. Both effects depend differently on the pore width. The competition between both effects manifests itself in thermodynamic properties like the excess colloid adsorption and the solvation force between the two confining walls. The effects found for a fluid confined in simple geometry, i.e., for the narrow slit-like pore, might play a significant role for more complex confinement like in the case of big colloids with radius $R/\sigma_c \gg 1$ immersed in a colloid-polymer mixture or for porous media filled with a colloidal suspension.

What is the effect of a solvent phase separation on the interparticle interaction between solute particles? This is a challenging question when one keeps in mind that the entropically driven interaction between two spherical particles in an ideal polymer solvent (with vanishing mutual interactions) has been obtained by Asakura and Oosawa in the fifties [9, 10] but it took about four decades until an accurate description was presented for the interaction between two spherical particles in a sea of small hard spheres [17, 18]. When we consider a mixture of hard spheres and ideal polymer one finds that its phase behavior is rather rich. We have presented the influence of the solvent described by an AOV mixture on the solute particle interactions in the wall-sphere and sphere-sphere geometry. In all situations the rich behavior of the solvent manifests itself in a large variety of phenomena. This holds in particular for the solvent near phase coexistence. In that regime many approaches to describe the fluid break down. To highlight the applicability of the presented route, we have studied the behavior of a complex solvent around two colloids at close distance and the effect of curvature on thermodynamic quantities at an ellipsoidal particle.

The colloidal suspensions we have studied here exhibit rather complex behavior, though the underlying AOV model describes a simple fluid. The next step could be to consider a more realistic description based on a theory of polymer with excluded volume interactions. Although we have investigated an idealized model system we believe that the results are robust to the introduction of perturbations and hold for more realistic systems. As colloids cover a wide range of materials the presented methods and results may provide a basis to study the formation of glasses and gels or the dynamics of time-dependent phenomena. The tunable character of interactions between colloids may also be used to study aspects of atomic systems by the use of the underlying larger length and time scales in colloidal systems as compared to atoms. From an experimental point of view the techniques to study colloidal suspensions are well-developed. Small-angle neutron and X-ray scattering provide useful techniques to study the structure of physical as well as biological systems. In the slit geometry the surface force apparatus and two mica plates allow one to measure solvation forces. Moreover, as it is possible to measure the pull-off force on the one-particle level by means of atomic force microscopy and the demixing in colloid-polymer mixtures can be observed directly by confocal microscopy, we hope to stimulate future studies.

# Zusammenfassung

Was sind Kolloide? Der Wortursprung *kolla* (Leim) und *eidos* (Aussehen, Gestalt) deutet eine Nähe zum Bereich der Weichen Materie in der Statistischen Physik an, spiegelt jedoch nicht die ganze Vielfalt an Eigenschaften wider. Der Ausdruck *kolloidal* beschreibt allgemein einen Zustand der Unterteilung und damit speziell in einem Medium dispergierte Teilchen, welche in mindestens einer Richtung von der Größenordnung einiger Nanometer bis hin zu typischerweise einigen Mikrometern sind. Vor etwa einem Jahrhundert spielten Kolloide eine bedeutende Rolle bei der Entwicklung der Vorstellung der diskontinuierlichen Struktur der Materie, d.h. der Existenz von Atomen. A. Einstein sagte voraus, dass aufgrund der thermischen Molekularbewegung kleine Teilchen der Brown'schen Bewegung unterliegen und diese so stark ist, dass sie mit einem Mikroskop beobachtet werden könne. Einige Jahre später gelang es J. Perrin die Voraussagen der Kinetischen Theorie experimentell zu bestätigen und die Existenz von Atomen zu zeigen. Nach der Verleihung der Nobelpreise an R.A. Zsigmondy 1925 und an J. Perrin 1926 für Arbeiten an Kolloiden bzw. der diskontinuierlichen Struktur der Materie folgte in der Zeit danach eine intensive Erforschung des Atommodells, des Quantencharakters der Materie und des Atomkerns. Erst seit kurzer Zeit erfreut sich die Untersuchung kolloidaler Systeme einer Renaissance. Die Entwicklung experimenteller Verfahren, die Verfügbarkeit von Computersimulationen und ausgereifte theoretische Zugänge bilden eine Grundlage dafür. Kolloide sind außerdem von technologischer Bedeutung um mikro- und nanostrukturierte Materialien herzustellen und zu kontrollieren. Gleichzeitig regt die Vielfalt der in der Natur und im Alltag vorkommenden Kolloide, wie etwa in Farben, als rote Blutkörperchen oder in diversen industriellen Prozessen, an, dieses Gebiet zu erforschen.

Kolloidale Systeme können verschiedene Phasenübergänge durchlaufen und etwa eine gasförmige oder kristalline kolloidale Phase haben. Für das Phasenverhalten der Kolloide spielt deren gegenseitige Wechselwirkung eine Rolle. Dabei hat das Lösungsmittel, in dem sich die Kolloide befinden, einen starken Einfluss auf die gegenseitige Wechselwirkung. Seine Rolle fasst man in Form einer effektiven Wechselwirkung zwischen den einzelnen Kolloid-Teilchen zusammen. Weist dabei das Lösungsmittel selbst ein komplexes Phasenverhalten auf, so ist es sehr aufwändig, die effektive Wechselwirkung zu bestimmen. Für spezielle Spezies von Kolloiden gibt es jedoch erfolgreiche Ansätze, um diese Aufgabenstellung zu behandeln. Sterisch oder elektrostatisch stabilisierte Kolloide können eine starke kurzreichweitige aber verschwindende langreichweitige Wechselwirkung aufweisen und deshalb bei sphärischer Geometrie als harte Kugeln beschrieben werden. Es lassen sich außerdem Teilchen wählen, bei denen die Dichte und der Brechungsindex angepasst werden kann, und es können Systeme mit verschwindenden Dispersionskräften untersucht werden. Experimentell lassen sich solche Teilchen mit verschiedenen Methoden herstellen und weisen näherungsweise die genannten Eigenschaften auf. In der Anwendung bildet dieser Ansatzpunkt eine Grundlage für weiterreichende Theorien, störungstheoretisch etwa lassen sich zu einem solchen Referenzsystem attraktive Beiträge einbauen. Basierend auf der Dichtefunktionaltheorie im Rahmen der Fundamentalmaßtheorie (FMT) können beliebige Mischungen von harten Kugeln beschrieben werden. Zusammen mit dem Modell der idealen Polymere, eingeführt von Asakura und Oosawa und, unabhängig davon, von Vrij (AOV), kann die FMT auf Mischungen von Kolloiden und Polymeren erweitert werden. Darauf basierend können wir eine Kolloid-Komponente betrachten, die in einem Lösungsmittel aus weiteren Kolloid-($c$) und Polymer($p$)-Komponenten gelöst ist. Das $cp$-Lösungsmittel spielt dabei die Rolle eines komplexen Lösungsmittels, da dieses System reichhaltiges Phasenverhalten zeigt. Dies ist experimentell, als auch theoretisch gut untersucht worden. Wir verwenden diese Grundlage, um das komplexe Verhalten von kolloidalen Suspensionen zu untersuchen.

Die Darstellung der Ergebnisse dieser Arbeit ist in vier Kapitel unterteilt. Bevor wir zu den Ergebnissen kommen, geben wir eine kurze Einführung in die wichtigsten theoretischen Grundlagen und die Prinzipien in Kapitel 2. Wir beginnen mit grundlegenden Aussagen der Thermodynamik und aus der Theorie der Phasenübergänge. Anschließend geben wir eine Einführung in die Dichtefunktionaltheorie im Abschnitt 2.2 und eine detailliertere Beschreibung des Zugangs für kolloidale Systeme sowohl in der Harte-Kugel-Näherung als auch für Mischungen von Kolloiden und Polymeren im Abschnitt 2.3. Der in dieser Arbeit verwendete Zugang für die Beschreibung des *bulk*-Phasenverhaltens basiert auf der FMT. Wir führen die Grundlagen der Freien-Volumen Theorie (FVT) im Abschnitt 2.4 ein.

Im Kapitel 3 zeigen wir Ergebnisse für das *bulk*-Phasenverhalten von Mischungen aus Kolloiden und einer weiteren Komponente, die als Medium, oder Agens, auftritt und als *depletion agent* bezeichnet wird. Für einige Fälle ist das Phasenverhalten bekannt.

Um einen allgemeinen Zugang zur Bestimmung des Phasenverhaltens zu formulieren, der einerseits unterschiedliche Formen des depletion agent und gleichzeitig eine kontinuierliche Größen- und Formverteilung von Teilchen erlaubt, verallgemeinern wir die Theorie einer kürzlich erschienenen Publikation für Zwei-Komponenten-Systeme. Diese vereint die Fundamentalmaßtheorie mit der Freien-Volumen Theorie und erlaubt in eleganter Weise das Phasenverhalten zu bestimmen. Die Beschreibung erfolgt dabei im Semi-Großkanonischen Ensemble: Wir betrachten eine feste Anzahl der Kolloide und ein depletion agent, der an ein Reservoir gekoppelt ist. Die fundamentale Größe ist hier der freie Volumenbruch $\alpha$, den die depletion agents einnehmen können unter der Berücksichtigung der Besetzung vom Volumen durch die Kolloide. Durch eine Verallgemeinerung der depletion agents auf eine kontinuierliche Verteilung erhalten wir in diesem Zugang einen *effektiven* freien Volumenbruch $\alpha_{\text{eff}}$. Dieser spielt die Rolle von $\alpha$, beinhaltet jedoch eine Integration über den Parameter der Verteilung. Die Verteilung des depletion agents kann in verschiedenen Formen eingeführt werden. Eine natürliche Größe, wie sie typischerweise in Experimenten vorkommt, ist die Partikelgröße. Ein Parameter $q$ stellt in diesem Fall das Radienverhältnis dar. Es ist jedoch auch vorstellbar, dass andere Größen verschieden sein können, wie etwa die Länge von stäbchenförmigen Teilchen bei gleichbleibender Dicke, oder der Durchmesser von Plättchen bei fester Dicke.

Für einige Arten von Teilchen können wir Ausdrücke für den effektiven freien Volumenbruch $\alpha_{\text{eff}}$ in expliziter Form erhalten. Für stäbchenförmige Teilchen und Plättchen, jeweils im Grenzfall vernachlässigbarer Dicke, erhalten wir für verschiedene zugrunde liegende Verteilungen der Stäbchenlänge bzw. des Plättchendurchmessers explizite Ausdrücke für $\alpha_{\text{eff}}$. Dabei verwenden wir häufig verwendete Verteilungen wie die Schulzverteilung, die Gaussverteilung, die Stetige Normalverteilung und die Log-Normalverteilung.

Im Fall von dreidimensionalen Teilchen, wie z.B. von Kugeln im einfachsten Fall, lassen sich keine expliziten Ausdrücke für $\alpha_{\text{eff}}$ finden und der freie Volumenbruch muss numerisch bestimmt werden. Ist diese Größe einmal bestimmt, so können wir daraus das Phasenverhalten der zugrunde liegenden Mischung berechnen. Bei der Berechnung der Phasenverhaltens beschränken wir uns auf die Schulzverteilung. Diese eignet sich aus theoretischer als auch experimenteller Sicht gut für weitere Untersuchungen.

Wir untersuchen Polydispersität verschiedenen Ursprungs. Im ersten Fall betrachten wir eine Mischung aus einer Teilchensorte von monodispersen Kolloiden und einer größen-polydispersen Spezies von depletion agents. Für asymmetrische monodisperse Mischungen dieser Teilchen ist bekannt, dass eine flüssig–flüssig Phasenseparation gegenüber der flüssig–fest Phasenseparation nicht stabil ist. Unter Einfluss der Polydispersität finden wir jedoch, dass eine stabile flüssig–flüssig Phasenseparation auftritt, vorausgesetzt dass die Verteilung breit genug ist. In diesem Fall finden wir einen stabilen kritischen Punkt und einen Tripelpunkt zwischen den drei Phasen gasförmig (kolloid-arm), flüssig (kolloid-reich) und fest (kristallin). Es ist jedoch auch denkbar, Polydispersität in einer anderen Form einzuführen. Dies erlaubt uns unser verallgemeinerter Ansatz. Wir können in einfacher Weise Morphologie-Polydispersität einführen, d.h. Teilchen bei denen andere geometrische Größen als die Teilchengröße variieren. Wir betrachten dabei ellipsoidförmige Teilchen, bei denen die Halbachsen von $q$ abhängen, so dass wir in einem Fall das Teilchenvolumen konstant und in einem anderen Fall linear von $q$ anhängig lassen. In ähnlicher Form, wie schon für kugelförmige depletion agents, finden wir eine stabile fluid–fluid Phasenseparation, wenn die Polydispersität einen bestimmten Grad erreicht hat. Insgesamt können wir zusammenfassend sagen, dass Polydispersität der depletion agents die Phasenseparation zwischen zwei fluiden (der gasförmigen und der flüssigen) Phasen begünstigt. Die Untersuchung des Verhaltens von Grenzfällen, gezeigt am Beispiel von Stäbchen und Plättchen mit verschwindender Dicke, untermauern diese Beobachtung.

Der Schritt von einer einfachen Verteilung, wie der eben beschriebenen Schulzverteilung, zu einer beliebigen Verteilung, wie sie in physikalischen Systemen realisiert werden kann, ist in unserem Zugang einfach durchzuführen. Diese Eigenschaft machen wir uns zunutze und verwenden eine *bimodale* Verteilung $d_S(q; x, \bar{q}, \bar{Q}, z_{\bar{q}}, z_{\bar{Q}}) = x\, d_S(q; \bar{q}, z_{\bar{q}}) + (1 - x)\, d_S(q; \bar{Q}, z_{\bar{Q}})$, d.h. eine Verteilung, die zwei separate polydisperse Komponenten kombiniert. Ist das Verhältnis der Längenskalen $\bar{q}$ und $\bar{Q}$ groß genug und der Überlapp der Teilverteilungen klein, so können wir von einer ternären Mischung aus einer Kolloidkomponente und zwei Spezies von depletion agents sprechen. Wir können die Phasendiagramme für die Mischungsparameter $x = 1$ und $x = 0$ so wählen, dass sie jeweils eine stabile fluid–fluid Phasenseparation haben. Das lässt sich durch Polydispersität oder durch geeignete Größenverhältnisse zwischen den Komponenten erreichen. Doch was passiert für die zusammengesetzte Verteilung $0 \leq x \leq 1$? Wir finden für Werte aus dem Zwischenbereich ein reichhaltiges Phasenverhalten: Neben der Gasphase und dem kristallinen Zustand beobachten wir, dass zwei stabile Phasen auftreten können. Wir finden eine flüssige Phase niedrigerer Dichte (low density liquid) und eine flüssige Phase höherer Dichte (high density liquid). Im gleichen Parameterbereich finden wir dann zwei stabile kritische Punkte und zwei Tripelpunkte. Phasendiagramme mit ähnlichem Verhalten findet man auch in einkomponentigen Systemen, in denen die Wechselwirkungspotentiale zwei Längenskalen aufweisen [52–55]. In unserem Fall führen wir zwei Längenskalen über die verschiedenen Größen der depletion agents ein. Wenn wir diese Längenskalen symmetrischer machen und die beiden Beiträge der einzelnen Verteilungen zur bimodalen Verteilung stark überlappen, so verschwindet dieser Effekt wieder. Dass das Auftreten von solch komplexem Phasenverhalten nicht allein durch Polydispersität zustande kommt, zeigen wir bei Untersuchungen von zwei monodispersen Spezies der depletion agents einerseits und durch Untersuchung von Teilchen anderer Geometrie andererseits.

Im Kapitel 4 untersuchen wir Phänomene von kolloidalen Suspensionen in eingeschränkter Geometrie. Der Einschluss eines fluiden Systems kann, abhängig von der Wechselwirkung zwischen dem Fluid und den einschliessenden Wänden, zu verschiedenen Phasenübergängen führen, wie etwa zur Kapillarkondensation [56–58] oder der Kapillarverdampfung [59, 60]. Das Oberflächenphasenverhalten des Fluids an einer Wand spielt die zentrale Rolle. Für eine Mischung aus Kolloiden und Polymeren ist bekannt, dass Layering- und Benetzungseffekte an einer Wand auftreten können [22]. Ein geeignetes Modell für diese Kolloid-Polymer-Mischungen ist das AOV Modell, welches in der Dichtefunktionaltheorie im Rahmen der FMT diese Effekte an einer Wand aufweist. In eingeschränkter Geometrie einer schmalen Pore aus zwei parallelen Wänden können für dieses System Kapillarkondensation und Kapillarverdampfung beobachtet werden [35, 66]. Betrachtet man nun eine Kolloid-Polymer-Mischung in eingeschränkter Geometrie, so führt der Wettbewerb des Oberflächenphasenverhaltens, also der Layeringeffekte, und der Kapillarkondensation zu einer interessanten Phänomenologie.

Wir zeigen zunächst, dass Layeringphänomene von genereller Natur sind, indem wir für eine thermodynamische Beschreibung verschiedene Zustandsgleichungen verwenden. Darüber hinaus untersuchen wir ob dieser Effekt robust gegenüber dem Einführen von Polydispersität ist. Für eine Kolloid-Polymer-Mischung zwischen zwei ebenen harten Wänden finden wir ein Phasenverhalten, welches, abhängig vom Grad der Einschränkung, folgende drei Phasen aufweisen kann: das kolloidale Gas, die Layering Phase und die kolloidale Flüssigkeit. Für große Abstände der beiden Wände, also ein niedriges Ausmaß der Einschränkung, finden wir alle drei Phasen. Für kleine Abstände, also für eine starke Einschränkung, finden wir nur zwei thermodynamisch stabile Phasen, die Gasphase und die flüssige Phase. Im Übergangsbereich beobachten wir einen Tripelpunkt, an dem drei verschiedene Phasen koexistieren. Betrachtet man das gesamte Phasendiagramm einschließlich der metastabilen Phasen, so finden wir ein komplexes Phasendiagramm. Der Grad der Einschränkung spiegelt sich in dem Wettbewerb zwischen den Layeringübergängen und der Kapillarkondensation wider.

Beide Effekte weisen eine unterschiedliche Anhängigkeit von der Porengröße, in unserem Fall des Abstands der beiden Wände, auf. Während etwa die Verschiebung der fluid–fluid Koexistenzlinie im Phasendiagramm mit einem Potenzgesetz, $\delta\eta_c \propto L^{-1}$, vom Wandabstand abhängt, so zeigt das Layering eine exponentielle Abhängigkeit, $\delta\eta_c \propto \exp(-L/\xi)$. Dieses unterschiedliche Verhalten führt zu unterschiedlich starken Beiträgen bei großen bzw. kleinen Wand-Wand-Abständen. Das Konkurrenzverhalten zwischen den Layeringübergängen und der Kapillarkondensation äußert sich auch in weiteren thermodynamischen Größen, wie etwa der Kolloidadsorption in der Pore und der Solvationskraft zwischen den beiden Wänden. Diese wird durch einen zusätzlichen Druck aufgrund der Korrelationen des Lösungsmittels verursacht. Durch das komplexe Phasenverhalten des eingeschlossenen Fluids finden wir sprunghafte Änderungen der Solvationskraft, wenn ein Phasenübergang durchlaufen wird. Wie in anderen thermodynamischen Größen finden wir ein Potenzgesetz und einen exponentiellen Zusammenhang der Sprunghöhe in der Solvationskraft am Phasenübergang in Abhängigkeit des Wand-Wand-Abstandes.

Nachdem wir das *bulk*-Phasenverhalten des Lösungsmittels für polydisperse Verteilungen und das Verhalten der Kolloid-Polymer-Mischung in eingeschränkter Geometrie für diskrete Mischungen untersucht haben, betrachten wir die effektiven Wechselwirkungen, zu welchen die depletion agents zwischen weiteren Teilchen führen. Im Kapitel 5 untersuchen wir deshalb ein System, in dem ein Kolloid in einem Lösungsmittel, das aus einer Mischung aus kleineren Kolloiden und Polymeren besteht, in die Nähe einer ebenen harten Wand gebracht wird. Das System aus zwei großen kolloidalen Teilchen, suspendiert in einem Lösungsmittel, welches komplexes Phasenverhalten zeigen kann, untersuchen wir im Kapitel 6.

Im Rahmen der Dichtefunktionaltheorie ist es möglich, Dichteprofile von mehrkomponentigen Flüssigkeiten aus Kolloiden und Polymeren an einer ebenen Wand zu bestimmen. Sind die Dichteprofile bekannt, so kann daraus das Potential der entropischen Kraft (depletion potential) einer Komponente zwischen der Wand und einer Teilchensorte $b$ im Grenzfall verschwindender Dichte, $\rho_b \to 0$, bestimmt werden. Das Potential der entropischen Kraft $W(z)$ kann ohne der expliziten Bestimmung des Dichteprofils der Komponente $b$ mit Hilfe der Einfügemethode (insertion method) bestimmt werden. Wir verwenden diese Methode und untersuchen Potentiale der entropischen Kraft von Mischungen aus Kolloiden und Polymeren. Letztere weisen als *bulk*-System eine Phasenseparation in zwei fluide Phasen auf, die kolloidale Gasphase und die kolloidale Flüssigkeit. Bleibt man jedoch in der fluiden Phase, d.h. unterhalb des kritischen Punktes in der $(\eta_c, \eta_p^r)$-Darstellung des Phasendiagramms, so beobachten wir bei Potentialen der entropischen Kraft entlang horizontaler Pfade im Phasendiagramm für kleine Anteile an Kolloiden nahezu monotones Verhalten. Bei Zunahme des Kolloidanteils gegenüber dem Polymeranteil sehen wir eine Zunahme des oszillatorischen Verhaltens. Für Pfade, die in der Nähe des kritischen Punktes verlaufen, beobachten wir außerdem, dass für kleine Normalabstände $z$ von der Wand die Potentiale $W(z)$ stark von der Nähe des Zustandes zu Phasenübergängen beeinflusst werden und deshalb flach und langreichweitiger verlaufen. Um einen Zusammenhang zwischen den Potentialen der entropischen Kraft $W(z)$ und dem Phasenverhalten herzustellen, untersuchen wir den Oberflächenvirialkoeffizienten $\hat{B}_2$. Mit unserer Definition, Gln. (5.5) und (5.8), nimmt der Betrag des Koeffizienten $\hat{B}_2$ mit Zunahme der Packungsdichten zu. Bemerkenswert ist, dass dann wenn wir in die Nähe des Bereichs der fluid–fluid Phasenseparation kommen, der Betrag von $\hat{B}_2$ sehr stark zunimmt. Wir finden aber noch einen weiteren Zusammenhang zum Phasenverhalten. Das Phasendiagramm der Kolloid-Polymer-Mischung wird durch die Fisher-Widom-Linie in zwei Bereiche geteilt. In einem Bereich fallen Korrelationen $g_{ij}(r)$ im asymptotischen Bereich ($r \to \infty$) monoton und exponentiell ab, im anderen oszillatorisch und exponentiell. Andere strukturelle Größen wie z.B. Dichteprofile, Potentiale der entropischen Kraft und Solvationskräfte zeigen dasselbe asymptotische Verhalten. Betrachtet man nun das Verhalten von $\hat{B}_2$, so finden wir ebenfalls eine Linie im Phasendiagramm an der der Oberflächenvirialkoeffizient maximal wird. Diese Linie weist eine auffallende Nähe zur Fisher-Widom-Linie auf.

Durch die Definition von $\hat{B}_2$ erhalten wir einen Zusammenhang zur Adsorption der Spezies $b$ an der ebenen Wand. Mit Hilfe des Gibbs'schen Adsorptionstheorems und der exzess Helmholtz'schen Freien Energiedichte $\Phi_{ex}$ können wir den Grenzwert von $\hat{B}_2 \to \infty$ untersuchen. Wir finden, dass die Zustände im Phasendiagramm, die diese Eigenschaft aufweisen, auf der Spinodalen liegen, also auf der Linie, die nichtstabile Zustände im Phasendiagramm begrenzt.

Der Einfluss des Phasenverhaltens des Lösungsmittels auf die Wechselwirkung zwischen zwei Teilchen ist komplex. Für einfache Systeme, etwa eine binäre Hartkugelmischung, ist das Phasenverhalten in weiten Bereichen hinreichend einfach, so dass bei asymmetrischen Mischungen die Freiheitsgrade der kleinen Komponente ausintegriert werden können, und das System als eine effektiv einkomponentige Flüssigkeit mit effektiver Wechselwirkung beschrieben werden kann. Für Mischungen, bei denen das Lösungsmittel eine Phasenseparation aufweist, muss das Ausintegrieren der Freiheitsgrade dieses berücksichtigen, was nicht einfach zu erreichen ist, da die Einfügemethode Effekte wie Kapillarkondensation oder Bridging nicht richtig beschreiben kann. Wir untersuchen deshalb das Verhalten einer AOV Mischung in der Nähe von festgehaltenen Teilchen, welche als das externe Potential für die Mischung wirken. Dabei betrachten wir einerseits zwei große sphärische Kolloide in kleinem Abstand und andererseits ein ellipsoidförmiges Teilchen. Um das Problem numerisch zu lösen, berücksichtigen wir die Rotationssymmetrie und führen ein trianguliertes Gitter für die Durchführung von Faltungsintegralen ein, welche für die gewichteten Dichten in der FMT benötigt werden. Wir merken an, dass es numerisch deutlich aufwändiger ist, die Dichteprofile $\rho_i(z, r)$ zu berechnen als radialsymmetrische Profile $g_i(r)$ in der Nähe eines einzigen Kolloids. Durch die numerischen Einschränkungen können wir kein stark asymmetrisches System betrachten. Für zwei große Kolloide $b$ in einer phasenseparierenden AOV Mischung als Lösungsmittel betrachten wir dabei ein System aus zwei fixen großen Teilchen $b$ und variieren die Zustandsvariablen indem wir die Packungsdichte $\eta_c$ der Kolloid($c$)-Komponente des Lösungsmittels ändern. Für niedrige Werte von $\eta_c$ finden wir eine geringe Abhängigkeit der Dichteprofile von der Krümmung des Kolloids $b$. Bei Zunahme von $\eta_c$ finden wir eine Reihe von Sprüngen in den Adsorptionen $\Gamma_i$ der Komponenten des Lösungsmittels. An gleicher Stelle schneiden sich jeweils zwei Kurven des Großkanonischen Potentials. Ein Blick auf die Dichteprofile veranschaulicht (in diesem endlichen System) diese Pseudophasenübergänge. Wir sehen eine sprunghafte Anreicherung der Kolloiddichte $\rho_c(z, r)$ im Bereich zwischen den fixierten Teilchen $b$ bei geringfügiger Änderung der Packungsdichte $\eta_c$. Wir merken an, dass wir wegen des numerischen Aufwands maximal ein Radienverhältnis von 1 : 20 zwischen den Teilchen des Lösungsmittels und der großen Kolloide verwenden können, und wir uns für bestimmte Fälle im metastabilen Bereich des Phasendiagramms der Kolloid-Polymer-Mischung befinden. Einen analogen Pfad im Phasendiagramm verfolgen wir für ein ellipsoidförmiges Teilchen, das sich in einer phasenseparierenden AOV Mischung als Lösungsmittel befindet. Auch hier beobachten wir einen Sprung in den Adsorptionen der Lösungsmittelteilchen und Bereiche des Großkanonischen Potentials mit unterschiedlichen Steigungen. Fallen die Potentiale verschiedener Bereiche in einem Schnittpunkt zusammen, so kommt es zu einem Pseudophasenübergang für dieses endliche System. Deutlich zu sehen ist in diesem Beispiel die Abhängigkeit der Dichte $\rho_c(z, r)$ von der Position an der Oberfläche des ellipsoidförmigen Teilchens $b$. Für ein prolates Teilchen finden wir Bereiche mit einem Layeringverhalten im Dichteprofil in der Nähe der kurzen Halbachse, während das Dichteprofil in Richtung der langen Halbachsen keine Layeringstrukturen zeigt. Wir sehen in den beiden Fällen, dem AOV Lösungsmittel in der Nähe von zwei großen Kolloiden und in der Nähe eines ellipsoidförmigen Teilchens, dass das Phasenverhalten des Lösungsmittels eine große Rolle spielt und das Verhalten der effektiven Wechselwirkung stark beeinflusst.

Kolloidale Systeme beschreiben eine breite Klasse von Teilchen, da sie hauptsächlich über ihre Größe definiert sind. Für Teilchen, die sich mit Hard-Core-Potentialen beschreiben lassen, wie etwa kugelförmige Kolloide, Polymerknäuel oder dünne Plättchen, bildet das AOV Modell einen geeigneten Ausgangspunkt für theoretische Untersuchungen. Basierend auf diesem Modell läßt sich eine verallgemeinerte Freie-Volumen Theorie und Dichtefunktionaltheorie zur Beschreibung verschiedener kolloidaler Systeme und deren Verhaltens anwenden.

Zum einem spielt es für die Beschreibung der Naturvorgänge und von Experimenten eine wichtige Rolle, Verteilungen verschiedener Teilchen zu beschreiben. Wir konnten mit einem verallgemeinerten Zugang den Effekt der Polydispersität untersuchen. Gleichzeitig erlaubte es unser Zugang, beliebige Verteilungen zu verwenden, und wir konnten für bimodale und bidisperse Mischungen aus depletion agents ein unerwartet komplexes Phasendiagramm mit zwei kritischen Punkten und drei fluiden Phasen finden.

Obwohl das AOV Modell ein einfaches Fluid beschreibt weist es doch zahlreiche Effekte auf. Eine wichtige Einflussgröße auf thermodynamische Eigenschaften ist der Einschluss einer Kolloid-Polymer-Mischung in eingeschränkten Geometrien. Für das hier verwendete Modell konnten wir dabei einen Wettbewerb verschiedener Phasenübergänge untersuchen. Abhängig vom Grad der Einschränkungen, wie z.B. der Porengröße, tritt dabei Layering-Verhalten bzw. Kapillarkondensation auf. Wir konnten bestätigen, dass beide Übergänge in unterschiedlicher Art von der Einschränkung abhängen.

Was ist der Effekt der Phasenseparation eines Lösungsmittels auf die effektive Wechselwirkung zwischen Teilchen der gelösten Substanz? Wir haben eine Kolloid-Polymer-Mischung als Lösungsmittel verwendet, um den Einfluss des komplexen Phasenverhaltens zu studieren. Unser Zugang machte es möglich den Effekt der Phasenseparation an zwei großen Kolloiden und Krümmungseffekte direkt zu untersuchen.

Ein weiterer Schritt um realistischere Systeme zu beschreiben wäre etwa die Berücksichtigung von Polymeren mit Ausschlussvolumen-Wechselwirkungen (excluded volume interactions). Die AOV Mischung, welche wir für viele Untersuchungen zu Grunde gelegt haben, beschreibt ein simples Modellsystem. Dennoch glauben wir das die Ergebnisse sich auch unter Einführung von Störungen übertragen lassen und für realistischere Modelle gelten. Der einstellbare Charakter der Wechselwirkungen zwischen den Kolloiden kann außerdem dazu verwendet werden, um Aspekte von atomaren Systemen zu untersuchen. Dabei kann man die zu Grunde liegenden größeren Längen- und Zeitskalen als sie bei Atomen vorkommen nutzen. Vom experimentellen

Standpunkt aus lassen sich Kolloide mit diversen weit entwickelten Methoden untersuchen. Kleinwinkel-Neutronen- und Kleinwinkel-Röntgenstreuung bieten jeweils eine Methode zur Untersuchung der Struktur von physikalischen als auch biologischen Systemen. In der eingeschränkten Geometrie, speziell der schmalen Pore, kann mit dem sog. surface force apparatus oder dem Glimmerplättchen die Solvationskraft gemessen werden. Es ist außerdem möglich auch deutlich kleinere Systeme, bis hin zu einzelnen Teilchen, mit der Atomkraftmikroskopie zu untersuchen oder die Entmischung in Kolloid-Polymer-Mischungen mit der konfokalen Mikroskopie direkt zu beobachten. Wir hoffen mit unseren Ergebnissen zukünftige Arbeiten anregen zu können.

# Bibliography

[1] A. Einstein, Ann. Phys. **17**, 549 (1905).

[2] J. Perrin, Ann. Chim. Phys. **18**, 5 (1909).

[3] P.N. Pusey, in *Liquids, Freezing and the Glass Transition*, Proc. Les Houches Session L1, eds. J.P. Hansen, D. Levesque and J. Zinn-Justin (Elsevier, Amsterdam, 1991).

[4] V.J. Anderson and H.N.W. Lekkerkerker, Nature **416**, 811 (2002).

[5] J.C. Crocker and D.G. Grier, Phys. Rev. Lett. **73**, 352 (1994).

[6] J. Baumgartl, J.L. Arauz-Lara, and C. Bechinger, Soft Matter **2**, 631 (2006).

[7] J.K. Percus and G.J. Yevick, Phys. Rev. **110**, 1 (1958).

[8] G.A. Mansoori, N.F. Carnahan, K.E. Starling, and T.W. Leland, J. Chem. Phys. **54**, 1523 (1971).

[9] S. Asakura and F. Oosawa, J. Chem. Phys. **22**, 1255 (1954).

[10] S. Asakura and F. Oosawa, J. Pol. Sci. **33**, 183 (1958).

[11] A. Vrij, Pure Appl. Chem. **48**, 471 (1976).

[12] R. Evans, Adv. Phys. **28**, 143 (1979).

[13] Y. Rosenfeld, Phys. Rev. Lett. **63**, 980 (1989).

[14] M. Schmidt, H. Löwen, J.M. Brader, and R. Evans, Phys. Rev. Lett. **85**, 1934 (2000).

[15] B. Götzelmann, R. Evans, and S. Dietrich, Phys. Rev. E **57**, 6785 (1998).

[16] M. Dijkstra, R. van Roij, and R. Evans, Phys. Rev. E **59**, 5744 (1999).

[17] B. Götzelmann, R. Roth, S. Dietrich, M. Dijkstra, and R. Evans, Europhys. Lett. **47**, 398 (1999).

[18] R. Roth, R. Evans, and S. Dietrich, Phys. Rev. E **62**, 5360 (2000).

[19] C.N. Likos, Phys. Reports **348**, 267 (2001).

[20] R. Roth and R. Evans, Europhys. Lett. **53**, 271 (2001).

[21] A.J. Archer, R. Evans, and R. Roth, Europhys. Lett. **59**, 526 (2002).

[22] J.M. Brader, R. Evans, and M. Schmidt, Mol. Phys. **101**, 3349 (2003).

[23] D.G.A.L. Aarts, M. Schmidt, and H.N.W. Lekkerkerker, Science **304**, 847 (2004).

[24] F.L. Calderon, J. Bibette, and J. Biais, Europhys. Lett. **23**, 653 (1993).

[25] P.N. Pusey, W.C.K. Poon, S.M. Illet, and P. Bartlett, J. Phys.: Condens. Matter **6**, A29 (1994).

[26] M. Adams, Z. Dogic, S.L. Keller, S. Fraden, Nature **393**, 349 (1998).

[27] G.A. Vliegenthart, A. van Blaaderen, and H.N.W. Lekkerkerker, Faraday Discuss. **112**, 173 (1999).

[28] E.H.A. de Hoog, W.K. Kegel, A. van Blaaderen, and H.N.W. Lekkerkerker, Phys. Rev. E **64**, 021407 (2001).

[29] D.G.A.L. Aarts and H.N.W. Lekkerkerker, J. Phys.: Condens. Matter **16**, S4231 (2004).

[30] K.L. Gawrys and P.K. Kilpatrick, J. Colloid Interface Sci. **288**, 325 (2005).

[31] S. Bhat, R. Tuinier and P. Schurtenberger, J. Phys.: Condens. Matter **18**, L339 (2006).

[32] M. Dijkstra, Current Opinion in Colloid & Interface Science **6**, 372 (2001).

[33] J.G. Malherbe and S. Amokrane, Mol. Phys. **99**, 355 (2001).

[34] J. Liu and E. Luijten, Phys. Rev. Lett. **92**, 035504 (2004).

[35] M. Schmidt, A. Fortini, and M. Dijkstra, J. Phys.: Condens. Matter **15**, S3411 (2003).

[36] P.P.F. Wessels, M. Schmidt, and H. Löwen, Phys. Rev. E **68**, 061404 (2003).

[37] H.N.W. Lekkerkerker, W.C.K. Poon, P.N. Pusey, A. Stroobants, and P.B. Warren, Europhys. Lett. **20**, 559 (1992).

[38] M. Dijkstra, J.M. Brader, and R. Evans, J. Phys.: Condens. Matter **11**, 10079 (1999).

[39] D.G.A.L. Aarts, R. Tuinier, and H.N.W. Lekkerkerker, J. Phys.: Condens. Matter **14**, 7551 (2002).

[40] B.J. Alder and T.E. Wainwright, J. Chem. Phys. **27**, 1208 (1957).

[41] M. Foroutana and M.A. Jafarizadeh, Physica A **329**, 337 (2003).

[42] R.P. Sear and D. Frenkel, Phys. Rev. E **55**, 1677 (1997).

[43] D. Goulding and J.P. Hansen, Mol. Phys. **99**, 865 (2001).

[44] R.M.L. Evans, J. Chem. Phys. **114** 1915 (2001).

[45] P. Sollich, J. Phys.: Condens. Matter **14**, R79 (2002).

[46] D.J. Fairhurst and R.M.L. Evans, Colloid Polym. Sci. **282**, 766 (2004).

[47] D. Henderson, D.T. Wasan and A. Trokhymchuk, Mol. Phys. **102**, 2081 (2004).

[48] M. Fasolo and P. Sollich, cond-mat/0410374.

[49] M. Fasolo and P. Sollich, Phys. Rev. E **70**, 041410 (2004).

[50] P. Paricaud, S. Varga, P.T. Cummings, and G. Jackson, Chem. Phys. Lett. **398**, 489 (2004).

[51] S.M. Oversteegen and R. Roth, J. Chem. Phys. **122**, 214502 (2005).

[52] P.C. Hemmer and G. Stell, Phys. Rev. Lett. **24**, 1284 (1970).

[53] G. Stell and P.C. Hemmer, J. Chem. Phys. **56**, 4274 (1972).

[54] G. Franzese, G. Malescio, A. Skibinsky, S.V. Buldyrev, and H.E. Stanley, Nature **409**, 692 (2001).

[55] F. Lo Verso, M. Tau, and L. Reatto, J. Phys.: Condens. Matter **15**, 1505 (2003).

[56] R. Evans and P. Tarazona, Phys. Rev. Lett. **52**, 557 (1984).

[57] R. Evans, U.M.B. Marconi, and P. Tarazona, J. Chem. Phys. **84**, 2376 (1986).

[58] R. Evans, J. Phys.: Condens. Matter **2**, 8989 (1990).

[59] H. Dominguez, M. Allen, and R. Evans, Mol. Phys. **96**, 209 (1999).

[60] S. Varga, D. Boda, D. Henderson, and S. Sokołowski, J. Colloid Interface Sci. **227**, 223 (2000).

[61] T. Grünewald, L. Dähne, and C.A. Helm, J. Phys. Chem. B **102**, 4988 (1998).

[62] D.A. Antelmi, P. Kékicheff, and P. Richetti, Langmuir **15**, 7774 (1999).

[63] H.K. Christenson and C.E. Blom, J. Chem. Phys. **86**, 419 (1987).

[64] J.L. Parker, P. Richetti, P. Kékicheff, and S. Sarman, Phys. Rev. Lett. **68**, 1955 (1992).

[65] H. Wennerström, K. Thuresson, P. Linse, and E. Freyssingeas, Langmuir **14**, 5664 (1998).

[66] M. Schmidt, A. Fortini, and M. Dijkstra, J. Phys.: Condens. Matter **16**, S4159 (2004).

[67] R. Roth, R. Evans, A. Lang, and G. Kahl, J. Phys.: Condens. Matter **14**, 12063 (2002).

[68] J.-P. Hansen and H. Löwen, Annu. Rev. Phys. Chem. **51**, 209 (2000).

[69] A.J. Archer and R. Evans, J. Chem. Phys. **118**, 9726 (2003).

[70] P. Hohenberg and W. Kohn, Phys. Rev. **136**, B864 (1964).

[71] N.D. Mermin, Phys. Rev. **137**, A1441 (1965).

[72] T. Morita and K. Hiroike, Prog. Theor. Phys. **25**, 537 (1961).

[73] C. de Dominicis, J. Math. Phys. **3**, 983 (1962).

[74] F.H. Stilinger and F.P. Buff, J. Chem. Phys. **1**, 37 (1962).

[75] J.K. Percus, in *Equilibrium Theory of Classical Fluids*, eds. H.L. Frisch and J. Lebowitz (Benjamin, New York, 1964).

[76] C. Ebner, W.F. Saam, and D. Stroud, Phys. Rev. A **14**, 2264 (1976).

[77] W.F. Saam and C. Ebner, Phys. Rev. A **15**, 2566 (1977).

[78] R. Evans, in *Fundamentals of Inhomogeneous Fluids*, ed. D. Henderson (Dekker, New York, 1992).

[79] J. Wu, AIChE J **52**, 1169 (2006).

[80] J. A. Barker and D. Henderson, Rev. Mod. Phys. **48**, 587 (1976).

[81] Y.-X. Yu and J. Wu, J. Chem. Phys. **117**, 10156 (2002).

[82] H. Hansen-Goos and R. Roth, J. Chem. Phys. **124**, 154506 (2006).

[83] H. Hansen-Goos and R. Roth, J. Phys.: Condens. Matter, accepted (2006).

[84] M. Schmidt, H. Löwen, J. M. Brader, and R. Evans, J. Phys.: Condens. Matter **14**, 9353 (2002).

[85] N.F. Carnahan and K.E. Starling, J. Chem. Phys. **51**, 635 (1969).

[86] P.-M. König, R. Roth, and K. Mecke, Phys. Rev. Lett. **93**, 160601 (2004).

[87] R. Evans and U.M.B. Marconi, J. Chem. Phys. **86**, 7138 (1987).

[88] A. Gonzalez, J.A. White, and R. Evans, J. Phys.: Condens. Matter **9**, 2375 (1997).

[89] A. Gonzalez and J.A. White, Physica A **296**, 347 (2001).

[90] J.K. Percus, J. Stat. Phys. **15**, 505 (1976).

[91] T.K. Vanderlick, H.T. Davis, and J.K. Percus, J. Chem. Phys. **91**, 7136 (1989).

[92] J.P. Hansen and I.R. McDonald, *Theory of simple liquids*, (Academic Press, London, 2003).

[93] S.M. Oversteegen and H.N.W. Lekkerkerker, J. Chem. Phys. **120**, 2470 (2004).

[94] D. Frenkel and A.J.C. Ladd, J. Chem. Phys. **81**, 3188 (1984).

[95] W.W. Wood, J. Chem. Phys. **20**, 1334 (1952).

[96] Y. Rosenfeld, Phys. Rev. E **50**, R3318 (1994).

[97] Y. Rosenfeld, Mol. Phys. **86**, 637 (1995).

[98] T. Boublík, J. Chem. Phys. **53**, 471 (1970).

[99] P.B. Warren, Langmuir **13**, 4588 (1997).

[100] R. Roth, R. Evans, and A.A. Louis, Phys. Rev. E **64**, 051202 (2001).

[101] E.J. Meijer and D. Frenkel, J. Chem. Phys. **100**, 6873 (1994).

[102] M. Fasolo and P. Sollich, J. Phys.: Condens. Matter **17**, 797 (2005).

[103] S.V. Buldyrev, G. Franzese, N. Giovambattista, G. Malescio, M.R. Sadr-Lahijany, A. Scala, A. Skibinsky, and H.E. Stanley, Physica A **304**, 23 (2002).

[104] G. Malescio, G. Franzese, G. Pellicane, A. Skibinsky, S.V. Buldyrev, and H.E. Stanley, J. Phys.: Condens. Matter **14**, 2193 (2002).

[105] J.M. Brader, R. Evans, M. Schmidt, and H. Löwen, J. Phys.: Condens. Matter **14**, L1 (2002).

[106] R. Evans and U.M.B. Marconi, Phys. Rev. A **32**, 3817 (1985).

[107] A. Fortini, M. Schmidt, and M. Dijkstra, Phys. Rev. E **73**, 051502 (2006).

[108] J.R. Henderson, Mol. Phys. **59**, 89 (1986).

[109] S.G. Ash, D.H. Everett, and C.J. Radke, J. Chem. Soc., Faraday Trans. 2 **69**, 1526 (1973).

[110] E. Helfand, H. Reiss, H.L. Frisch, and J.L. Lebowitz, J. Chem. Phys. **33**, 1379 (1960).

[111] H. Shinto, K. Uranishi, M. Miyahara, and K. Higashitani, J. Chem. Phys. **116**, 9500 (2002).

[112] P.B. Paramonov and S.F. Lyuksyutov, J. Chem. Phys. **123**, 084705 (2005).

[113] W.G. McMillan and J.E. Mayer, J. Chem. Phys. **13**, 276 (1945).

[114] X. Ye, T. Narayanan, P. Tong, J.S. Huang, M.Y. Lin, B.L. Carvalho, and L.J. Fetters, Phys. Rev. E **54**, 6500 (1996).

[115] M.E. Fisher and B. Widom, J. Chem. Phys. **50**, 3756 (1969).

[116] S. Sokolowski and J. Stecki, Acta Phys. Pol. A **55**, 611 (1979).

[117] J. Stecki and S. Sokołowski, Mol. Phys. **39**, 343 (1980).

[118] D.A. McQuarrie and J.S. Rowlinson, Mol. Phys. **60**, 977 (1987).

[119] R. Roth, J. Phys.: Condens. Matter **17**, S3463 (2005).

[120] M. Kinoshita, S. Iba, K. Kuwamoto, and M. Harada, J. Chem. Phys **105**, 7177 (1996).

[121] C. Bauer, T. Bieker, and S. Dietrich, Phys. Rev. E **62**, 5324 (2000).

[122] J. Fukuda, H. Stark, M. Yoneya, and H. Yokoyama, Phys. Rev. E **69**, 041706 (2004).

[123] T. Araki and H. Tanaka, Phys. Rev. E **73**, 061506 (2006).

[124] B. Widom, J. Phys. Chem. **86**, 869 (1982).

[125] J.R. Henderson, Mol. Phys. **50**, 741 (1983).

[126] R. Evans, R.J. Leote de Carvalho, J.R. Henderson, and D.C. Hoyle, J. Chem. Phys. **100**, 591 (1994).

[127] C. Grodon, M. Dijkstra, R. Evans, and R. Roth, J. Chem. Phys. **121**, 7869 (2004).

[128] C. Grodon, M. Dijkstra, R. Evans, and R. Roth, Mol. Phys. **103**, 3009 (2005).

[129] R. Evans, U.M.B. Marconi, and P. Tarazona, J. Chem. Soc., Faraday Trans. 2 **82**, 1763 (1986).

[130] P.-M. König, P. Bryk, K. Mecke, and R. Roth, Europhys. Lett. **69**, 832 (2005).

# Danksagung

In den vergangenen drei Jahren hatte ich die Gelegenheit an einer spannenden Aufgabe zu arbeiten. Zum Gelingen und erfolgreichen Abschluss habe ich von verschiedener Seite Unterstützung erhalten. Es freut mich folgenden Personen meinen Dank aussprechen zu können.

*Prof. Dr. S. Dietrich*, der mir die Gelegenheit gab an diesem spannenden Thema arbeiten zu können. Ich konnte von den interessanten Diskussionen über Detail- als auch Überblicksfragen profitieren. Das MPI für Metallforschung in Stuttgart und speziell unsere Abteilung boten ein exzellentes Umfeld.

*Prof. Dr. U. Seifert*, für die spontane Bereitschaft zur Übernahme des Zweitgutachtens dieser Arbeit.

*Dr. R. Roth*, für seine fortwährende Unterstützung und hervorragende Zusammenarbeit. Von den Diskussionen spannender fachlicher Fragen, der Weitergabe der Faszination an der Physik und diesem faszinierenden Thema und einem offenen Ohr bei der Betreuung habe ich in ganz besonderem Maß profitiert.

*Prof. Dr. R. Evans*, for fruitful discussions and great collaboration in various projects.

*Dr. M. Sprenger* und *Dr. T. Hiester*, meinen Bürokollegen für die tolle Atmosphäre, die Diskussion kleiner und großer Dinge und die Verleihung des Schifferpatents für die Lamellenjalousie.

*Dr. P.-M. König*, für die ausgezeichnete Zusammenarbeit, den gemeinsamen Spaß an der DFT (”ten-digits man”) und das Teilen der Bewunderung von grep, sed, *et.al.*

*Dr. J.M. Brader* and *S. Macke*, for interesting discussions concerning particular topics.

*H. Hansen-Goos* und *H. Lehle* für den umsichtigen Umgang mit unseren Ressourcen und die Gespräche ”beyond entropy”, *R.-J. Merath* für die Unterhaltung und allen Gruppenmitgliedern für die angenehme Arbeitsatmosphäre.

*Meinen Eltern*, von denen ich immer die volle Unterstützung bekam und die mir alle Freiheiten für das Studium ließen.

Meiner Freundin *Steffi*, dafür dass sie für mich da ist und Geduld und Verständnis für meine Arbeit aufbringt.